OPTICAL FIBER DEVICES FABRICATED BY FEMTOSECOND LASER MICRO-MACHINING FOR SENSING APPLICATIONS

YANG MINWEI

Ph.D

The Hong Kong Polytechnic University

2011

The Hong Kong Polytechnic University

Department of Electrical Engineering

OPTICAL FIBER DEVICES FABRICATED BY FEMTOSECOND LASER MICRO-MACHINING FOR SENSING APPLICATIONS

YANG MINWEI

A thesis submitted in partial fulfillment of the requirements

for the Degree of Doctor of Philosophy

March 2011

CERTIFICATE OF ORIGINALITY

I hereby declare that this thesis is my own work and that, to the best of my knowledge and belief, it reproduces no material previously published or written, nor material that has been accepted for the award of any other degree or diploma, except where due acknowledgement has been made in the text.

_____ (Signed)

_____ YANG Minwei __ (Name of Student)

Abstract

The development of optical fiber sensors (OFS) with high sensitivity and compact dimension is receiving increased attention. One promising solution is to develop micro-structure based OFS, which requires excellent performance of fabrication tools. Femtosecond pulse (fs) laser is widely applied for micro-machining due to the advantages of high precision, good quality and excellent spatial resolution, which is suitable for fabricating micro-structures over fiber.

This thesis starts with a background review of the fs laser micro-machining technique, including the generation of ultrashort pulse duration and high power intensity, the advantages and typical applications of fs laser micro-machining and micro-structured OFS fabricated by fs laser in previous literatures.

The fs laser micro-machining system setup is described, which includes: 1) a commercialized fs laser; 2) an external optical path; and 3) a microscopy system. The detailed descriptions on the focusing micro objective lens and its effect on the fabricated micro-structure dimensions are presented.

With proper micro-machining parameters, a symmetrically located micro-hole can be drilled into the core center. The micro-hole can introduce scattering loss that is changeable according to the external refractive index (RI) and the transmission properties depend on its diameter near the core. Such a micro-hole can be used as RI sensor based on transmission detection, with a linear response and a small temperature-RI cross sensitivity, which enables temperature independent RI sensing.

Fs laser scanning technique is applied to fabricate micro-cavity into fiber. By asymmetrically positioned the micro-cavity to be deviated from the core center,

the remaining core and the micro-cavity can form a Mach-Zehnder interferometer (MZI) with a large RI difference between the two arms and enables a compact device dimension. The fringe visibility can be optimized by adjusting the deviation position. The micro-cavity can be applied for both high temperature (up to 1100 ℃) sensing with a good repeatability and RI sensing with an extremely large sensitivity around the RI value of water.

Novel structural modulated long period fiber grating (LPFG) can be fabricated by periodically positioning micro-holes either symmetrically in all solid photonic bandgap fiber or asymmetrically in single mode fiber. The micro-holes can effectively couple energy from core mode to cladding mode and thus enabling a compact grating dimension. Cladding modes involved in coupling are numerically simulated and compared with the experiments. The RI sensing properties are measured for both types of LPFG.

Integration of micro-holes into the fiber with inscribed fiber Bragg grating (FBG) is achieved by locating micro-holes asymmetrically on one side of the core. The micro-holes can partially expose the core to external RI without significantly damaging the FBG structure. This composite sensor can detect both temperature and RI simultaneously, by tracing the wavelength change and transmission loss of the FBG resonant dip.

Selective infiltration of liquid into air hole(s) of photonic crystal fiber is developed. This technique has the advantages of flexibility, good accuracy and device robustness. Two kinds of sensor devices, a directional coupler and a MZI are developed based on this technique. Both of the devices possess a large temperature sensitivity.

List of Publications

Journal Papers

1. **M. Yang**, Y. Li, and D. N. Wang, "Long-period fiber gratings fabricated by use of defocused CO_2 laser beam for polarization-dependent loss enhancement," J. Opt. Soc. Am. B **26**, 1203-1208 (2009).

2. **M. Yang**, D. N. Wang, Y. Wang, and C. R. Liao, "Long period fiber grating formed by periodically structured microholes in all-solid photonic bandgap fiber," Opt. Express **18**, 2183-2189 (2010).

3. **M. Yang**, D. N. Wang, Y. Wang, and C. R. Liao, "Fiber in-line Mach–Zehnder interferometer constructed by selective infiltration of two air holes in photonic crystal fiber," Opt. Lett. **36**, 636-638 (2011).

4. **M. Yang**, D. N. Wang, C. R. Liao, "Fiber Bragg grating with micro-holes for simultaneous and independent refractive index and temperature sensing," IEEE Photon. Technol. Lett, to be published, DOI: 10.1109/LPT.2011.2163624.

5. Y. Li, **M. Yang**, D. N. Wang, J. Lu, T. Sun, and K. T. V. Grattan, "Fiber Bragg gratings with enhanced thermal stability by residual stress relaxation," Opt. Express **17**, 19785-19790 (2009).

6. Y. Wang, D. N. Wang, **M. Yang**, W. Hong, and P. Lu, "Refractive index sensor based on a microhole in single-mode fiber created by the use of femtosecond laser micromachining," Opt. Lett. **34**, 3328-3330 (2009).

7. Y. Wang, **M. Yang**, D. N. Wang, S. Liu, and P. Lu, "Fiber in-line Mach–Zehnder interferometer fabricated by femtosecond laser micromachining for refractive index measurement with high sensitivity," J. Opt. Soc. Am. B **27**, 370-374 (2010).

8. Y. Wang, Y. Li, C. R. Liao, D. N. Wang, **M. Yang**, and P. Lu, "High-temperature sensing using miniaturized fiber in-line Mach–Zehnder interferometer," IEEE Photon. Technol. Lett. **22**, 39-41 (2010).

9. X. Fang, X. Y. He, C. R. Liao, **M. Yang**, D. N. Wang, and Y. Wang, "A new

method for sampled fiber Bragg grating fabrication by use of both femtosecond laser and CO_2 laser," Opt. Express **18**, 2646-2654 (2010).

10. C. R. Liao, Y. Wang, D. N. Wang, and **M. Yang**, "Fiber in-line Mach–Zehnder interferometer embedded in FBG for simultaneous refractive index and temperature measurement," IEEE Photon. Technol. Lett. **22**, 1686-1688 (2010).

11. Y. Li, **M. Yang**, C. R. Liao, D. N. Wang, J. Lu, and P. X. Lu, "Prestressed fiber Bragg grating with high temperature stability," J. Lightwave Technol. **29**, 1555-1559 (2011).

12. Y. Wang, **M. Yang**, D. N. Wang, and C. R. Liao, "Selectively infiltrated photonic crystal fiber with ultrahigh temperature sensitivity," IEEE Photon. Technol. Lett, to be published, DOI: 10.1109/LPT.2011.2163705.

Conference Papers

1. **M. Yang**, D. N. Wang, and Y. Li, "Long period fiber grating fabricated by defocused CO_2 laser for refractive index sensing," 1st Workshop on Specialty Optical Fibers and Their Applications (2008).

2. Y. Wang, D. N. Wang, **M. Yang**, W. Hong, and P. Lu, "Femtosecond laser drilled micro-hole in a single-mode fiber for refractive index sensing," ISOT: 2009 International Symposium on Optomechatronic Technologies (2009).

3. D. N. Wang, Y. Wang, and **M. Yang**, "Microhole-structured long period fiber grating," BGPP2010: Bragg Gratings, Photosensitivity, and Poling in Glass Waveguides (2010).

4. C. R. Liao, Ying Wang, D. N. Wang, and **M. Yang**, "Multi-parameter sensor using fiber In-line MZ Interferometer Embedded in Fiber Bragg Grating," EWOFS2010, Fourth European Workshop on Optical Fibre Sensors (2010).

5. **M. Yang**, D. N. Wang, and C. R. Liao, "Micro-holes integrated fiber Bragg grating for simultaneous and independent refractive index and temperature measurement," ACP2010: Asia Communications and Photonics Conference and Exhibition (2010).

6. **M. Yang**, D. N. Wang, Y. Wang, and C. R. Liao, "Fiber in-line Mach-

Zehnder interferometer based on selective infiltration of photonic crystal fiber," The 21st International Conference on Optical Fiber Sensors, Proc. SPIE, **7753-276** (2011).

7. C. R. Liao, D. N. Wang, X. Y. He, and **M. Yang**, "Twisted optical microfiber for refractive index sensing," The 21st International Conference on Optical Fiber Sensors, Proc. SPIE, **7753-293** (2011).

Acknowledgements

Contents

List of Figures

temperature in the RI liquid (circles: measured intensity I_0; line: calculated intensity I_1) (b) FBG resonant wavelength shift versus temperature (circles: experiment; line: linear fitted).

traced fringe dip (b) transmission spectra when PCF length is 1.8 cm, circles: traced fringe dip (c) traced fringe dip wavelength shift for different PCF length: circles, 3.4 cm; squares: 1.8 cm; lines: linear fitted.

Figure 6.16 Simulation of the thermo coefficients of the core LP_{01} mode (circles) and the hybrid mode (squares); lines: linear fit of the simulation results.

List of Tables

Chapter 1 Introduction

1.1   Literature Review

1.1.1 Development of Femtosecond (Fs) Pulse Laser Technology

Lasers with ultrashort pulse duration have always been a research frontier of physics since the first demonstration of a passive mode locking picosecond (ps) ruby laser in the mid of 1960s [1]. The development process of ultrashort pulse laser is shown in Fig. 1.1 [2]:
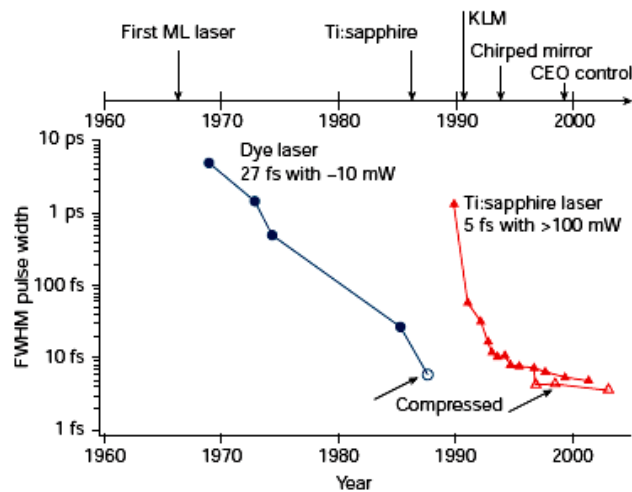
Fig. 1.1 Development of ultrashort pulse lasers [2].

The development process includes three stages: (1) nanosecond (ns) stage, from the mid of 1960s to the later 1970s, in which diverse mode locking theories and experimental technologies have been investigated; (2) ps stage, from the later 1970s to the 1980s, in which preliminary applications of ultrashort pulse laser in physics and chemistry have been investigated; and (3) fs stage, from the 1980s till now, in which the pulse duration has been shortened to the level of fs. During the last decades, the fast development of ultrashort pulse laser has enabled pulse

duration continuously decreasing to the level as small as 2.6 fs [3].

The first demonstration of fs laser is based on the mechanism of colliding pulse mode locking (CPM) in organic dye material [4], which has the disadvantage of a complicate maintaining process of the dye laser and thus could hardly be used for wide applications. Until later 1980s, with the development of crystals growth technology, novel kinds of solid gain materials such as Ti: Sapphire has been fabricated, which has a wide gain bandwidth and thus is suitable for generation of fs laser pulses [5]. Various mode locking techniques have been developed [6-9]. Among them, the Kerr lens mode locking (KLM) technique developed based on the Kerr effect of Ti: Sapphire itself without any external mode locking element is a great improvement of fs laser technology [10, 11], which can decrease the pulse duration to several fs [3, 12-14]. However, self-starting of KLM is rather difficult, which requires a very strict working environment [15, 16]. As an alternation, the application of semiconductor saturable absorber mirrors (SESAM) enables the KLM easily self-start and work stably for long time [17]. Nearly all types of solid-state ultrashort laser can self-start by use of SESAM [13, 17-18].

Nowadays, the main research focus of ultrashort pulse laser are: (1) shorter pulse duration; (2) higher pulse peak power; (3) higher average power; and (4) higher repetition rate. Due to the higher order dispersion, the pulse duration is in the order of 10 fs for a Ti: Sapphire fs laser that uses fused silica prisms [19-21]. However, through well designed chirp mirrors with proper dispersion control, the pulse duration can be further decreased, while maintains a good spatial beam quality of the laser pulses [22-27]. For high peak power generation, the chirped pulse amplification (CPA) technique is applied [28], as shown in Fig. 1.2 [29]:
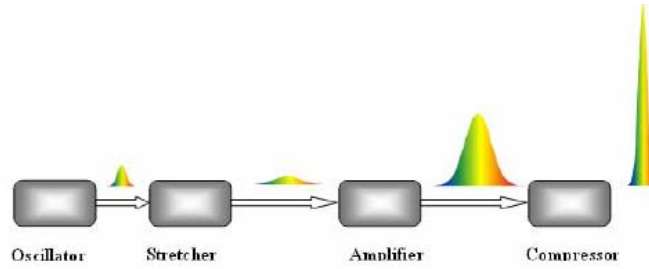
Fig. 1.2 Illustration of the CPA process [29].

The CPA process includes: (1) the stretch of fs pulses to ns pulses; (2) the amplification of the ns pulses; and (3) the compression of the ns pulses to fs pulses. The stretch and compression of the pulses are achieved by diffraction gratings or pairs of prisms. This technique can overcome the amplification difficulties of gain materials in solid-state lasers while protects the components that may be easily damaged by ultrahigh pulse peak power, and thus has been widely used in ultrashort pulse laser system including the system used in this thesis. A typical fs laser system is composed of the following components: an oscillator, a stretcher, an amplifier and a compressor. By the CPA technique, the pulse peak power can be increased to the level of 10^{15} W [30].

Laser diode pumped mode locking fs laser has achieved an high average power of 60 W recently [31]. Until now, the largest average power is achieved in a disk laser [32], which greatly reduces the thermal effect and is capable of absorbing powers from multiple pump sources simultaneously. The combination of SESAM and disk can be further optimized to increase the average power. The increase of average power will have few disadvantages in beam properties, Q-switch instability or damage to the SESAM. Meanwhile, the optimized SESAM has already achieved tunable ultrashort pulses repetition rate in the order of several tens of GHz [33-35], and the repetition rate can still be enhanced.

In general, due to the advantages of ultrashort pulse duration, the high repetition rate, the broadband spectrum and the ultrahigh pulse peak power, fs laser has wide applications in detection of physical or chemical processes within an

ultrashort time scale; high speed telecommunication system with large capacity; optical coherence tomography with high resolution; micro operation for medical research and many others. The next section will focus on one of the important applications of fs laser: micro-machining.

1.1.2 Review of Fs Laser in Micro-machining

1.1.2.1 Properties of Fs Laser Micro-machining

Compared with conventional machining processes, laser assisted machining has the advantages of non-contact, good machining quality, high flexibility and easiness of automation. With the development of laser technology, applications of laser in machining has gained significant progress, including hole drilling, line cleaving, welding, quenching, engraving and materials surface processing. For example, continuous wave (CW) or long pulse duration lasers, such as Nd: YAG and CO_2 laser, have already been used in vehicle and chemical industries.

With the maturation of commercialized fs laser system, fs laser micro-machining has also been employed intensively in material operation. Compared with CW or long pulse duration lasers, fs laser has initiated many new machining fields, such as high precision, small destruction, spatial 3 dimensional (3D) internal processing. In general, fs laser machining has the following novel properties:

(1) Small machining dimension. The transverse dimension of laser focus spot and thus the machining result is always larger than the laser wavelength due to the diffraction limit which fs laser also obeys. However, due to the ultrahigh pulse peak power of fs laser, the normally involved nonlinear absorption of photon energy will result in that the material damage strongly dependent on the laser energy and its spatial intensity distribution. The fs laser normally has a spatial Gaussian distribution, which has its strongest intensity at the focus spot center and quickly decreases along the focus spot radius. Therefore, through

precisely adjusting the pulse energy when only the laser power intensity at the focus spot center could achieve the material damage threshold, one can obtain a sub-micro machining dimension, which is much smaller than the entire focus spot size. For example, periodical structures with nm scale can be fabricated on SU-8 material through a two-photon absorption process [36].

(2) Less thermal effect during the laser operation process. The ultrahigh pulse peak power and ultrashort pulse duration enable fs laser to interact with materials with little energy diffusion. This can help to eliminate the usually involved defects in laser machining such as material melting, thermal diffusion and shockwave. Moreover, the emitted ions have the same charge polarity as the electron plasma generated, which prevents re-contamination of the machining surface. Therefore, the fs laser machined surface has a much smoother morphology compared with that machined by long pulse duration lasers [37].

(3) Capability of internal 3D machining of transparent materials. Since transparent materials do not linearly absorb the fs laser energy, the laser energy could transmit to the internal focus point with little loss. Therefore, by carefully adjusting the laser energy, internal machining of transparent materials could be achieved while leaving the surface unaffected [38].

(4) Diversity of machining materials and low energy assumption. Due to the different absorption process of fs laser energy, the materials under operation have deterministic threshold energy. The ablation of material strongly depends on the laser pulse energy. Laser energy absorption and ablation threshold energy only depend on the atom properties of the material, which has nothing to do with the free carrier concentration in the material. Therefore, fs laser with ultrashort pulse duration and enough pulse energy can machine any kinds of materials, such as silica, ceramics, semiconductors, polymers, biological tissues [36-39].

1.1.2.2   Applications of Fs Laser for Micro-machining

Based on these advantages, the fs laser has been widely applied in micro-

machining. In this section, several typical applications of fs laser micro-machining are listed, while the micro-structures in optical fiber fabricated by fs laser micro-machining are reviewed in section 1.1.3.2.

(1) Optical storage [40, 41]. By focusing fs laser inside the material, internal voids with diameters smaller than the diffraction limit can be fabricated. Multiple of such voids can form compact point arrays which form optical storing media with high density. The stored message can be read out by either the phase contrast microscope image or the light scattering of each micro voids.

(2) Micro photonic devices [42-44]. Different kinds of micro photonic devices, including waveguides, beam splitters, diffraction gratings, photonic arrays, reflectors and many others can be directly fabricated by refractive index (RI) change induced by fs laser irradiation. The devices can have either 2D or 3D structures and locate inside the materials. No strict restriction exists for the fabrication materials.

(3) Micro-electronics [45]. The fs laser can repair defects of photomasks, fabricate new photomasks quickly, and make micro-holes in the wafer easily, which can help to shorten the fabrication time and reduce the encapsulation dimension in the fabrication process of micro-electronics circuits. Besides, the substrate wafer may not be significantly damaged as the thermal effect is small during the fs laser micro-machining process.

(4) Medical and biological applications [46]. The property of little thermal effect has enabled fs laser as a powerful tool for laser surgery. Besides, the capability of internal 3D micro-machining has enabled fs laser for direct small invasive surgery of important organs without hurting the outside tissues.

1.1.3 Review of Optical Fiber Sensors (OFS)

1.1.3.1　Conventional OFS

Optical fiber devices (OFD) for providing certain functions have long been

developed since the first demonstration of optical fiber with low transmission loss. OFD can be divided into active or passive devices. Active devices require external control or input optical power, while passive devices operate without a source of energy supply. Typical active OFD include phase modulator, amplifier, frequency shifter, while passive OFD include polarizer, directional coupler, filter, multiplexers/demultiplexer, Farady rotator, attenuator, and so on [47].

Among various kinds of OFD, optical fiber sensors (OFS), which can response to a wide variety of measurands, have received significant research attention [48]. Compared with traditional electronic or mechanical sensors, OFS possesses the certain advantages of light weight, small size, low cost, high sensitivity, immunity to electromagnetic interference, and ease of multiplexing for distributing applications [49]. Different types of OFS and OFS fabricating and sensing technologies have been developed since the first original prototype of using optical fiber as the sensing element in the mid 1970s, including fiber interferometer, fiber Bragg grating (FBG), long period fiber grating (LPFG), fiber scattering reflection, distributed OFS, FBG laser sensor, and many others, being introduced by enormous review articles and books [48-55]. Up until present, OFS have wide applications in sensing different kinds of measurands, such as temperature, strain, humidity, vibration, rotation, pressure, acoustic emission, voltage/current/magnetism, biologics, chemicals and gases [48-55].

OFS are usually designed to possess a sensing head, which can response to the change of the interested sensing measurands. The responding sensing signal is generated from the change of beam properties in fiber, such as wavefront phase, modes dispersion, transmission intensity, and polarization state. The sensing heads normally have a certain length to either enhance the sensitivity or spatially average the sensing measurands. In general, there are two types of OFS configurations [48]. For the first type, the interested measurands usually locate at a certain position, which indicates a point sensing. The other type of OFS

configuration, called the distributed sensing, can discriminate individual measurands at different spatial locations by multiplexing several sensing heads along one fiber length. The typical requirements for the sensing head of OFS are high sensitivity, low noise interference, compact in size for encapsulation, and easiness in demodulation of the responding sensing signal.

1.1.3.2　Micro-structured OFS Fabricated by Fs Laser

Fs laser has already been applied for fabricating different kinds of OFS in the recent years. A typical application is the FBG inscribed in normal single mode fiber (SMF). FBG can reflect the forward propagation light backward at certain wavelength (Bragg wavelength), which can form a narrow bandwidth filter. This property, together with the low insertion loss, makes FBG an important OFD for optical communication, sensing and fiber laser [48]. FBG are normally inscribed by ultraviolet (UV) laser, which requires increasing the fiber photosensitivity through hydrogen loading. Besides, UV inscription also requires a usually expensive phase mask with its period fixed for only one Bragg wavelength. Instead, through a point-by-point inscription method, fs laser can induce periodical RI change in the core, with a fast inscription speed as 1 mm/s [56, 57]. This inscription method requires no photosensitivity of fiber. And by changing the fiber movement speed, FBG with different periods can be fabricated without the existence of any phase masks. Different grating orders, including the first and the second order FBG, can be fabricated [56-58]. The microscope image of the first and the second order FBG are shown in Fig. 1.3 [58].
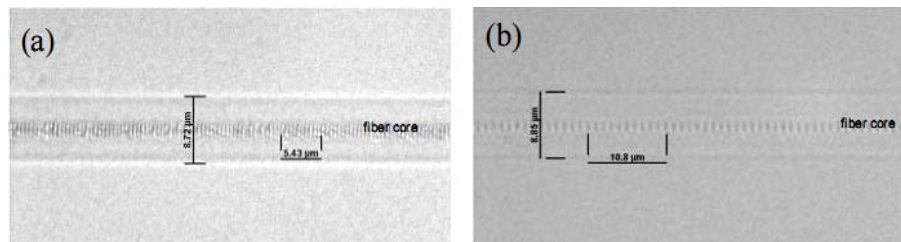
Fig 1.3 Fs laser point-by-point inscribed FBG (a) first order (b) second order [58].

The highly precise ablation property of fs laser has also enabled it in micro-machining on optical fiber. Together with the hydrofluoric acid (HF) etching technique, a micro-channel with the diameter of several μm can be fabricated into the core center of SMF [59]. The small pulse energy (< 1 μJ) can result in a pattern into the fiber without significant structural destruction, which may result from either the fs laser induced RI change or extremely small material damage. This pattern is much more quickly etched away by HF than the unaffected fiber and forms a micro-channel, which induces scattering loss and thus is sensitive to the RI of the liquid filled in it. By use of the same method, a micro-slot along the fiber longitudinal direction can also be fabricated through line scanning of the fs laser focus point. The micro-slot locates in half of the core region, and forms a hybrid waveguide with the remaining half core when filled with liquid, which can also be applied as a refractometer [60]. The morphology of the micro-channel and micro-slot are shown in Fig. 1.4 (a) and (b), respectively [59, 60].
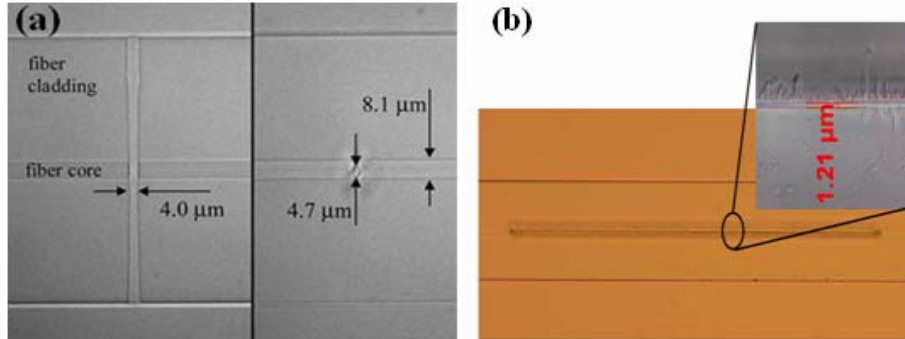
Fig 1.4 Fs laser inscribed (a) micro-channel (b) micro-slot [59, 60].

Another micro-structure based OFS fabricated by fs laser line scanning is the micro-cavity which removes the fiber core by certain length. This micro-cavity can form a Fabry-Perot interferometer (FPI) with compact device dimension, as shown in Fig. 1.5 [61-64]. By polishing the cavity surface smooth, the visibility of the FPI can be increased to over 10 dB. This device can be applied for sensing of water solution with small temperature-RI cross sensitivity [64].
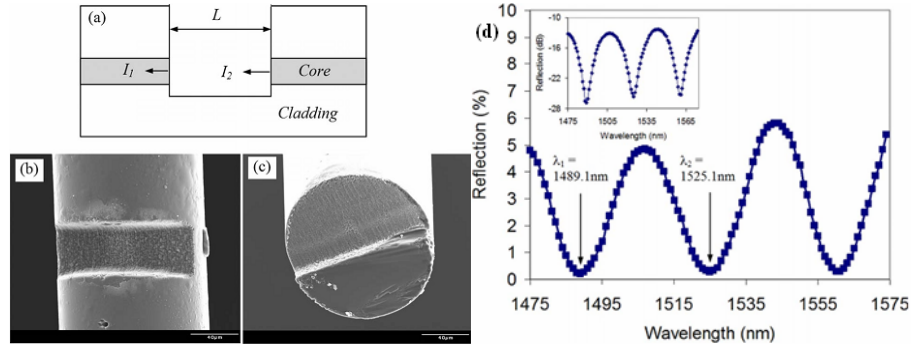
Fig 1.5 Fs laser inscribed FPI in SMF (a) schematic figure (b) top view (c) cross section view (d) reflective spectrum [61-64].

The property of internal 3D micro-machining of fs laser can help to fabricate 3D micro-structure with dimension scale of μm. For example, through a two-step process including fs laser ablation and cleaving, a prototype of cantilever with thickness of ~20 μm on the fiber tip can be fabricated, as shown in Fig. 1.6 [65].
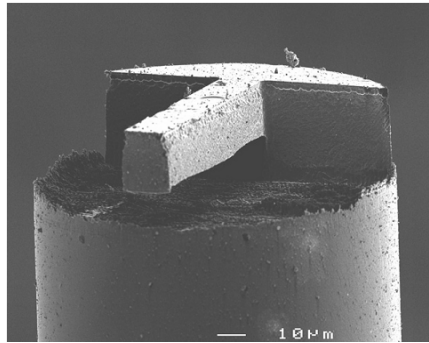
Fig 1.6 Fs laser 3D micro-machined cantilever on fiber tip [65].

During recent years, fs laser has also been used for fabricating LPFG [66-68]. The LPFG fabricated by infrared fs laser has a supreme thermal stability [66] and thus possesses potential applications as high temperature sensors. LPFG in photonic crystal fiber (PCF) with single side RI modulation is also developed by fs laser micro-machining, which can be applied as directional bending sensor sensitive to both the bending curvature and bending direction [68].

When fs laser directly irradiates the fiber cross section facet, a cone shape micro-hole with certain depth will be fabricated. By circularly irradiating, these cone micro-holes can together compose a micro-cavity. After fusion splicing

with another cleaved SMF, cladding mode will be generated by the cavity and interferes with the core mode directly propagating through the cavity. Thus a fiber-inline Mach-Zehnder interferometer (MZI) is fabricated based on a compact internal micro-structure, as shown in Fig. 1.7 [69]. The cavity dimension, including its length and diameter, can be adjusted by changing the fs laser pulse energy. After fusion splicing, this device could sustain more mechanical stress compared with FPI in [61-64].
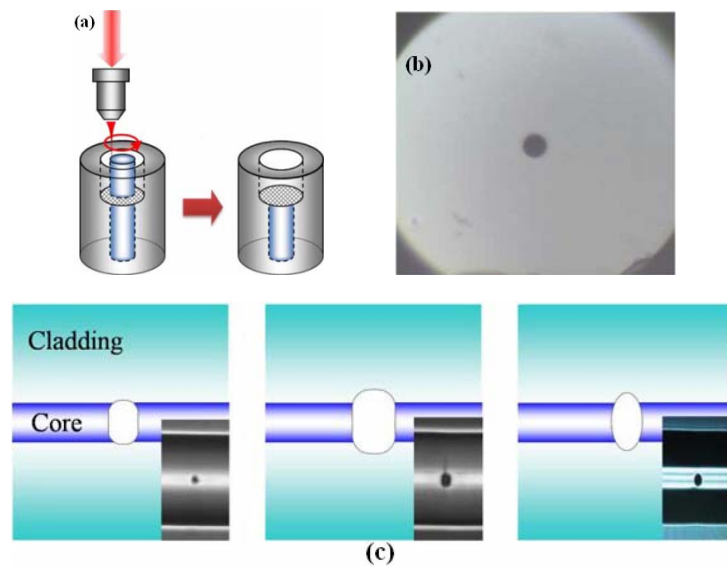
Fig 1.7 Fiber-inline MZI based on internal micro-cavity fabricated by fs laser (a) schematic fabrication process (b) cross section view (c) different cavity dimensions [69].

With the development of novel types of optical fiber, such as PCF, photonic bandgap fiber (PBGF), micro capillary fiber, and hollow core fiber, fs laser micro-machining for novel micro-structure OFS will have more applications.

1.2   Motivation and Significance of This Work

The various and unique advantages of fs laser micro-machining have enabled it as a powerful and widely used tool for micro-machining on bulk glass, metals, polymers, semiconductors and even biological tissues. The precise control of fs laser energy and focus point location can make desired micro-structure more accurately, easily, and controllably than conventional laser machining techniques.

The fs laser micro-machining technique thus opens a way for fabricating novel kinds of OFS based on micro structural change in optical fiber. Many works have been reported on this field. These micro-structures can be applied for sensing different measurands, with advantages of high sensitivities and a much more compact device dimension (in the order of tens of μm) compared with normal OFS, which enables an intrinsic point sensing.

This thesis proceeds with the work of fabrication and application of novel kind micro-structures by use of fs laser micro-machining. The fs laser micro-machining system is built up for a flexible and convenient control of the parameters for fs fabrication process on optical fiber. By use of this system, a micro-hole can be fabricated through stationary fs laser irradiation and a micro-cavity can be fabricated through fs laser scanning along the fiber longitudinal direction. This thesis also undertakes the potential applications of complicated micro-structures, such as structural modulated LPFG by periodically position multiple micro-holes along the fiber length and FBG sensor integrated with micro-holes. These works enhances the possibility for integrating different kinds of micro-structures in one fiber for sensor applications. Finally, the fs laser assisted selective infiltration technique is developed. This technique includes two fundamental fs laser micro-machining methods: the stationary irradiation and the line scanning for material cleaving, which provides an application for complicate fs laser micro-machining on optical fiber.

1.3 Thesis Outline

Chapter 2 In this chapter, a general physical process of fs laser interaction with transparent materials is firstly introduced, with detailed discussion on ionization, energy absorption and material ablation mechanism. Then in section 2.2, the fs laser micro-machining system setup for the work of this thesis is described in details in terms of the function of each component. Finally, section 2.3 discusses

the focusing geometry of the spatial Gaussian distributed fs laser beam by microscope objective lens, which provides guidance for the remaining work.

Chapter 3 In section 3.1, a novel kind of RI sensor by direct drilling a micro-hole in fiber with fs laser micro-machining is presented, and the different fabrication parameters with their corresponding micro-hole dimensions and morphologies are compared. Then, in section 3.2, individual RI responses of micro-holes with different dimensions are presented and analyzed both qualitatively and quantitatively, with a small temperature-RI cross sensitivity obtained for one type micro-hole. Finally in section 3.3, a micro-cavity is fabricated into optical fiber by fs laser line scanning. With proper deviation distance to the core center, this micro-cavity can form a novel kind of fiber-inline MZI and can be applied as high temperature sensor with good thermal stability or RI sensor with extremely large sensitivity.

Chapter 4 The coupled local mode theory is introduced for LPFG with strong waveguide variation and a general discussion of mode coupling mechanism based on RI modulation and the mode field property of LPFG is introduced in section 4.1 with a CO_2 laser irradiation model. After then, by periodically drilling micro-holes along the fiber length, either symmetrical or asymmetrical located, a novel kind of structural modulated LPFG can be effectively fabricated in different kinds of fiber, such as all solid PBGF and SMF, which are shown in section 4.2 and 4.3, respectively. The mode field properties, the phase matching curves and the applications as RI sensors are also performed in these sections. Finally, section 4.4 briefly discusses the fabrication geometry error during the micro-machining process.

Chapter 5 The fabrication of FBG sensor integrated with micro-holes is presented in section 5.1. The individual RI and temperature performances are shown in section 5.2. This device also has a small temperature-RI cross

sensitivity, which can be applied as simultaneous temperature and RI sensor, as shown in section 5.3. A brief discussion concerning the device performance is presented in section 5.4.

Chapter 6 With the assistance of fs laser, a novel technique for selective infiltrating liquid into air holes of PCF is achieved and illustrated in section 6.1, with excellent flexibility and reliability. Two kinds of sensor devices are developed with this technique. In section 6.2, a directional mode coupler device is developed as ultra sensitive temperature sensor, with its phase matching curves, mode field property and the temperature sensitivity simulated. In section 6.3, a novel fiber-inline MZI device is developed which can also be applied as highly sensitive temperature sensor. The device performances, including the interference fringe free spectral range (FSR) and the temperature sensitivity are numerically simulated and compared with experimental results.

Chapter 7 In this chapter, all the research works of this thesis is summarized in section 7.1. In section 7.2, a brief discussion on the potential improvements and future research interests is presented.

References for Chapter 1

1. T. Dustech, "Mode-locking effects in an internally modulated ruby laser," Appl. Phys. Lett. **7**, 80-82 (1965).
2. U. Keller, "Recent developments in compact ultrafast lasers," Nature **424**, 831-838 (2003).
3. E. Matsubara, K. Yamane, T. Sekikawa, et al, "Generation of 2.6 fs optical pulses using induced-phase modulation in a gas-filled hollow fiber," J. Opt. Soc. Am. B **24**, 985-989 (2007).
4. R. L. Fork, B. I. Greene, C. V. Shank, "Generation of optical pulses shorter

than 0.1 psec by colliding pulse mode locking," Appl. Phys. Lett. **38**, 671-672 (1981).

5. P. F. Moulton, "Spectroscopic and laser characteristics of Ti:Al$_2$O$_3$," J. Opt. Soc. Am. B **3**, 125-132 (1986).

6. R. Roy, P. A. Schulz, A. Walther, "Acousto-optic modulator as an electronically selectable unidirectional device in a ring laser," Opt. Lett. **12**, 672-674 (1987).

7. N. Sarukura, Y. Ishida, H. Nakano, et al, "CW passive mode locking of a Ti:sapphire laser," Appl. Phys. Lett. **56**, 814-815 (1990).

8. P. M. W. French, S. M. J. Kelly, J. R. Taylor, "Mode locking of a continuous-wave titanium-doped sapphire laser using a linear external cavity," Opt. Lett. **15**, 378-380 (1990).

9. K. Naganuma, K. Mogi, "50-fs pulse generation directly fron a colliding-pulse mode-locked Ti:sapphire laser using an antiresonant ring mirror," Opt. Lett. **16**, 738-740 (1991).

10. D. E. Spence, P. N. Kean, W. Sibbett, "60-fsec pulse generation from a self-mode-locked Ti:sapphire," Opt. Lett. **16**, 42-44 (1991).

11. H. A. Haus, J. G.Fujimoto, E. P. Ippen, "Structures for additive pulse mode locking," J. Opt. Soc. Am. B **8**, 2068-2076 (1991).

12. A. Stingl, M. Lenzner, Ch. Spielmann, et al, "Sub-10-fs mirror-dispersion-controlled Ti:sapphire laser," Opt. Lett. **20**, 602-604 (1995).

13. I. D. Jung, F. X. Kärtner, N. Matuschek, et al, "Self-starting 6.5 fs from a KLM Ti:sapphire laser," Opt. Lett. **22**, 1009-1011 (1997).

14. K. Yamane, Z. Zhang, K. Oka, et al, "Optical pulse compression to 3.4 fs in the monocycle region by feedback phase compensation," Opt. Lett. **28**, 2258-2260 (2003).

15. G. Cerullo, S. De Silvestri, V. Magni, "Resonators for Kerr-lens mode-locked femtosecond Ti:sapphire lasers," Opt. Lett. **19**, 807-809 (1994).

16. G. Cerullo, S. De Silvestri, V. Magni, "Self-starting Kerr lens mode-locking of a Ti:sapphire laser," Opt. Lett. **19**, 1040-1042 (1994).

17. U. Keller, D. A. B. Miller, G. D. Boyd, "Solid-state low-loss in tracavity saturable absorber for Nd:YLF lasers:An antiresonant semiconductor Fabry-Perot saturable absorber," Opt. Lett. **17**, 505-507 (1992).

18. V. L. Kalashnikov, D. O. Krimer, I. G. Poloyko, "Soliton generation and picosecond collapse in solid-state lasers with semiconductor saturable absorbers," J. Opt. Soc. Am. B **17**, 519-523 (2000).

19. M. T. Asaki, C. Huang, D. Garvey, et al, "Generation of 11-fs pulses from a self-mode-locked Ti:sapphire laser," Opt. Lett. **18**, 977-979 (1993).

20. P. F. Curley, Ch. Spielmann, T. Brabec, et al, "Operation of a femtosecond Ti:sapphire solitary laser in the vicinity of zero group delay dispersion," Opt. Lett. **18**, 54-56 (1993).

21. J. Zhou, G. Taft, C. Huang, et al, "Pulse evolution in a broad-bandwidth Ti:sapphire laser," Opt. Lett. **19**, 1149-1151 (1994).

22. R. Szipöcs, K. Ferencz, C. Spielmann, et al, "Chirped multilayer coatings for broadband dispersion control in femtosecond lasers," Opt. Lett. **19**, 201-203 (1994).

23. A. Stingl, M. Lenzner, Ch. Spielmann, et al, "Sub-10-fs mirror-dispersioncontrolled Ti: sapphire laser," Opt. Lett. **20**, 602-604 (1995).

24. F. X. Kärtner, N. Matuschek, T. Schibli, et al, "Design and fabrication of double-chirped mirrors," Opt. Lett. **22**, 831-833 (1997).

25. N. Matuschek, F. X. Kärtner, U. Keller, "Analytical design of double-chirped mirrors with customtailored dispersion characteristics," IEEE J. Quantum Electron. **35**, 129-137 (1999).

26. N. Matuschek, L. Gallmann, D. H. Sutter, et al, "Back-side coated chirped mirror with ultra-smooth broadband dispersion characteristics," Appl. Phys. B **71**, 509-522 (2000).

27. G. Steinmeyer, D. H. Sutter, L. Gallmann, et al, "Frontiers in ultrashort pulse generation: pushing the limits in linear and nonlinear optics," Science **286**, 1507-1512 (1999).

28. Donna Strickland, G. Mourou, "Compression of amplified chirped optical

pulses," Opt. Commun. **55**, 447-449 (1985).

29. M. Nisoli, S. De Silvestri, O. Svelto, et al, "A novel high-energy pulse compression system: Generation of multigigawatt sub-5-fs pulses," Appl. Phys. B **65**, 189-196 (1997).

30. M. Aoyama, K. Yamakawa, Y. Akahane, et al, "0.85-PW, 33-fs Ti: sapphire laser," Opt. Lett. **28**, 1594-1596 (2003).

31. E. Innerhofer, T. Südmeyer, F. Brunner, et al, "60 W average power in 810-fs pulses from a thin-disk Yb:YAG laser," Opt. Lett. **28**, 367-369 (2003).

32. A. Giesen, H. Hügel, A. Voss, et al, "Scalable concept for diode-pumped high-power solid-state lasers," Appl. Phys. B **58**, 365-372 (1994).

33. L. Krainer, R. Paschotta, G. J. Spiihler, et al, "Tunable picosecond pulse-generating laser with a repetition rate exceeding 10 GHz," Electron. Lett. **28**, 225-227 (2002).

34. A. Rousse, C. Rischel, S. Fourmaux, et al, "Non-thermal melting in semiconductors measured at femtosecond resolution," Nature **410**, 65-68 (2001).

35. S. C. Zeller, L. Krainer, G. J. Spühler, et al, "Passively modelocked 40-GHz Er: Yb: glass laser," Appl. Phys. B **76**, 787-788 (2003).

36. S. Jeon, V. Malyarchuk, J. A. Rogers, et al, "Fabricating three dimensional nanostructures using two photon lithography in a single exposure step," Opt. Express **14**, 2300-2308 (2006).

37. B. N. Chichkov, C. Momma, S. Nolte, et al, "Femtosecond, picosecond and nanosecond laser ablation of solids," Appl. Phys. A **63**, 109-115 (1996).

38. S. Maruo, K. Ikuta, H. Korogi, "Submicron manipulation tools driven by light in a liquid," Appl. Phys. Lett. **82**, 133-135 (2003).

39. M. D. Perry, B. C. Strart, P. S. Banks, et al, "Ultrafast-pulse laser machining of dielectric materials," J. Appl. Phys. **85**, 6803-6810 (1999).

40. E. N. Glezer, E. Mazur, "Ultrafast-laser driven micro-explosions in transparent materials," Appl. Phys. Lett. **71**, 882-884 (1997).

41. E. N. Glezer, M. Milosavljevic, L. Huang, et al, "Three-dimensional optical

storage inside transparent materials," Opt. Lett. **21**, 2023-2025 (1996).

42. K. Hirao, K. Miura, "Writing waveguides and gratings in silica and related materials by a femtosecond laser," J. Non-Crystalline Solids **239**, 91-95 (1998).

43. J. Siegel, J. M. Fernández-Navarro, A. García-Navarro, et al, "Waveguide structures in heavy metal oxide glass written with femtosecond laser pulses above the critical self-focusing threshold," Appl. Phys. Lett. **86**, 121109-1-3 (2005).

44. M. Hughes, W. Yang, D. Hewak, "Fabrication and characterization of femtosecond laser written waveguides in chalcogenide glass," Appl. Phys. Lett. **90**, 131113-1-3 (2007).

45. K. Venkatakrishnan, B. K. A. Ngoi, P. Stanley, et al, "Laser writing techniques for photomask fabrication using a femtosecond laser," Appl. Phys. A **74**, 493-496 (2001).

46. T. Juhasz, G. Djotyan, F. H. Loesel, et al, "Applications of femtosecond lasers in corneal surgery," Laser Physics **10**, 495-500 (2000).

47. P. Goure, I. Verrier, *Optical Fibre Devices*, Institute of Physics Publishing: Bristol, 2002.

48. A. D. Kersey, "A review of recent developments in fiber optic sensor technology," Optical Fiber Technology, **2**, 291-317 (1996).

49. B. Lee, "Review of the present status of optical fiber sensors," Optical Fiber Technology, **9**, 57-79 (2003).

50. K. T. V. Grattan, B. T. Meggitt, *Optical Fiber Sensor Technology*, Kluwer Academic publisher: Boston (1999).

51. B. Culshaw, J. Dakin, *Optical Fiber Sensors*, Artech House: Boston, (1988).

52. F. T. S. Yu, S. Yin, *Fiber Optic Sensors*, Dekker: New York (2002).

53. A. Othonos, K. Kalli, *Fiber Brag Gratings-Fundamentals and Applications in Telecommunications and Sensing*, Artech House: Boston (1999).

54. C. K. Kirkendall, A. Dandridge, "Overview of high performance fiber-optic sensing," J. Phys. D **37**, 197-216 (2004).

55. T. G. Giallorenzi, J. A. Bucaro, A. Dandridge, et al, "Optical fiber sensor technology," IEEE J. Quantum Electron. **18**, 626-65 (1982).

56. Y. Lai, A. Marinez, I. Khrushchev, et al, "Distributed Bragg reflector fiber laser fabricated by femtosecond laser inscription," Opt. Lett. **31**, 1672-1674 (2006).

57. K. Feng, J. Cai, V. Grubsky, et al, "Dynamic dispersion compensation in a 10 Gbit/s optical system using a voltage controlled tuned nonlinearly chirped fiber Bragg grating," IEEE Photon. Technol. Lett. **11**, 373-375 (1999).

58. Y. Lai, K. Zhou, K. Sugden, et al, "Point-by-point inscription of first-order fiber Bragg grating for C-band applications," Opt. Express **15**, 18318-18325 (2007).

59. Y. Lai, K. Zhou, I. Bennion, "Microchannels in conventional single-mode fibers," Opt. Lett. **31**, 2559-2561 (2006).

60. K. Zhou, Y. Lai, X. Chen, et al, "A refractometer based on a micro-slot in a fiber Bragg grating formed by chemically assisted femtosecond laser processing," Opt. Express **15**, 15848-15853 (2007).

61. Y. Rao, M. Deng, D. Duan, et al, "Micro Fabry-Perot interferometers in silica fibers machinded by femtosecond laser," Opt. Express **15**, 14123-14128 (2007).

62. Z. L. Ran, Y. J. Rao, W. J. Liu, et al, "Laser-micromachined Fabry-Perot optical fiber tip sensor for high-resolution temperature-independent measurement of refractive index," Opt. Express **16**, 2252-2263 (2008).

63. T. Wei, Y. Han, H. Tsai, et al, "Miniaturized fiber inline Fabry-Perot interferometer fabricated with a femtosecond laser," Opt. Lett. **33**, 536-538 (2008).

64. T. Wei, Y. Han, Y. Li, et al, "Temperature-insensitive miniaturized fiber inline Fabry-Perot interferometer for highly sensitive refractive index measurement," Opt. Express **16**, 5764-5769 (2008).

65. A. A. Said, M. Dugan, S. de Man, et al, "Carving fiber-top cantilevers with femtosecond laser micromachining," J. Micromech. Microeng. **18**, 035005

(2008).

66. Y. Kondo, K. Nouchi, T. Mitsuyu et al, "Fabrication of long-period fiber gratings by focused irradiation of infrared femtosecond laser pulses," Opt. Lett. **24**, 646-648 (1999).

67. A. I. Kalachev, D. N. Nikogosyan, G. Brambilla, "Long-period fiber grating fabrication by high-intensity femtosecond pulses at 211 nm," J. Lightwave Technol. **23**, 2568-2578 (2005).

68. T. Allsop, K. Kalli, K. Zhou, et al, "Long period gratings written into a photonic crystal fibre by a femtosecond laser as directional bend sensors," Opt. Commun. **281**, 5092-5096 (2008).

69. M. Park, S. Lee, W. Ha, et al, "Ultracompact Intrinsic Micro Air-Cavity Fiber Mach–Zehnder Interferometer," IEEE Photon. Technol. Lett. **21**, 1027-1029 (2009).

Chapter 2 Fs Laser Micro-machining Principle and System

The ablation of transparent materials by fs laser comprises a series of complicate physical processes, including nonlinear absorption of photon energy, ionization of materials, generation of plasma, and ablation of materials [1-5]. This chapter will first present a brief review of these physical processes. Some key issues for fs laser ablation, such as the ablation threshold energy and thermo effect will be discussed in detail. Then, the fs laser micro-machining system setup for the rest work in this thesis will be introduced, which includes a commercial fs laser system, an external optical path and a microscope system. The system can conveniently adjust the energy and tailor the spatial spot width of fs laser. Finally, the geometry focusing property of the fs laser beam with spatial Gaussian distribution is discussed, which helps in proper choosing of microscope objective lens (MO).

2.1 Fs Laser Interaction with Transparent Materials

Due to the ultrashort pulse duration, the fs laser pulse can have extremely high pulse peak power and light intensity, even with moderate single pulse energy. This enables fs laser as a powerful tool for ablation of transparent materials, which usually have a high transmission of light with little energy depositing [6-16]. Normally, the generation of high density electron plasma is believed to be the main mechanism for fs laser ablation of materials [2, 17-19]. The generation of plasma is a nonlinear process, which results in the promotion of electrons from the valence band to the conduction band of the material. The high density plasma then can absorb most of the laser energy locally and permanent damage

can occur when enough energy is deposited and transferred to the material and meets the critical electron density. The ablation results depend strongly on the spatial and temporal distribution of the laser energy.

2.1.1 Material Ionization

Two main ionization processes, photoionization and avalanche ionization, stand for material ionization during fs laser ablation process [19-22]. Photoionization means the direct excitation of electrons by the laser field. For transparent materials such as fused silica, the energy of only one photon may not be high enough to promote electrons from the valence band to the conduction band. Therefore, multiple photons must work simultaneously to lead to the excitation of electrons, which is a nonlinear process. Depending on the laser frequency and intensity, photoionization can be divided into multiple photon ionization (MPI) and tunneling ionization according to the adiabatic parameter γ [20]:

$$\gamma = \frac{\omega}{e} [\frac{mcn\varepsilon_0 E_g}{I}]^{1/2} \qquad (2.1)$$

where ω is the laser frequency, I is the laser intensity at the focus spot, m and e are the reduced mass and charge of the electron, n is the material RI, c is the light velocity, ε_0 is the free space permittivity, and E_g is the material bandgap. The γ value determines the regime of photoionization, as shown in Fig. 2.1 [22]:
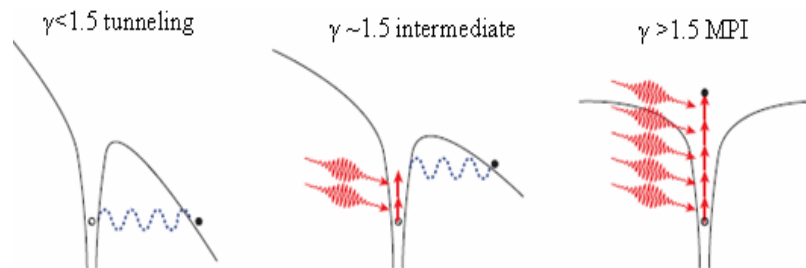
Fig. 2.1 Schematic process of tunneling ionization and MPI [22].

The tunneling ionization ($\gamma<1.5$) stands for the laser with low frequency and strong field. The strong laser field can suppress the Coulomb well significantly

so that the bound electrons can tunnel this small well barrier and become free. On the other hand, when laser frequency is high (but still below the threshold for single photon or linear absorption), MPI ($\gamma > 1.5$) can occur when multiple photons are simultaneously absorbed by the electron, which has a total photon energy larger than the material bandgap and can directly promote an electron from the valance band to the conduction band. In the intermediate regime ($\gamma \sim 1.5$), the ionization process may be a mixture of the two types.

When a free electron (called seed electron) has already existed in the conduction band of the material, it can absorb the laser photon energy sequentially. In order to conserve both the energy and the momentum, this electron must absorb or emit a phonon, or scatter off an impurity [23], which results in an efficient absorption of energy for free carriers through frequent collision with the material lattice [19]. After several photons are absorbed, the energy of the electron exceeds the conduction band minimum at least one bandgap energy. Then, the next collision can ionize another electron to the conduction band. These two electrons are near the conduction band minimum and can be heated by free carrier absorption process, which may ionize more electrons from the valence band sequentially. The seed electrons may result from the thermally excited electrons, easily ionized impurities, or directly photoionization. The illustration of avalanche ionization is shown in Fig. 2.2 [22]:
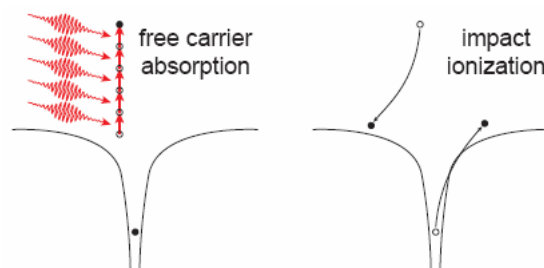
Fig. 2.2 Schematic process of avalanche ionization [22].

The exact ionization process remains a dispute. Earlier studies believe that avalanche ionization is the mechanism for material ablation [24]. Some recent

studies believe that MPI provides the seed electrons while avalanching ionization is still the main ablation mechanism [2, 19, 25-26]. The pulse duration and the power intensity strongly determine the ionization process. In this thesis, the pulse energy used is in the order of several to tens of μJ, the pulse duration is ~120 fs, and the focused laser spot area is in the order of 10^{-7} cm^2, which corresponds to the power intensity in the order of 10^{14} W/cm^2. Such a value shows that the ionization process is a combination of MPI and avalanche ionization, according to the calculation results in Fig. 2.3 [27].
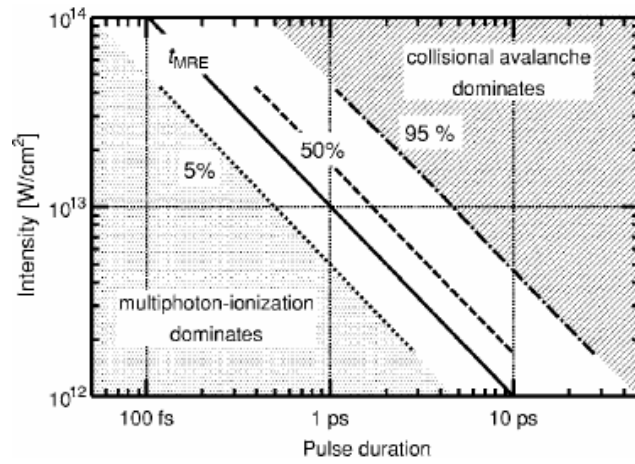
Fig. 2.3 Ionization process depends on pulse intensity and pulse duration [27].

2.1.2 Absorption of Laser Energy

The MPI and avalanche ionization will generate electron plasma, which can absorb laser energy efficiently. The absorption rate and absorption depth are two main parameters to investigate the absorption process. Both of them strongly depend on the plasma density. The absorption rate reaches maximum when the plasma density N increases until the plasma frequency ω_P reaches that of the laser frequency ω, which can be understood by use of a Drude model [22]:

$$\omega_P = [\frac{Ne^2}{\varepsilon_0 m}]^{1/2} \tag{2.2}$$

The absorption rate is then given by [23]:

$$\kappa = \frac{\omega_P^2 \tau}{c(1+\omega^2\tau^2)} \quad\quad\quad (2.3)$$

where c is the light velocity, and τ is the phenomenological Drude scattering time (which means the scattering time of the electron by impurities and phonons) [23]. When enough electron plasma is generated, or the plasma density reaches that of the critical plasma density, permanent damage occurs to the material.

Meanwhile, due to the ultrashort pulse duration, most of the laser energy can only deposit into a shallow layer of materials. The absorption depth is inversely proportional to the electron plasma density, as shown in Fig. 2.4 [22]. For example, for 800 nm radiation laser, when the electron plasma density reaches 10^{21} electrons/cm^3 (typical value of the critical plasma density for fused silica [23]), the absorption depth is in the order of 1 μm. For tight focusing, such as focusing by MO in this thesis, the main absorption region of laser energy belongs to the confocal volume, which is limited by the Rayleigh length of the MO, as discussed later in section 2.4.
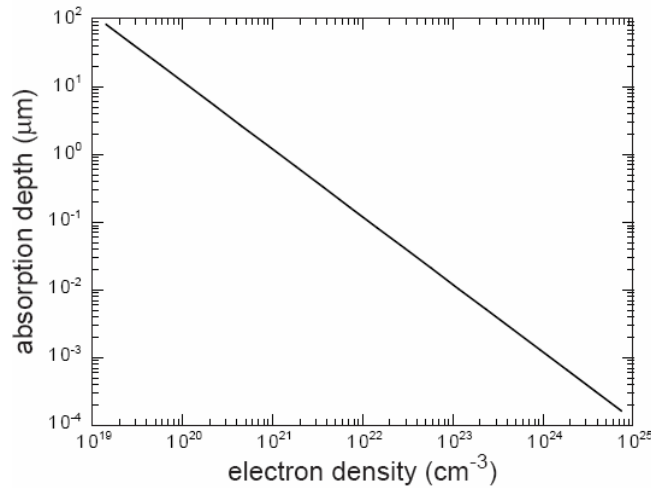
Fig. 2.4 Absorption depth as a function of electron plasma density [22].

2.1.3 Material Ablation

For pulse laser with ultrashort pulse duration, the nonlinear absorption of the

laser energy occurs in an ultrashort time scale compared with the time for energy transferring to the lattice, decoupling the absorption and lattice heating process [28]. Electrons in the conduction band are heated much faster than the time needed to emit phonons, diffuse out of the irradiation region, or recombine with their parent ions. As a result, the electron plasma density will continuously increase until its density matches the critical plasma density [28], and permanent damage or structural change occurs.

As discussed before, for short pulse duration, photoionization provides the seed electrons. This happens in the rising edge of the pulse, while rest of the pulse duration provides the necessary energy for avalanche ionization [28]. Therefore, the breakdown energy of ultrashort laser pulse hardly depends on the material imperfections, which makes the ablation threshold energy deterministic compared with long pulse duration lasers [29]. Meanwhile, due to the extremely high pulse peak intensity, the required pulse energy is much less than that of a long duration pulse, which results in a much more regular and confined material damage morphology [30]. Little energy will deposit into the material out of the focus region and enables a precise ablation.

Two main mechanisms stand for the ablation of materials by ultrashort laser pulses [31, 32]: (1) thermal evaporation, whereas the collision between electrons and phonons heats the lattice locally so as to exceed the evaporation temperature; (2) Coulomb explosion, whereas the electron plasma are shocked by the sequent laser pulses and results in a separation of the charges and ions, which will emit due to the strong electrostatic forces. The two mechanisms coexist during the ablation process, which depends on the pulse intensity, the pulse duration, the pulse number and the material ablation threshold energy [33]. When the pulse energy is much stronger (for example, in the order of several to tens of μJ as in this thesis) than the threshold energy of material ablation, the thermal evaporation dominates the ablation process. The material ablation speed may be

as quick as several μm per pulse, which results in a coarser ablation surface morphology than that of Coulomb explosion [34-36].

2.1.4 Thermal Effect

The large pulse energy (in the order of several to tens of μJ) used in the work of this thesis may lead to significant thermal ablation of the fiber, which makes the ablated surface coarse. The thermal effect comes from the process of electron thermalization, which means the collisions between electrons increase the electron energy to a Femi-distribution level [37]. This process can be described by a two-temperature model, which normally has a time scale of ~100 fs and depends on the laser energy intensity [37]: under strong laser intensity, the electron thermalization has a much faster speed, whereas electrons could transfer energy to lattice by emitting phonons in a much smaller time scale than 100 fs. After the electron thermalization, the lattice will be heated to a state called overheated, which has a temperature much higher than that of the average melting temperature and causes the phase explosion process [38-40]. Meanwhile, the thermal conduct causes heat energy diffusion from the electron plasma to the surrounding materials, which causes melting, evaporation and ablation of the materials out of the laser energy depositing region. However, the thermal effect induced surface roughness is still much smaller compared with longer pulse laser, as the emitting ions will take away most energy deposited in the material.

2.2 Fs Laser Micro-machining System

The micro-machining on optical fiber is a precise process, which needs to accurately position the fiber under ablation and focus the laser beam on to the fiber with errors smaller than the order of several μm. Meanwhile, the pulse energy and the spatial beam property need to be adjusted carefully. The fs laser micro-machining system developed for this purpose is introduced in this section. The system schematic is shown in Fig. 2.5, which includes the following parts:

(1) a commercial fs laser system which generates fs laser pulses; (2) an external optical path which can help adjust the spatial beam diameter and the pulse energy; and (3) a microscope system which can effectively focus laser pulses onto the material under fabrication.
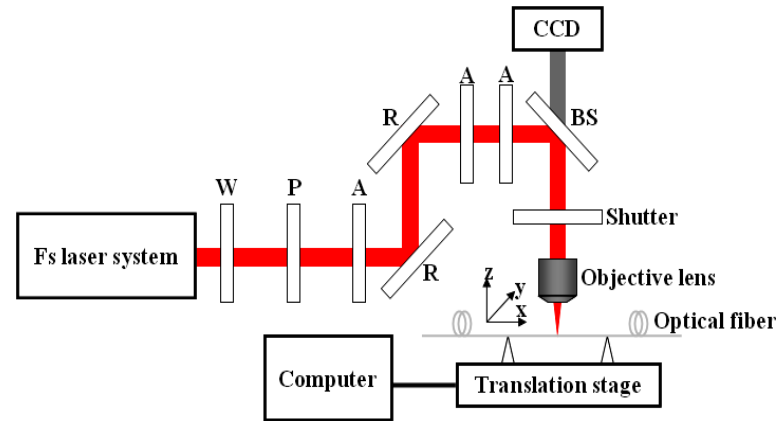
Fig. 2.5 Fs laser micro-machining system: W: half waveplate; P: polarizer; A: aperture; R: reflector; BS: beam splitter; CCD: charged-coupled device camera.

With the help of this micro-machining system, one can adjust proper pulse parameters and micro-machining time for desired micro-structures and observe the fabrication result easily. During the fs micro-machining process, a broadband light source (type ALS-CWDM-FA made by Amonics Ltd.) and an optical spectrum analyzer (OSA, type Ando6139 made by YOKOGAWA Ltd.) are connected at the two ends of the fiber under fabrication, which can monitor the transmission spectrum in real time. Before the experiments, the optical path of the system may need slightly adjustment to achieve the best working condition.

2.2.1 Fs Laser System

The fs laser system used here is a commercialized Ti: Sapphire laser system, consisting of an oscillator (Mai Tai) and an amplifier (Spitfire Pro), made by Spectra-Physics Ltd. The output fs laser is a linear polarized light, with its central wavelength of 800 nm, the pulse duration of 120 fs, a repetition rate of 1 kHz, the maximum single pulse energy of ~1 mJ (which equals to the maximum average power of 1 W). The laser beam is a Gaussian beam with the spatial

TEM$_{00}$ mode, and the 1/e beam radius of $\omega_0 \approx 2$ mm [41]. The CPA technique is applied for the high output power.

2.2.2 External Optical Path

The purpose of the external optical path is to transmit fs laser with proper pulse energy and beam properties before it is focused onto the fiber under machining. The principles for setting the optical path includes: (1) the optical path should change pulse duration as little as possible, which requires using optical components without significant dispersion; (2) the pulse energy needs to be adjusted continuously and conveniently; and (3) spatially filtering of the output fs laser is preferred to remove the aberrations of the laser beam and obtain a clean laser beam which contains only a single spatial mode.

According to these requirements, the external adjusting optical path composes of the following optical components: several reflectors with high reflectivity for 800 nm, a half waveplate, a Glan prism and a small aperture. The reflectors can change the fs laser propagation direction with little transmission loss and dispersion. The Glan prism is a polarizing beam splitter, which acts as a linear polarizer. The half waveplate can change the polarization direction of the linear polarized fs laser. These two components together form an attenuator which can adjust the transmitted pulse energy by rotating the half waveplate and meet the transmission axis direction of the polarizer. In the experiment, the transmitted pulse energy can be adjusted continuously from 1 μJ to 1 mJ. The small aperture can tailor the spatial beam width, which filters out the imperfect optics and stray light of the laser output, and ensures a good beam quality. The output beam after the aperture has a Gaussian distribution of its spatial energy. In this system, the fs laser beam diameter is adjusted to about 5 mm.

2.2.3 Microscope System

The microscope system (Nikon 80i) includes the following components: a pair of apertures for input optical path collimation; three neutral density(with almost no wavelength dependence) attenuators with different attenuation factors (1/4, 1/8, and 1/16) for a precise and versatile adjustment of the on fiber pulse energy; a group of MO with different magnifications for focusing fs laser onto the ablation fiber; and a 3D translation stage controlled by the computer with a tuning resolution of 40 nm. A charge-coupled device (CCD) camera is connected with the MO to monitor the position of the ablation fiber and the fs laser focus spot during micro-machining process. A shutter is mounted before the MO which can conveniently stop laser and thus can control the time of fs laser irradiation onto the ablation fiber.

2.3   Focus of Fs Laser

Besides the pulse energy and irradiation time, the selection of MO for focusing fs laser onto the ablation fiber also has significant influence on the fabricated micro-structure by the micro-machining process. The three main parameters of one MO are its magnification, numerical aperture (NA) and working distances (WD, which is the distance between the MO output and the focal plane), which decides the focus spot diameter and also the focus depth. The microscope system has 4 MO, with their individual parameters listed in Table 2.1.

Table 2.1 Parameters of MO used in the micro-machining system.

Magnification	4×	10×	20×	60×
NA	0.10	0.25	0.50	0.85
WD (mm)	30	7.0	2.1	0.40-0.31

Normally, for a more precise location of the focus point, the MO with a larger magnification is preferred. However, the corresponding larger NA value may lead to a smaller focus point diameter and also a smaller laser focus depth,

which limits the dimensions of the micro-structure that can be fabricated.

Considering the fact that the fs laser is a spatial Gaussian beam, its focusing geometry onto the ablation fiber after the MO can be illustrated in Fig. 2.6 [42]:
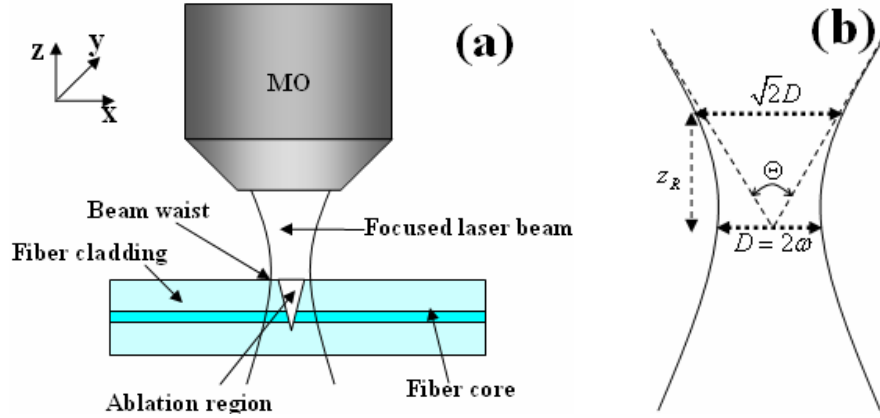
Fig. 2.6 Fs laser focused onto the ablation fiber by MO: (a) schematic geometry (b) spatial geometry of focused Gaussian beam width: beam waist ω; beam diameter at beam waist $D=2\omega$; Rayleigh length Z_R; total spread angle Θ.

The focused Gaussian beam would have its minimum beam radius value of ω at its beam waist. The Rayleigh length Z_R (or Rayleigh range) is defined as the distance from the beam waist to the place where the beam has two times of the spot area as that at the beam waist, which depends on the beam wavelength λ:

$$z_R = \frac{\pi\omega^2}{\lambda} \tag{2.4}$$

Gaussian beam becomes a straight line when it is far away from the beam waist. The total spread angle Θ (in radians) is defined as two times of the angle between that line and the beam central axis:

$$\Theta = 2\frac{\lambda}{\pi\omega} \tag{2.5}$$

The confocal parameter b, or depth of focus of the beam, is defined as:

$$b = 2z_R \tag{2.6}$$

Normally, the focus spot of a Gaussian beam can be characterized as an Airy disk, which determines the diameter D of the focus spot according to the NA

value of the MO, and the wavelength of the beam as [41, 43]:

$$D = 2\omega = 2\frac{\lambda f}{\pi\omega_0} \approx 1.22\frac{\lambda}{NA} \qquad (2.7)$$

where ω_0 is the Gaussian beam width before incident into MO and f is the focal length of the lens. According to Eq. (2.4) ~ (2.7), the beam waist radius ω is inversely proportion to the NA value. Therefore, the larger the NA of the MO, the stronger the spatial power intensity at the focus point when the incident laser energy is kept constant. However, the Rayleigh length Z_R is proportional to the square of ω. For the 4 MO used in this thesis, their different focal diameters at the beam waist, and the corresponding Rayleigh lengths, are listed in Table 2.2.

Table 2.2 Calculated beam waist diameter and Rayleigh length of different MO.

Magnification	4×	10×	20×	60×
D (μm)	9.76	3.90	1.95	1.15
z_R (μm)	93.5	15.0	3.74	1.29

As discussed in section 2.1.2, stronger power intensity at the focus spot will make the materials more easily ionized. However, smaller Rayleigh length may result in a shorter energy absorption depth and thus may limit the depth of the micro-structure that can be fabricated. Meanwhile, the spatial peak energy intensity will decrease more significantly along z-direction for the MO with a larger NA value and the ablation process will stop when the peak energy intensity is smaller than the threshold energy for ablation of silica.

2.4 Summary

The mechanism of fs laser ablation of transparent materials is a very complicated and intrinsically nonlinear physics process, which includes ionization of electrons, laser energy absorption by the electron plasma, generation of high density electron plasma and final ablation of the material. The actual process depends strongly on the laser parameters such as energy intensity, laser wavelength, pulse duration, pulse number and material property.

The ablation occurs when the electron plasma density meets the critical density, which determines the ablation threshold energy and ablation depth. For high intensity pulse energy, thermal damage occurs even in ultrashort pulse duration. These discussions provide the general guidance for the rest work of this thesis.

Besides, the fs laser micro-machining system set up for the remaining work of this thesis is described in this chapter, which can conveniently control the important parameters in fs micro-machining, including the spatial beam diameter, the single pulse energy and the irradiation time onto the ablation fiber. A detailed discussion on the effects of the NA value of the focusing MO is presented, which strongly determines the focused fs laser beam geometry. The ablation dimension is related to the Rayleigh length of the focusing MO, according to the laser intensity along the irradiation direction and laser energy depositing region during the absorption of laser energy.

References for Chapter 2

1. D. Von der Linde, K. Sokolowski-Tinten, J. Bialkowski, "Laser-solid interaction in the femtosecond time regime," Appl. Surf. Sci. **109/110**, 1-10 (1997).

2. X. Liu, D. Du, G. Mourou, "Laser ablation and micromachining with ultrashort laser pulses," J. Quantum Electron. **33**, 1706-1716 (1997).

3. A. Kaiser, B. Rethfeld, M. Vicanek, et al, "Microscopic processes in dielectrics under irradiation by subpicosecond laser pulses," Phys. Rev. B **61**, 11437-11450 (2000).

4. F. Ladieu, P. Martin, S. Guizard, "Measuring thermal effects in femtosecond laser-induced breakdown of dielectrics," Appl. Phys. Lett. **81**, 957-959 (2002).

5. B. N. Chichkov, C. Momma, S. Nolte, et al, "Femtosecond, picosecond and nanosecond laser ablation of solids," Appl. Phys. A **63**,109-115 (1996).

6. L. Petit, N. Carlie, T. Anderson, et al, "Effect of IR femtosecond laser irradiation on the structure of new sulfo-selenide glasses," Opt. Materials, **29**, 1075-1083 (2007).

7. S. Juodkazis, K. Nishimura, H. Misawa, "In-bulk and surface structuring of sapphire by femtosecond pulses," Appl. Surf. Sci. **253**, 6539-6544 (2007).

8. O.G. Kosareva, T. Nguyen, N. A. Panov, et al, "Array of femtosecond plasma channels in fused silica," Opt. Commun. **267**, 511-523 (2006).

9. A. Saliminia, N. T. Nguyen, S. L. Chin, et al, "The influence of self-focusing and filamentation on refractive index modifications in fused silica using intense femtosecond pulses," Opt. Commun. **241**, 529-538 (2004).

10. M. Y. Shen, C. H. Crouch, J. E. Carey, et al, "Formation of regular arrays of silicon microspikes by femtosecond laser irradiation through a mask," Appl. Phys. Lett. **82**, 1715-1717 (2003).

11. A. Ben-Yakar, R. L. Byer, A. Harkin, et al, "Morphology of femtosecond-laser-ablated borosilicate glass surfaces," Appl. Phys. Lett. **83**, 3030-3032 (2003).

12. C. B. Schaffer, A. O. Jamison, E. Mazur, "Morphology of femtosecond laser-induced structural changes in bulk transparent materials," Appl. Phys. Lett. **84**, 1441-1443 (2004).

13. J. W. Chan, T. R. Huser, S. H. Risbud, et al, "Waveguide fabrication in phosphate glasses using femtosecond laser pulses," Appl. Phys. Lett. **82**, 2371-2373 (2003).

14. K. Miura, J. Qiu, T. Mitsuyu, et al, "Preparation and optical properties of fluoride glass waveguides induced by laser pulses," J. Non-Crystalline Solids, **256&257**, 212-219 (1999).

15. C. Florea, K. A. Winick, "Fabrication and characterization of photonic devices directly written in glass using femtosecond laser pulses," J. Lightwave. Technol. **21**, 246-253 (2003).

16. E. N. Glezer, E. Mazur, "Ultrafast-laser driven micro-explosions in

transparent materials," Appl. Phys. Lett. **71**, 882-884 (1997).

17. M. D. Perry, B. C. Stuart, P. S. Banks, et al, "Ultrashort pulse laser machining of dielectric materials," J. Appl. Phys. **85**, 6803-6810 (1999).

18. B. C. Stuart, M. D. Feit, A. M. Rubenchik, et al, "Laser-induced damage in dielectrics with manosecond to subpicosecond pulses," Phys. Rev. Lett. **74**, 2248-2251 (1995).

19. N. Bloembergen, "Laser-induced electric breakdown in solids," IEEE J. Quantum Electron **10**: 375-386 (1974).

20. L. V. Keldysh, "Ionization in the field of a strong electromagnetic wave," Sov. Phys. JETP **28**, 1307-1314 (1965).

21. S. C. Jones, P. Braunlich, R. T. Casper, et al, "Recent progress on laser-induced modifications and intrinsic bulk damage of wide-gap optical-materials," Opt. Eng. **28**, 1039-1068 (1989).

22. C. B. Schaffer, "Interaction of femtosecond laser pulses with transparent materials," PhD thesis, Harvard University (2001).

23. P. Y. Yu, M. Cardona, *Fundamentals of Semiconductors*, Springer-Verlag: Heidelberg (1996).

24. E. G. Gamaly, A. V. Rode, B. Luther-Davies, et al, "Ablation of solids by femtosecond lasers: ablation mechanism and ablation thresholds for metals and dielectrics," Phys. of Plas. **9**, 949-957 (2002).

25. A. Tien, S. Backus, H. Kapteyn, et al, "Short-pulse laser damage in transparent materials as a function of pulse duration," Phys. Rev. Lett. **82**, 3883-3886 (1999).

26. P. P. Pronko, P. A. VanRompay, C. Horvath, et al, "Avalanche ionization and dielectric breakdown in silicon with ultrafast laser pulses," Phys. Rev. B **58**, 2387-2390 (1998).

27. B. Rethfeld, " Free-electron generation in laser-irradiated dielectrics," Phys. Rev. B **73**, 035101-1-6 (2006).

28. B. C. Stuart, M. D. Feit, S. Herman, et al, "Nanosecond-to-femtosecond laser-induced breakdown in dielectrics," Phys. Rev. B **53**, 1749-1761 (1996).

29. D. Du, X. Liu, G. Korn, et al, " Laser-induced breakdown by impact ionization in SiO_2 with pulse widths from 7 ns to 150 fs," Appl. Phys. Lett. **64**, 3071-3073 (1994). materials

30. E. N. Glezer, M. Milosavljevic, L. Huang, et al, "Three-dimensional optical storage inside transparent materials," Opt. Lett. **21**, 2023–2025 (1996).

31. V. P. Krainov, A. S. Roshchupkin, "Dynamics of the Coulomb explosion of large hydrogen iodide clusters irradiated by superintense ultrashort laser pulses," Phys. Rev. A. **64**, 063204~063208 (2001).

32. R. Stoian, A. Rosenfeld, D. Ashkenasi, et al, "Surface charging and impulsive ion ejection during ultrashort pulsed laser ablation," Phys. Rev. Lett. **88**, 097603~097606 (2002).

33. K. K. Thornber, "Application of scaling to problems in high-field electronic transport," J. Appl. Phys. **52**, 279-290 (1981).

34. S. Amoruso, X. Wang, C. Altucci, et al, "Thermal and nonthermal ion emission during high-fluence femtosecond laser ablation of metallic targets," Appl. Phys. Lett. **77**, 3728-3730 (2000).

35. J. Yang, Y. Zhao, X. Zhu, "Transition between nonthermal and thermal ablation of metallic targets under the strike of high-influence ultrashort laser pulses," Appl. Phys. Lett. **88**, 2006, 094101-1-3 (2006).

36. H. Dachraoui, W. Husinsky, "Thresholds of plasma formation in silicon identified by optimizing the ablation laser pulse form," Phys. Rev. Lett. **97**, 107601-1-4 (2006).

37. B. Rethfeld, A. Kaiser, M. Vicanek, et al, "Ultrafast dynamics of nonequilibrium electrons in metals under femtosecond laser irradiation," Phys. Rev. B **65**, 214303-1-10 (2002).

38. C. Cheng, X. Xu, "Molecular dynamic study of volumetric phase change induced by a femtosecond laser pulse," Appl. Phys. A **79**, 761-765 (2004).

39. L. V. Zhigilei, B. J. Garrison, "Microscopic mechanisms of laser ablation of organic solids in the thermal and stress confinement irradiation regimes," J. Appl. Phys. **88**, 1281-1298 (2000).

40. R. Kelly, A. Miotello, "Comments on explosive mechanisms of laser sputtering," Appl. Surf. Sci. **96-98**, 205-215 (1996).

41. Y. Li, C. R. Liao, D. N. Wang, et al, "Study of spectral and annealing properties of fiber Bragg gratings written in H_2-free and H_2-loaded fibers by use of femtosecond laser pulses," Opt. Express **16**, 21239-21247 (2008).

42. A. E. Siegman, *Lasers*, University Science Books: Sausalito CA (1986).

43. J. M. Liu, "Simple technique for measurement of pulsed Gaussian-beam spot sizes," Opt. Lett. **23**, 792-794 (1982).

Chapter 3 Fs Laser Micro-machining of Optical Fiber

Fs laser micro-machining of optical fiber includes many types, such as stationary irradiation for micro-hole drilling; line scanning or cleaving; circular irradiation; fusion splicing; inducing RI change or structure imprinting; and surface processing. In this chapter, two basic micro-machining types, the micro-hole drilling and the line scanning, will be applied to develop two novel micro-structure OFS: (a) a micro-hole and (b) a micro-cavity based MZI. The fabrication process and the fabrication parameters have significant effects on the morphology of the fabricated micro-structure. The applications of micro-hole as the temperature insensitive RI sensor and MZI as the high temperature sensor or RI sensor with extremely high sensitivity will be investigated.

3.1 Micro-hole Drilled in Single Mode Fiber (SMF)

The micro-machining system is introduced in section 2.2. The SMF under fabrication is mounted on a 3D translation stage by two clamps. The clamps can rotate with arbitrary angles, which is convenient for observing the morphology of the micro-structure in different views. The amplitude resolution of OSA is 0.01 dB. Referring to the axes in Fig. 2.5, the focus point is located at the fiber cladding surface in z-direction since material ablation occurs from the cladding surface into the fiber, while in x-y plane it is located at the fiber core center.

The fs laser pulse energy and the irradiation time decide the dimensions of the fabricated micro-hole. Normally, large pulse energy with a long irradiation time will result in a large diameter and depth of the micro-hole. Besides, according to

the discussion in section 2.3, the NA value of the focusing MO will also affect the micro-hole depth. For a proper selection of fabrication parameters, multiple tries need to be carried out in advance. For example, the side views of micro-holes drilled with different parameters are shown in Fig. 3.1 (a)-(d), with individual pulse energy and focusing MO parameters listed in Table 3.1. The depth and the diameter can be approximated from the microscope images.
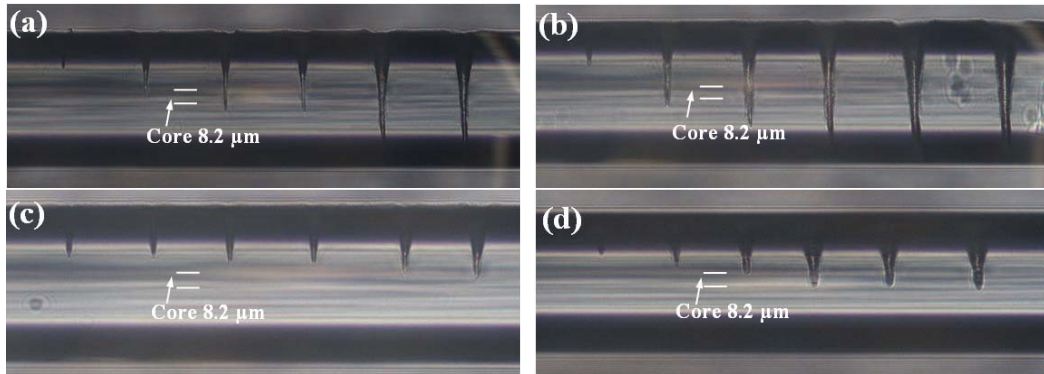
Fig. 3.1 Micro-holes fabricated with different fs laser irradiation parameters.

Table 3.1 Fabrication parameters of micro-holes in Fig. 3.1 (a)-(d).

Sample	MO parameters		Pulse energy (μJ)
	Magnification	NA	
Fig. 3.1 (a)	10×	0.25	5
Fig. 3.1 (b)	10×	0.25	10
Fig. 3.1 (b)	20×	0.50	5
Fig. 3.1 (d)	20×	0.50	10

The irradiation time for each micro-hole in Fig. 3.1 (a)-(d) is 5, 10, 20, 30, 60, 120 s, respectively, corresponding to the individual micro-hole appearing from left to right in each figure. It can be obviously seen from Fig. 3.1 (c) and Fig. 3.1 (d) that the micro-holes fabricated by the MO with the magnification of 20× can only penetrate to the core region (which is called half through) but can hardly penetrate fully through the whole fiber, no matter how long the irradiation time of fs laser is. However, by use of the MO with the magnification of 10×, the fs laser can fabricate either a half through or a full through micro-hole with proper pulse energy and irradiation time. This results from the fact that MO with a larger magnification usually has a smaller Rayleigh length, which limits the energy absorption depth and lowers the power density along z-direction, as

discussed in section 2.3.

From Fig. 3.1, another fact to be noticed is that the direct drilling by fs laser on fiber will result in a cone shape micro-hole and its cone angle depends on the beam diameter before entering the MO. A simple way for getting smaller cone angle is to adjust the spatial beam diameter and its wavefront by the small aperture in the external optical path stated in section 2.2. In this thesis, the fs laser spatial beam diameter is adjusted to about 5 mm. Besides, MO with a larger NA value will have a larger spread angle Θ according to Eq. (2.5), which also results in a larger cone angle, as shown in Fig. 3.1.

After a series of tries, it is found that when pulse energy is set as 11 μJ, either a full through or half through micro-holes with small cone angle can be easily fabricated by a 10× MO focused fs laser with different irradiation time. These two parameters are applied and kept constant for the rest of work in section 3.1. Compared with half through ones, when immersed into liquids, full through micro-holes can be fully filled of liquid quickly according to the well known capillary effect. The micro-holes before and after fully filled of liquid are shown in Fig. 3.2 (a) and (b) respectively, which is easily distinguished from each other.
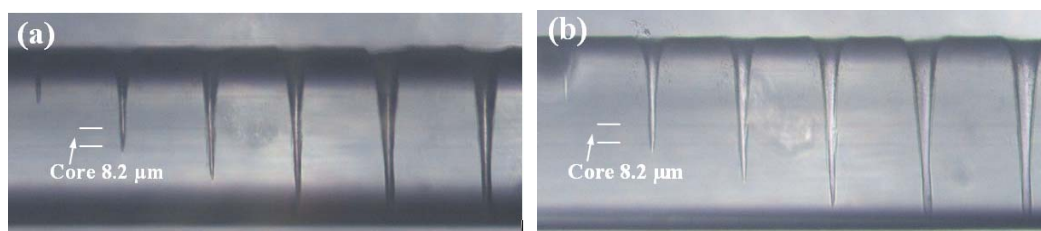
Fig. 3.2 Micro-holes (a) before (b) after fully filled with liquid.

The two main parameters to determine a micro-hole are its diameter D at the fiber core and the depth. In this section, three types of micro-holes are fabricated with different fs laser irradiation time of 5, 15, 150 s, respectively, with their individual D values approximated and listed in Table 3.2. The three D values are chosen for smaller than; close to; and larger than the fiber core diameter. Each

type of micro-holes has two samples for comparison. The morphologies of each

kind of micro-holes are shown in Fig. 3.3 (a)-(c), respectively.

Table 3.2 Three types of typical micro-holes.

Sample	Irradiation time (s)	D (μm)
S-6a	5	6.2
S-6b	5	6.1
S-8a	15	7.9
S-8b	15	8.0
S-11a	150	11.0
S-11b	150	11.0
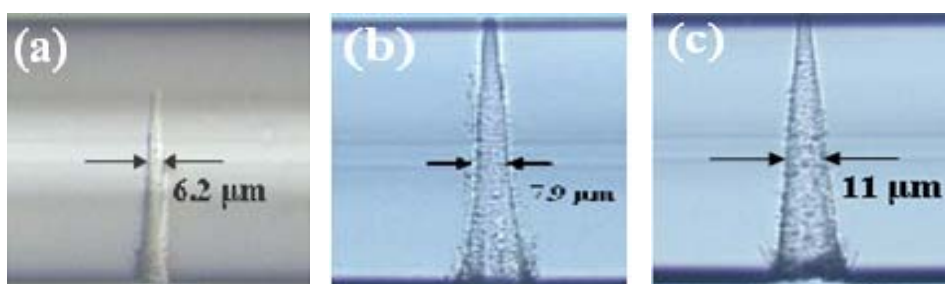
Fig. 3.3 Micro-holes with different D value (a) S-6 (b) S-8 (c) S-11.

3.2 Micro-hole Based Refractive Index (RI) Sensor

The RI responses of each type of micro-holes are carried out by the following

process (and for all RI sensing work in the rest of this thesis): (1) the

transmission spectrum of the sample in air is firstly recorded; (2) then the

sample is immersed in the RI liquid (from Cargille Laboratories) and the

corresponding transmission spectrum is measured; (3) the liquid filled is cleaned

by methanol solution and wait until the transmission spectrum of the sample

matches that in air. This process is repeated until all the RI liquids are measured.

3.2.1 RI Responses of Micro-holes with Different Sizes

The different RI responses of three samples, S-6a, S-8a, and S-11a, are shown in

Fig. 3.4, with wavelength dependence of the normalized transmission checked.
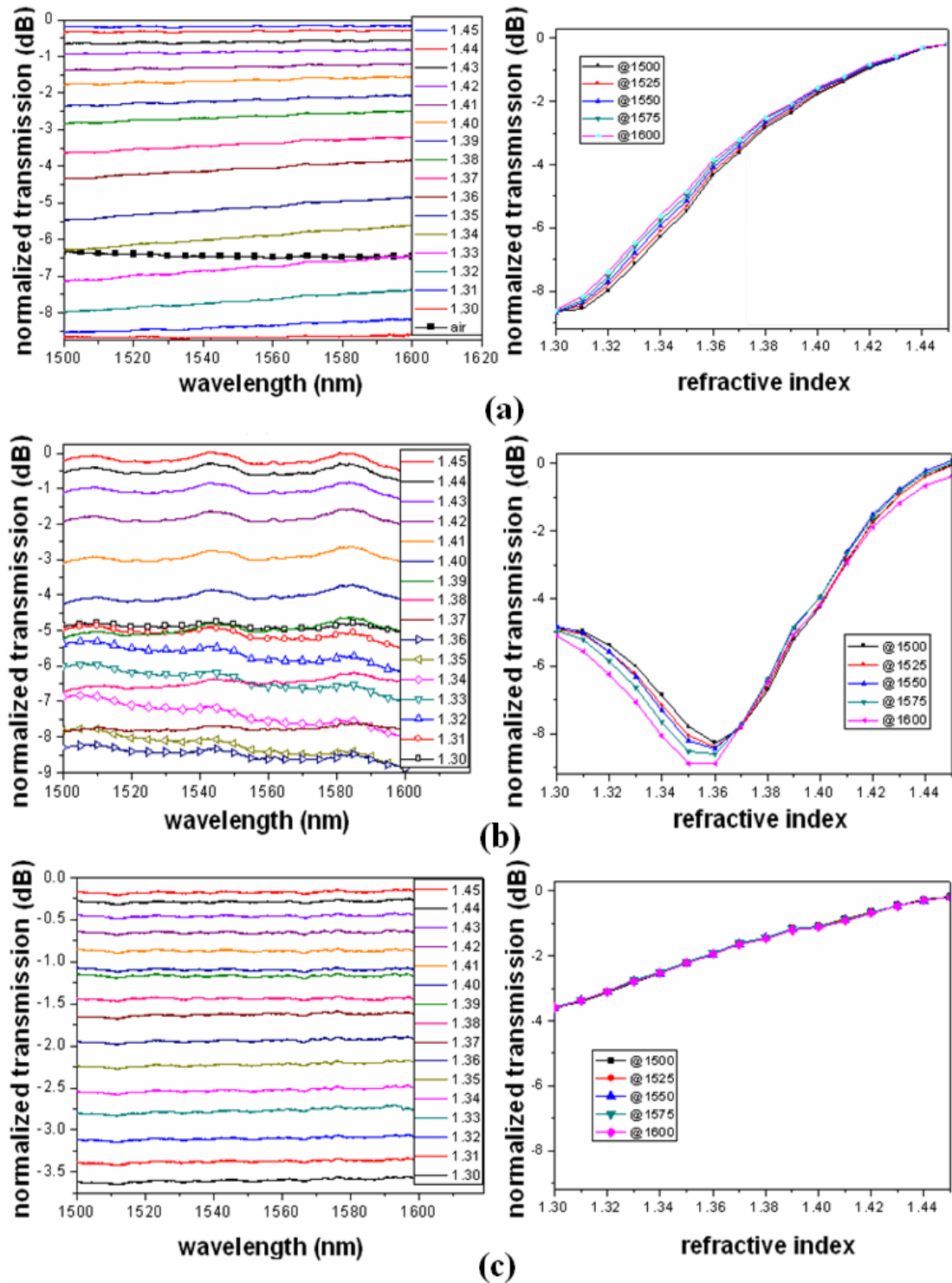
Fig. 3.4 RI responses of (a) S-6a (b) S-8a (c) S-11a.

Being different from the wavelength-coded OFS, the micro-hole based RI sensor here works by detecting the normalized transmission change, according to the RI of the liquid filled in it. The sensitivity of the device is measured with the unit of dB/RIU (refractive index unit). For S-6a, the transmission increases

monotonously with the liquid RI. The sample has a linear RI response in the region of 1.31-1.41, with an average sensitivity of 71 dB/RIU, which equals to the detection limit (DL) of 1.40×10^{-4} RIU. The DL here is defined as the minimum detection unit (0.01 dB of the OSA) divided by the sensitivity. The transmission has slight wavelength dependence in the region of 1500-1600 nm.

For S-8a, the transmission gradually and linearly decreases when the external RI changes from 1.30 to 1.35. The average sensitivity in this region is -67 dB/RIU. The transmission reaches minimum when liquid RI is 1.36 and then increases linearly in the region from 1.36-1.42, with an average sensitivity of 110 dB/RIU. Besides, this sample has a large wavelength dependence.

For S-11a, the transmission has a good linear response to the external RI in the region of 1.30-1.45. However, the average sensitivity is as small as 27 dB/RIU and the DL obtained is 3.70×10^{-4} RIU. Meanwhile, this sample has almost no wavelength dependence in the wavelength region of 1500-1600 nm.
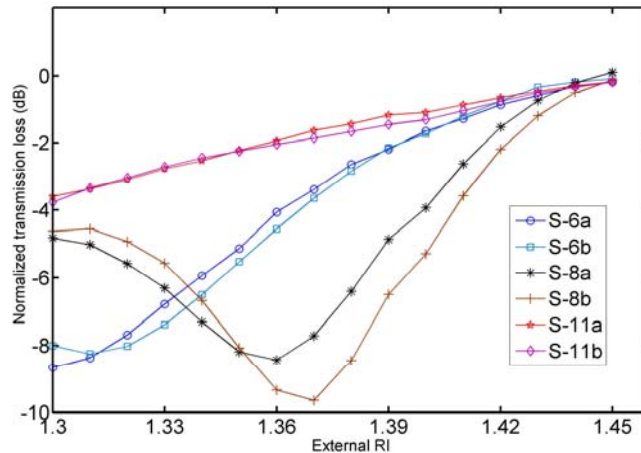
Fig. 3.5 RI responses of different samples at wavelength 1550 nm.

In order to verify the device reproducibility, the RI responses of S-6b, S-8b, and S-11b at the wavelength of 1550 nm are also investigated and shown in Fig. 3.5. For S-6b and S-11b, the RI response is quite similar to that of S-6a and S-11a. While for S-8b, the minimum transmission is obtained when the external RI

reaches 1.37. The results in Fig. 3.4 and Fig. 3.5 show that the RI response of the micro-hole strongly depends on its D parameter, especially when D is close to the fiber core diameter.

The light transmission behavior and the RI responses for micro-holes with different D parameters may be qualitatively explained by a simple ray optics model as shown in Fig. 3.6, where n_h and n_{core} ($n_h < n_{core}$) represents the RI of the liquid filled in the micro-hole and the RI of the fiber core.
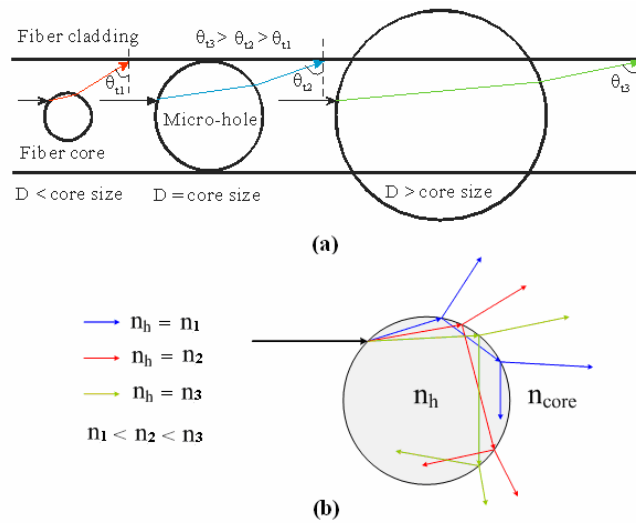
Fig. 3.6 Ray optics model for explaining the transmission behaviors of micro-holes with (a) different diameters (b) different RI values.

When $D<D_{core}$ (the core diameter), part of the light passes through the micro-hole and dissipates owing to the small incident angle θ_{t1} (which is smaller than the critical angle for total internal reflection) at the core–cladding interface. When $D>D_{core}$, the refracted light from the hole–core surface will be guided owing to the large incident angle θ_{t3} at the core-cladding interface. Such a difference in refracted light results in a larger transmission loss of $D<D_{core}$ than that of $D>D_{core}$, as the results shown in Fig. 3.4.

When $D≈D_{core}$, no light can be directly guided in the fiber core without passing through the micro-hole; thus the transmission is critically dependent on the RI of

the liquid filled in the micro-hole. Assuming that the light incident angle into the micro-hole is smaller than the critical angle, when $n_h=n_1$ is small, the first refracted beam cannot be bounded in the core, but the second refracted beam may be guided. When n_h is increased to a larger value of n_2, both the first and the second refracted beams can not be bounded by the core-cladding surface, which increases the transmission loss. When n_h is further increased to n_3, the first refracted beam will be directly guided, which should have a much higher intensity than the second refracted beam because of the low reflection at the air-core interface and thus reduce the transmission loss. Therefore, with the increase of the liquid RI in the micro-hole, the transmission will first decrease and then increase, and leaves a minimum transmission in the RI response curve.
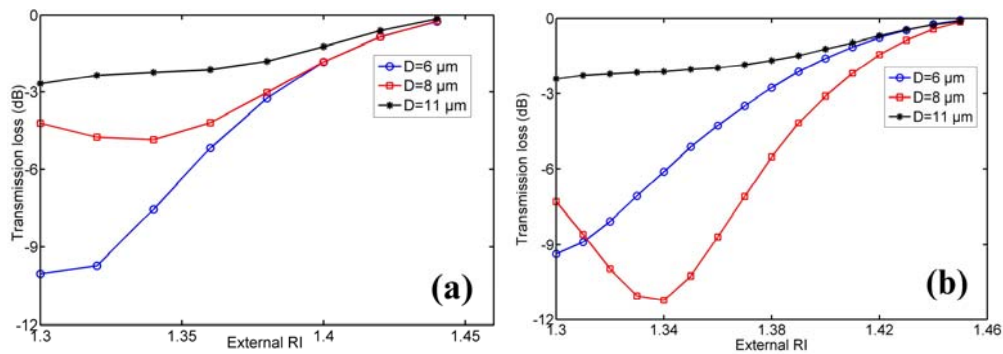
Fig. 3.7 Simulation of transmission loss of micro-holes with different D parameters at 1550 nm by (a) FDTD (b) BPM.

Two kinds of numerical methods are presented for quantitatively simulation the transmission property of micro-holes with different D parameters. The simulation results of finite-difference time domain (FDTD) and beam propagation method (BPM) are shown in Fig. 3.7 (a) and (b), respectively. Both the results show that the transmission property changes significantly when the micro-hole has a D parameter approximate to that of the fiber core diameter.

The slight wavelength dependence in Fig. 3.4 (a) and (b) may result from the fact that the micro-hole in the fiber core center can be considered as an FPI with a relatively small cavity length, which creates fringe spacing over a few hundreds

of nm [1-4]. The micro-hole can also lead to the scattering and multiple reflections of the propagation light, which plays a crucial role in the determination of the measurement resolution in different RI regions. Meanwhile, the roughness of the micro-hole wall created during the fs laser micro-machining process would cause fluctuation or ripple in the transmission spectra. This fluctuation could be reduced with optimized micro-machining parameters, such as using smaller pulse energy and longer irradiation time. The influence of the micro-hole depth on the transmission is not so significant as far as the micro-hole reaches the entire cross section of the fiber core. However, a small micro-hole depth can enhance the robustness of the device compared with the full through micro-hole [5, 6].

3.2.2 Temperature-RI Cross Sensitivity
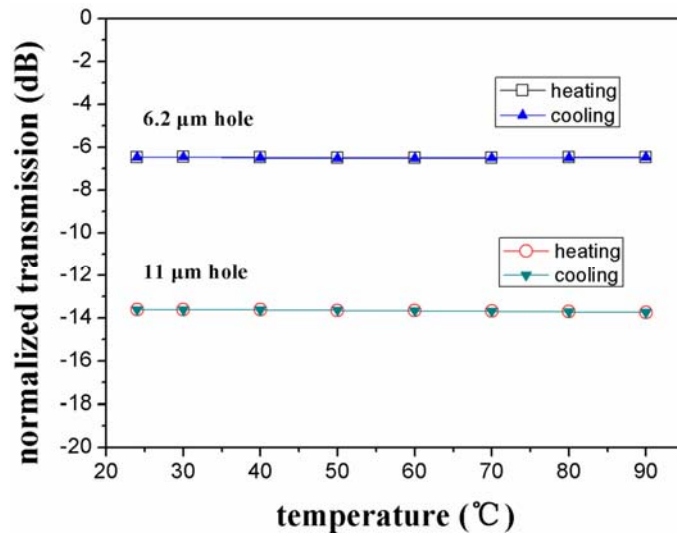
Fig. 3.8 Normalized transmissions of the micro-holes in air with the temperature.

In order to investigate the temperature response of this micro-hole based OFS device, the S-6a and the S-11a sample are firstly put in a column over (LCO102 made by ECOM Ltd.) and exposed to air. The heating and cooling tests are carried out and the transmission loss of each sample is shown in Fig. 3.8. For each temperature point, the samples are kept for more than 30 minutes until the temperature is stable. The transmission loss almost does not change (the

fluctuation is smaller than 0.01 dB), which shows that the micro-hole device has a temperature insensitive property.

For further investigation of the temperature insensitive property of the micro-hole, sample S-6a is immersed in water and heated by the same column oven as before. The RI of water will change according to its thermal coefficient, and thus change the transmission of the micro-hole at different temperature, which is shown as the black squares in Fig. 3.9. By subtracting the contribution from the temperature induced water RI change [7], the calibrated curve (red triangles in Fig. 3.9) exhibits only small fluctuations within 0.03 dB. The maximum measurement error induced by the temperature-RI cross sensitivity is less than 4.0×10^{-4} within the temperature range employed. This confirms the capability of the device to implement a temperature-independent RI measurement.
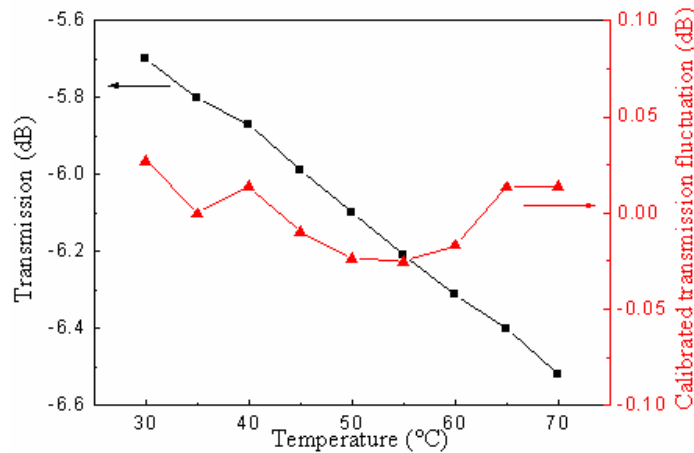
Fig. 3.9 Temperature response of sample S-6a when filled with water before calibration (black squares) and after calibration (red triangles).

3.3 Micro-cavity Based Fiber Mach-Zehnder Interferometer (MZI)

Fiber-inline MZI has wide applications in optical communication, optical switching and optical sensing. In many cases, fiber-line MZI is of great interests due to the advantages of structure compactness, fabrication simplicity and

easiness of signal detection [8-14]. Various types of fiber in-line MZI structures have been developed [8-14]. However, such MZI are based on the interference between the fundamental core mode and the higher order cladding mode, which has a very small effective RI difference between the two modes (<0.01). This results in a relatively large device size of typically in the order of from several mm to cm, which essentially limits their applications in some cases where RI variation needs to be precisely located.

Recently, a compact single-beam micro-fluidic MZI has been proposed of which the optical path difference (OPD) is achieved through light propagation across a fluid–air interface [15-17]. This type of MZI exhibits sufficient compactness, large tunability and an extreme high fringe visibility over 25 dB. However, the configuration contains three individual elements, with two sections of SMF functioning as light launching and output port, respectively, and one liquid filled capillary producing the OPD required, which needs additional precise alignment. Therefore, the integration of these individual elements would be advantageous.

3.3.1 Operation Principle

Line scanning is one typical application of fs laser micro-machining. By applying this technique, a number of micro-cavities and/or micro-holes have been fabricated as fiber-line FPI and applied for RI sensing [1-4]. In this section, a compact fiber-inline MZI structure is proposed based on the micro-cavity fabricated by fs laser line scanning along the fiber length. The schematic configuration is shown in Fig. 3.10.
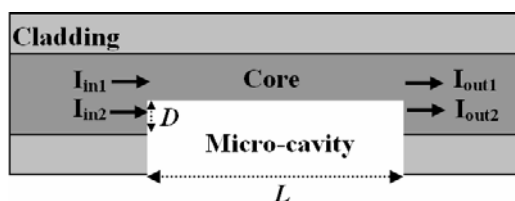
Fig. 3.10 Schematic configuration of the micro-cavity based fiber-inline MZI.

In Fig. 3.10, one of the interferometer arms contains a micro-cavity created by removing part of the fiber core near the core-cladding interface, and the other arm is the remaining part of the fiber core. The light propagating along the fiber will split into two portions (noted as I_{in1} and I_{in2}) by the first micro-cavity wall, and transmit in the two arms of MZI individually. Interference occurs when the two output light (noted as I_{out1} and I_{in2}) combine at the other micro-cavity wall. The micro-cavity has two important parameters: the cavity length L and the removed core width D.

According to the well-known two-beam interference equation [15]:

$$I_{out} = I_{out1} + I_{out2} + 2\sqrt{I_{out1}I_{out2}}\cos(\frac{2\pi\Delta nL}{\lambda}+\varphi_0) \tag{3.1}$$

where Δn is the difference of the beam effective RI of the two MZI arms and φ_0 is an initial random phase difference between the two arms. From Eq. (3.1), the interference signal reaches minimum when the following expression satisfied:

$$\frac{2\pi\Delta nL}{\lambda_m}+\varphi_0 = (2m+1)\pi \tag{3.2}$$

where m is an integer and λ_m is the wavelength of the m-th order of the transmission dip. And the FSR for certain fringe dip can be decided as:

$$FSR = \frac{\lambda_m^2}{\Delta nL} \tag{3.3}$$

From Eq. (3.3), it is clearly seen that the FSR is inversely proportional to the two arms $OPD = \Delta nL$. The micro-cavity based MZI approximately has the effective RI difference between the two arms with $\Delta n_{eff}{\approx}n_{silica}$-$n_{air}$=0.468, which is nearly 40 times larger than that of the conventional MZI based on core mode-cladding mode interference [8-14]. Therefore, for the certain FSR requirement, the cavity length can be reduced from the order of mm or cm to the order of several tens of μm, which enables the device a significantly compact dimension.

3.3.2 Device Fabrication

The fiber under ablation is mounted on the 3D translation stage as shown in Fig. 2.5. The fs laser is focused on the cladding surface, and then scanning along x-direction. According to the results in section 3.1, when focused by the 10× MO with pulse energy larger than 10 μJ, the fs laser can drill a full through micro-hole in SMF. For fabrication micro-cavity with a desired length, larger pulse energy and faster scanning speed of fs laser may save the micro-machining time. However, during the fs laser scanning process, micro cracks will be left in the ablation region, which makes the sample easily broken. Meanwhile, the scanning speed of the laser focus spot can not be too fast so as to make the cavity-core surface as smooth as possible, which can help to decrease the scattering loss of the device. After several tries, for a better micro-cavity quality, the fabrication parameters are set with the single pulse energy of 12 μJ and the scanning speed of 20 μm/s.

The fringe visibility depends on three factors: (1) the width of the removed fiber core D, which determines the relative intensity of I_{in1} and I_{in2}; (2) the transmission loss of the unguided mode in the micro-cavity; (3) the light absorption of the cavity medium. The latter two factors will affect the output power I_{out2} of the micro-cavity. The highest fringe visibility appears when $I_{out1}=I_{out2}$. For the proposed MZI with a large interference fringe visibility, it requires a proper adjustment of D value. Due to the different air-core interface dependent scattering loss, it is hardly to directly focus fs laser at the optimized D position. A possible solution is to first move the fs laser focus spot deviated away from the core center (in this section, the initial deviation distance is 20 μm in y-direction) and then slightly and gradually approaches the core center, until an acceptable visibility (for instance, over 15 dB) is obtained. At a certain deviation position, several times of scanning process along the fiber length are carried for a

polished micro-cavity surface. The morphology of the micro-cavity in different views is shown in Fig. 3.11.
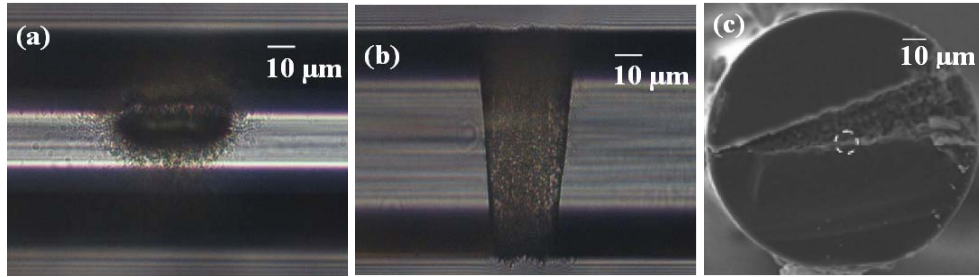
Fig. 3.11 Morphology of the micro-cavity in (a) top view (b) side view (c) cross section view.

The transmission spectra of several MZI samples with different micro-cavity lengths are shown in Fig. 3.12. Their individual FSR, scanning length of fs laser and calculated cavity length are listed in Table 3.3.
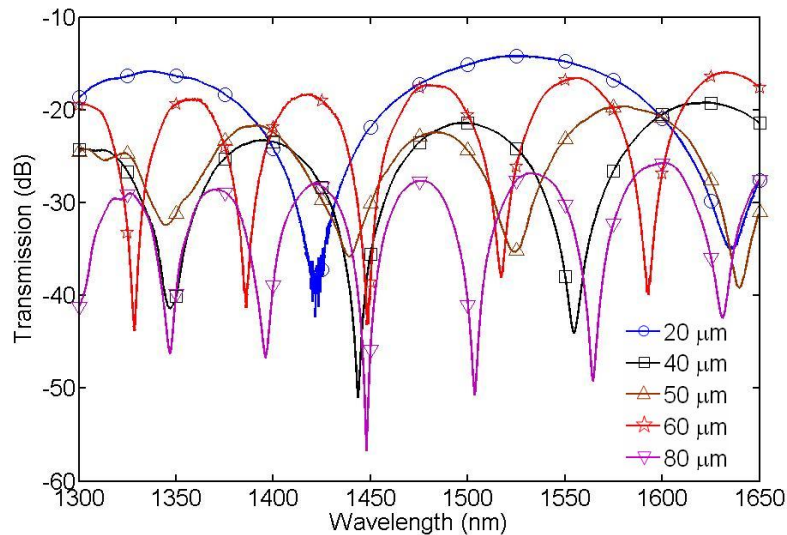
Fig. 3.12 Transmission spectra of several MZI samples with different fs laser scanning length.

Table 3.3 Individual scanning length, FSR and calculated cavity length of samples in Fig. 3.12.

Scanning length (μm)	FSR (nm)	Calculated cavity length (μm)
80	61	83
60	76	68
50	96	52
40	111	44
20	194	23

From Table 3.3, it can be seen that the actual micro-cavity length is always several μm larger than the fs laser scanning length along the fiber. This is due to

the fact that the focused laser beam has certain width at the beam waist as discussed in section 2.3. All the samples in Fig. 3.12 possess large device loss, which may result from: (1) the scattering loss at the cavity border, where the surface roughness is on the order of 1 μm; (2) the loss of the unguided mode propagated in the air cavity. By carefully controlling the pulse energy and scanning speed, the surface roughness and hence the insertion loss may be decreased, however, the unguided mode created loss might not be eliminated.

3.3.3 Application for High Temperature Sensing

One application of the MZI developed lies in the high temperature sensing, due to the permanent and stable structural change induced by the micro-cavity even in very high temperature region (>1000 ℃) as long as the fiber can survive below the silica transition temperature. The temperature sensitivity of the two-beam interference MZI can also be derived by differentiating of Eq. (3.2) with the micro-cavity length assumed constant:

$$\frac{\partial \lambda_m}{\partial T} = \frac{\lambda_m}{n_{eff}^{core}(T) - n_{eff}^{cavity}(T)} \left(\frac{\partial n_{eff}^{core}(T)}{\partial T} - \frac{\partial n_{eff}^{cavity}(T)}{\partial T} \right) \tag{3.4}$$

where $n_{eff}^{core}(T)$ and $n_{eff}^{cavity}(T)$ are the effective RI of the two arms of the MZI, which are both functions of temperature; $\frac{\partial n_{eff}^{core}(T)}{\partial T}$ and $\frac{\partial n_{eff}^{cavity}(T)}{\partial T}$ are their individual temperature coefficients. Further simplification can be applied by assume $n_{eff}^{cavity} = 1$ and keeps constant during the temperature variation. Therefore, the temperature sensitivity only depends on the monitored interference fringe dip wavelength and the temperature coefficient of the fiber core mode.

In order to check the high temperature sensing performance, a sample with micro-cavity length of 47 μm is put into a high temperature tube furnace (type MTF 12/38/250, made by CARBOLITE Ltd.) for high temperature measurement. The instrument can display the temperature directly at its tube center. The sample

is tried to be put at the middle of the tube furnace so as to make its environment temperature close to the value displayed by the instrument. The interference dip around 1551 nm at room temperature is monitored during the experiment since it has the largest FSR in the wavelength region of 1500–1600 nm. The sample is first heated to 1000 ℃ and maintained there for 2 hours to remove the effects of stress change induced by fiber coating burning, dopant diffusion and residual stress relaxation. After the device is cooled down slowly to the room temperature, the interference dip is found to shift to shorter wavelength for about 3 nm compared with the original spectrum. No significant deterioration of the transmission spectrum appears after the annealing process.

Then the sample is gradually heated to 100 ℃, and subsequently from 100 ℃ to 1100 ℃ with a step of 100 ℃, and stayed for 30 min at each step. The sample is kept at 1100 ℃ for 2 hours to investigate its high temperature stability before being cooled down to 100 ℃ and then to the room temperature, following the same step and staying time as in the heating process. The dip wavelength and the transmission spectra are recorded in both the heating and cooling processes. There is only a slight deviation (<0.2 nm) of the dip wavelength in the cooling process compared with that in the heating process. The thermal test is repeated for several times and the results have good repeatability.

Fig. 3.13 (a) shows the transmission spectra at different temperature points. The dip shifts toward longer wavelength with the increase of temperature. Fig. 3.13 (b) presents the variation of dip wavelength with the temperature change, the results obtained show good repeatability during the heating and cooling process with an obtained temperature sensitivity of 0.046 nm/℃. According to Eq. (3.4), the theoretical temperature sensitivity is calculated as 0.045 nm/℃, by applying the values as $n_{eff}^{core}(T) = 1.4682$ and $\dfrac{dn_{eff}^{core}(T)}{dT} = 1.3 \times 10^{-6}$ [18], which is in good

agreement with the experiment result. With the OSA resolution set of 0.01 nm, the DL obtained is 0.22 ℃.
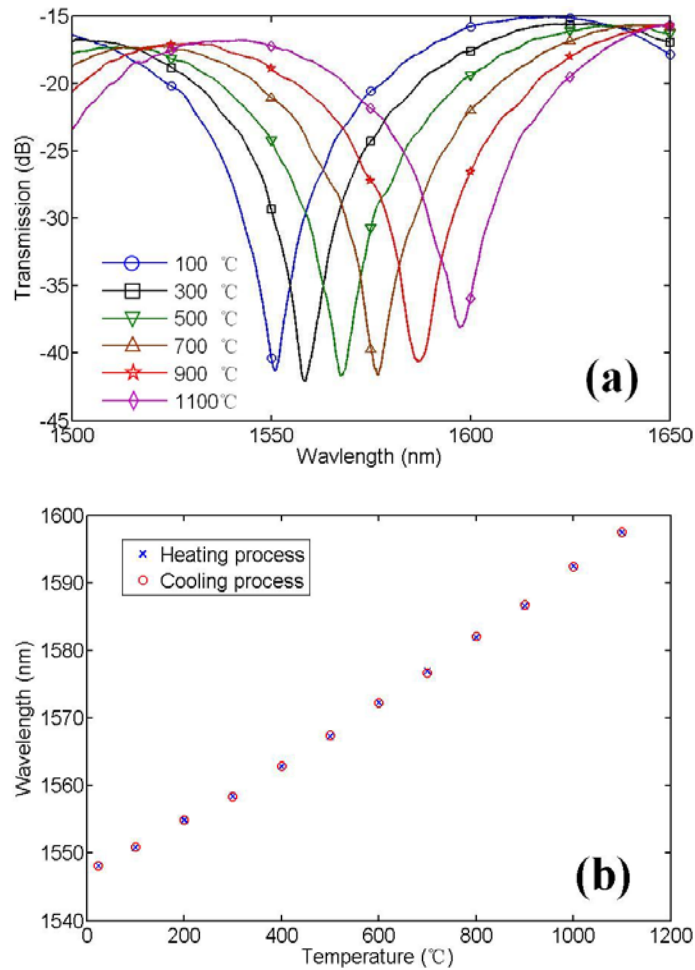
Fig. 3.13 Temperature sensitivity of the sample with 47 μm cavity length (a) transmission spectra at different temperatures (b) wavelength shift versus temperature.

3.3.4 Application for RI Sensing

The micro-cavity exposes the remaining core to external environment, which also enables this device for RI sensing. However, it should be noticed that the large fringe visibility in air (n_{cavity}=1) will degrade significantly when it is immersed in RI liquids, due to the large reduction of the effective RI difference between the core and the micro-cavity, which changes the light splitting ratio and causes the decrease of unguided mode loss and scattering loss. Assuming that the optimal visibility for MZI is initially achieved in air, when it is immersed in RI

liquid, the D value should be reduced (so as to increase I_{in1} in the remaining core) to maintain optimal visibility. On the other hand, optimal visibility achieved for the MZI in RI liquids cannot be maintained for the device in air.
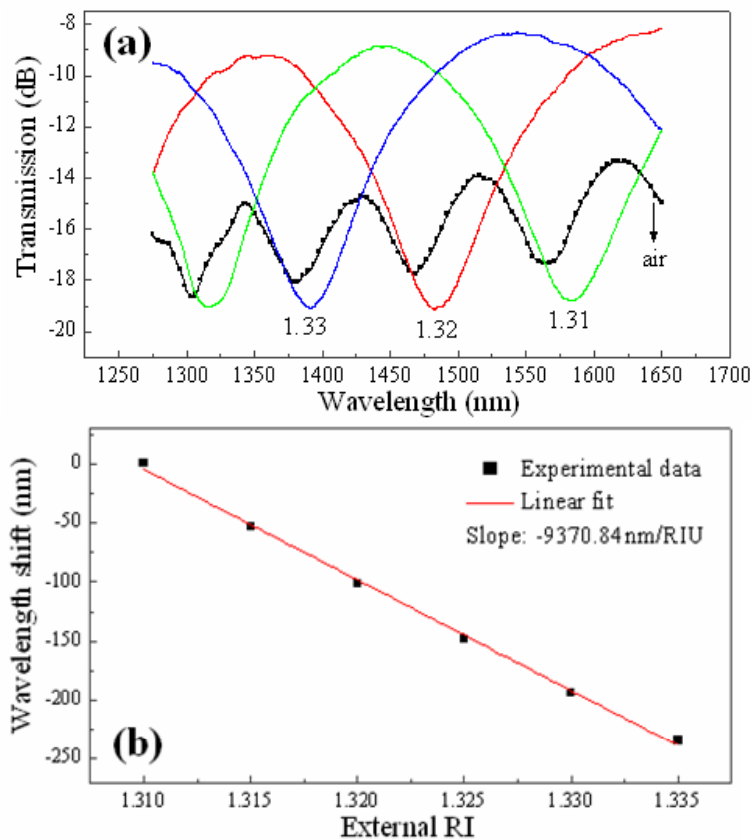
Fig. 3.14 Interference spectra of the fiber in-line MZI (a) transmission spectra in different RI liquids (b) wavelength shift versus the liquid RI filled in the micro-cavity.

In order to get a large visibility in RI liquids, a 51 μm micro-cavity MZI with fringe visibility of 4 dB and insertion loss of 14 dB in air is fabricated and immersed in RI liquids in the region of 1.305-1.340, with an interval 0.005. The transmission spectra recorded have an OSA resolution of 0.1 nm. The sample in RI liquids shows a larger visibility (~9 dB) than that in air. Selected transmission spectra of the sample corresponding to the liquid RI values of 1.31, 1.32, and 1.33 are plotted in Fig. 3.14 (a). The wavelength shift corresponding to different RI values between 1.31 and 1.335 is shown in Fig. 3.14 (b), where a linear fit of the experimental data is implemented and an extremely high sensitivity of −9370.84 nm/RIU is obtained.
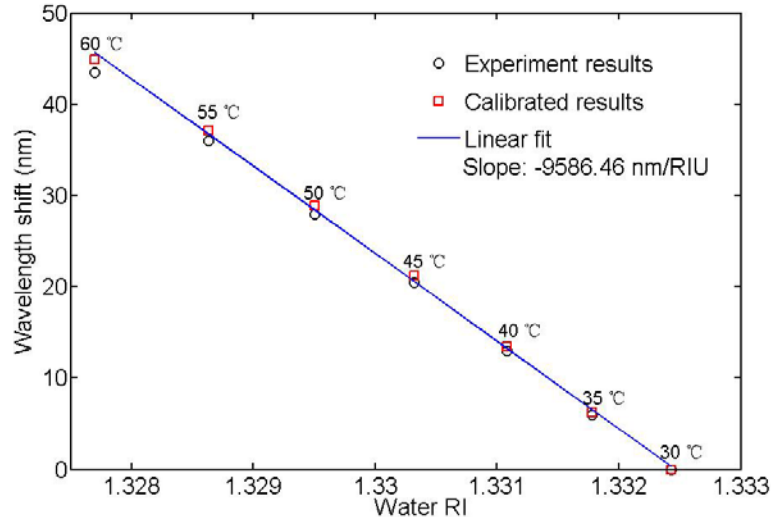
Fig. 3.15 Wavelength shift of the fiber in-line MZI with water filled in the micro-cavity. Black circles: monitored wavelength shift; red squares: calibrated wavelength shift by subtracting the temperature induced wavelength shift; line: linear fitting.

The linear response of the fiber in-line MZI to the external RI in a finer scale is also investigated by filling the cavity with water and varying the temperature. The temperature RI coefficient of the water is in the order of $10^{-4}/℃$ [7], much larger than that of fused silica (typically in the order of $10^{-5}/℃$) [18]. Fig. 3.15 demonstrates the wavelength shift of the device in the RI region between 1.32770 and 1.33243, corresponding to the temperature variation from 60 to 30 ℃ [18]. A total wavelength shift of ~43 nm can be observed. By subtracting the wavelength shift induced by temperature change according to the temperature sensitivity obtained in section 3.3.2, the RI sensitivity obtained is − 9586.46 nm/RIU, which is in good agreement with the results obtained previously.

The cavity length is supposed to keep constant during the RI sensing experiment. The RI sensitivity $\dfrac{\partial \lambda}{\partial n}$ can therefore be derived by differentiating Eq. (3.2) as:

$$\frac{\partial \lambda}{\partial n} = \frac{\lambda}{\Delta n} \qquad (3.5)$$

According to Eq. (3.5), the sensitivity of the MZI developed in this section can be calculated as -9924.1 nm/RIU at 1570 nm for $\Delta n=1.4682−1.31=0.1582$, which is close to the experimental results obtained.

The DL for wavelength encoded OFS can be determined with the smallest detectable change in resonance wavelength (R) and the sensitivity (S) by DL=R/S [19]. The R value can be estimated by taking into account the signal-to-noise ratio (SNR), full width at half maximum (FWHM) value of the resonance, thermal noise, and the OSA resolution. For the MZI developed in this section, R is dominated by the FWHM value of the interference fringe dip, which is measured to be ~80 nm. Assuming the SNR is 50 dB, DL is calculated to be 3.0×10^{-4} RIU [19]. DL could be further refined by optimizing the interference fringe visibility of the MZI device.

3.4 Summary

In this chapter, the fabrication processes for direct drilling of a micro-hole and a micro-cavity into SMF are presented as two typical applications of fs laser micro-machining on optical fiber. The fabrication parameters, including the magnification of focusing MO, the laser pulse energy, the irradiation time or scanning speed, are discussed in detail, which is well adjusted according to the desired morphology and the quality of the fabricated micro-structures.

The RI responses of three typical micro-holes, with different diameters near the fiber core are investigated. For micro-hole diameter smaller or larger than the fiber core diameter, the RI responses are monotonously increasing with the external RI. While for diameter close to the fiber core, a minimum transmission exists in the RI response curve. Simple ray optics model and numerical simulations are employed to explain the different transmission properties both qualitatively and quantitatively. The temperature-RI cross sensitivity of sample S-6a is examined to be small by immersing in water and heating together, which enables the micro-hole device as a temperature independent RI sensor.

A fiber-inline MZI is proposed by removing part of the fiber core and leaving micro-cavity deviated at several μm away from the core center. The light can then be split into two parts by the micro-cavity and the remaining core and then interfere at the micro-cavity end. The micro-cavity length determines the FSR of the interference fringe. The fringe visibility is mainly determined by the removed fiber core width, which can be optimized to over 15 dB by making fs laser focus point gradually approach the core center and repeat scanning process at each deviation position. Due to the permanent structural change, this kind of device can be applied for high temperature (up to 1100 ℃) sensing, with a good repeatability. The device can also be applied for RI sensing with an extreme high sensitivity of -9370.84 nm/RIU obtained in the RI region around water. Both the temperature and the RI sensitivity can be simulated by two-beam interference model, with the simulation results close to that of the experiments.

The micro-structures developed in this chapter possess extremely compact device dimensions and large RI sensitivities compared with normal OFS. The device performance can be further improved by carefully controlling the fs laser processing parameters, which may reduce the surface roughness of the micro-structures and thus reduce the scattering loss.

References for Chapter 3

1. Y. Rao, M. Deng, D. Duan, et al, "Micro Fabry-Perot interferometers in silica fibers machinded by femtosecond laser," Opt. Express **15**, 14123-14128 (2007).

2. Z. L. Ran, Y. J. Rao, W. J. Liu, et al, "Laser-micromachined Fabry-Perot optical fiber tip sensor for high-resolution temperature-independent measurement of refractive index," Opt. Express **16**, 2252-2263 (2008).

3. T. Wei, Y. Han, H. Tsai, et al, "Miniaturized fiber inline Fabry-Perot interferometer fabricated with a femtosecond laser," Opt. Lett. **33**, 536-538

(2008).

4. T. Wei, Y. Han, Y. Li, et al, "Temperature-insensitive miniaturized fiber inline Fabry-Perot interferometer for highly sensitive refractive index measurement," Opt. Express **16**, 5764-5769 (2008).

5. Y. Lai, K. Zhou, I. Bennion, "Microchannels in conventional single-mode fibers," Opt. Lett. **31**, 2559-2561 (2006).

6. K. Zhou, Y. Lai, X. Chen, et al, "A refractometer based on a micro-slot in a fiber Bragg grating formed by chemically assisted femtosecond laser processing," Opt. Express **15**, 15848-15853 (2007).

7. P. Schiebener, J. Straub, J. M. H. Levelt Sengers, et al, "Refractive index of water and steam as function of wavelength, temperature and density," J. Phys. Chem. Ref. Data **19**, 677-717 (1990).

8. V. P. Minkovich, J. Villatoro, D. Monzón-Hernández, et al, "Holey fiber tapers with resonance transmission for high-resolution refractive index sensing," Opt. Express **13**, 7609–7614 (2005).

9. B. H. Lee, J. Nishii, "Dependence of fringe spacing on the grating separation in a long-period fiber grating pair," Appl. Opt. **38**, 3450–3459 (1999).

10. J. H. Lim, H. S. Jang, K. S. Lee, et al, "Mach–Zehnder interferometer formed in a photonic crystal fiber based on a pair of long-period fiber gratings," Opt. Lett. **29**, 346–348 (2004).

11. H. Y. Choi, M. J. Kim, B. H. Lee, "All-fiber Mach–Zehnder type interferometers formed in photonic crystal fiber," Opt. Express **15**, 5711–5720 (2007).

12. J. Villatoro, V. P. Minkovich, D. Monzón-Hernández, "Compact modal interferometer built with tapered microstructured optical fiber," IEEE Photon. Technol. Lett. **18**, 1258–1260 (2006).

13. Z. Tian, S. S.-H. Yam, J. Barnes, et al, "Refractive index sensing with Mach–Zehnder interferometer based on concatenating two single-mode fiber tapers," IEEE Photon. Technol. Lett. **20**, 626–628 (2008).

14. P. Lu, L. Men, K. Sooley, and Q. Chen, "Tapered fiber Mach–Zehnder

interferometer for simultaneous measurement of refractive index and temperature," Appl. Phys. Lett. **94**, 131110 (2009).

15. C. Grillet, P. Domachuk, V. Ta'eed, et al, "Compact tunable microfluidic interferometer," Opt. Express **12**, 5440–5447 (2004).

16. P. Domachuk, C. Grillet, V. Ta'eed, et al, "Microfluidic interferometer," Appl. Phys. Lett. **86**, 024103 (2005).

17. C. Monat, P. Domachuk, C. Grillet, et al, "Optofluidics: a novel generation of reconfigurable and adaptive compact architectures," Microfluid. Nanofluid. **4**, 81–95 (2008).

18. T. Toyoda, M. Yabe, "The temperature dependence of the refractive indexes of fused silica and crystal quartz," J. Phys. D, Appl. Phys. **16**, L97–L100 (1983).

19. I. M. White, X. D. Fan, "On the performance quantification of resonant refractive index sensors," Opt. Express **16**, 1020–1028 (2008).

Chapter 4 Micro-holes Based Long Period Fiber Grating (LPFG)

LPFG possesses a periodical RI modulation along the fiber length, which couples the light energy from the core mode to the co-directional cladding mode and hence creating resonant dips in its transmission spectrum [1]. Various types of inscription methods, such as UV laser exposure [1-6], CO_2 laser irradiation [7-11], electric arc discharge [12-15], fs laser irradiation [16-20], mechanical micro-bending [21-23], chemical etched corrugations [24, 25] and ion beam implantation [26, 27] have already been developed to fabricate LPFG in different kinds of fibers, including SMF, PCF, fiber tapers, hollow core and all solid PBGF. Various LPFG based OFD have already been developed for sensing and telecommunication applications [28-30]. Normally, these LPFG can be regarded as index modulation type, whereas no significant structure modification lies in the fiber waveguide. Thus, the index modulation may not be strong enough and it requires a large grating length (in the order of several cm) to form a sufficient energy coupling between the core mode and the cladding mode.

Based on the micro-hole developed in Chapter 3, it is possible to make strong structural modulated LPFG by periodically drilling multiple micro-holes along the fiber length. However, the normally employed coupled mode theory (CMT) [31], which fits well for uniform grating (or grating with weak waveguide perturbation) such as LPFG inscribed by UV laser, can not be completely applied for the strong structural change. In this chapter, the coupled local mode theory (CLM) [32] is introduced to explain the coupling mechanism of such type of strongly waveguide modulated LPFG. The effects of RI modulation symmetry on the mode field distribution, the transmission spectrum and the polarization dependent loss (PDL) will also be investigated. LPFG based on periodically

micro-holes are fabricated in all-solid PBGF and SMF by use of fs laser micro-machining. Being different from the index modulation type LPFG also fabricated by use of fs laser [16–20], the micro-hole structured LPFG introduces a strong and asymmetric structural modulation in the fiber core and cladding, which couples light from the core mode to the cladding mode in a relatively efficient way by supporting a small grating dimension. The modes involved in the coupling and the corresponding phase matching curves are also examined and the experimental results obtained are compared with numerical simulations. RI sensing by use of the LPFG developed has also been carried out.

4.1   General Discussion of LPFG

4.1.1 Coupled Local Mode Theory

According to the CLM, the transverse electric and magnetic fields in the fiber with waveguide perturbation can be expressed as a superposition of individual local-modes with radiation fields as [32]:

$$E_t(x,y,z) = \sum_j E_{t,j}(x,y,z) = \sum_j \{b_j(z) + b_{-j}(z)\}\hat{e}_{t,j}(x,y,z) \qquad (4.1)$$

$$H_t(x,y,z) = \sum_j H_{t,j}(x,y,z) = \sum_j \{b_j(z) - b_{-j}(z)\}\hat{h}_{t,j}(x,y,z) \qquad (4.2)$$

where $b_j(z)$ represents the electric or magnetic field of a local mode, which contains both the amplitude and the phase information as [33]:

$$b_j(z) = a_j(z)\exp\{i\int_0^z \beta_j(z)dz\} \qquad (4.3)$$

in which $\beta_j(z) = \dfrac{2\pi}{\lambda}n_{eff}^j$ is the propagation constant, $\hat{e}_{t,j}$ and $\hat{h}_{t,j}$ are the normalized transverse mode electric and magnetic field profiles. The negative subscript $-j$ represents the backward propagation mode. Individual local mode may not be an exact solution of the Maxwell's equations, but they still satisfy the modes orthogonality in set. Considering the modes coupling between the core mode and the cladding mode, the general description of coupled local mode equations are:

$$\frac{db_{co}(z)}{dz} - i\beta_{co}(z)b_{co}(z) = C(z)b_{cl}(z)$$

$$\frac{db_{cl}(z)}{dz} - i\beta_{cl}(z)b_{cl}(z) = -C(z)b_{co}(z) \qquad (4.4)$$

where $C(z)$ is the mode coupling coefficient between the two modes:

$$C(z) = \frac{1}{4} \int_{A\infty} \{\hat{h}_{t,j} \times \frac{\partial \hat{e}_{t,l}}{\partial z} - \hat{e}_{t,j} \times \frac{\partial \hat{h}_{t,l}}{\partial z}\} \cdot \hat{z} dA \qquad j \neq l \qquad (4.5)$$

The CMT theory bases on the assumption that the core mode is partially coupled to individual cladding mode when passes through each waveguide perturbation and the intermodal coupling efficiency between the core mode and each cladding mode can be quantified by calculating the coupling coefficient between them. While in the unperturbed waveguide region, no mode coupling occurs.

If the fiber possesses a periodical waveguide perturbation with a period of Λ along the fiber length, $C(z), \beta_{co}(z)$ and $\beta_{cl}(z)$ are then a periodical function of z, and can be expanded into Fourier series [33]:

$$C(z) = \sum_{N=0}^{\infty} f_N \exp(i\frac{2N\pi}{\Lambda}z) \qquad (4.6)$$

where N denotes the grating order, f_N is the amplitude of the N-th harmonic component. By substituting Eq. (4.3) and Eq. (4.6) into Eq. (4.4), the corresponding phase term on the right hand is then:

$$\Delta\varphi = \int_0^z [\beta_{cl}(z) - \beta_{co}(z) + \frac{2N\pi}{\Lambda}]dz \qquad (4.7)$$

The resonant coupling occurs when the phase matching condition is satisfied, which requires that $\Delta\varphi \equiv \varphi(z_0 + \Lambda) - \varphi(z_0) = 0$ with a random starting point z_0.

Therefore, the resonant wavelength λ_{res} can be determined as:

$$N\lambda_{res} = \int_{z_0}^{z_0+\Lambda} [n_{eff}^{co}(z) - n_{eff}^{cl}(z)]dz \qquad (4.8)$$

If $n_{eff}^{co}(z)$ and $n_{eff}^{cl}(z)$ can be considered uniform (or constant) in the grating period, then Eq. (4.8) can be simplified as $N\lambda_{res} = (n_{eff}^{co} - n_{eff}^{cl})\Lambda$, which is the well-known phase matching condition of conventional CMT for weak perturbation LPFG.

The transmission spectrum of an ideal LPFG (with an infinite period number) would have a resonant dip (with no bandwidth) in the transmission spectrum at the resonant wavelength according to Eq. (4.8). For actual LPFG, the grating period number is limited, which means $C(z)$ is not an ideal periodical function of z as expressed in Eq. (4.6). The phase matching condition Eq. (4.8) still holds but the resonant dip will broaden and the resonant depth will reduce with the decrease of the number of grating periods.

Although an analytical solution of Eq. (4.4) can be hardly obtained, due to the rather complex dependence of $C(z)$, $\beta_{co}(z)$ and $\beta_{cl}(z)$ on z, a numerical simulation as an alternation can be carried out, which includes the following process [33]: (1) the waveguide variation geometry model is separated into several thin sections with thickness of Δz, and the parameters $C(z)$, $\beta_{co}(z)$ and $\beta_{cl}(z)$ are considered uniform in each section; (2) for a certain wavelength, the mode field profiles and the propagation constants of the core mode and the cladding mode can be decided through an finite element method (FEM), and $C(z)$ can be calculated by Eq. (4.5); (3) the initial input light is the core mode, which equals to the input boundary condition as $a_{co}(0) = 1$ and $a_{cl}(0) = 0$, and the individual transmitted amplitudes $a_{co}(\Delta z)$ and $a_{cl}(\Delta z)$ of the two modes in the small section can be calculated through Eq. (4.4) and are set as the input boundary condition for the next section. By repeating these procedures over the investigated waveguide variation and wavelength region, the final transmission spectrum can be obtained.

4.1.2 Symmetry of RI Modulation

The RI modulation symmetry may have significant effect on modes coupling. For LPFG written in SMF by UV exposure [1] or in boron-doped fiber by small CO_2 laser irradiation dosage [34], the RI modulation mainly locates in the fiber core region, which is rather small compared with the entire fiber cross section. Therefore, the RI modulation can be considered symmetric and the coupling occurs from the core mode (LP_{01} mode) to the circularly symmetric cladding mode (LP_{0x} mode). However, in the majority situations, due to the single side laser irradiation, a large asymmetric RI modulation lies in the fiber cross section, which excites a circularly asymmetric cladding mode (LP_{1x} mode) [35-37] and thus forms the mode coupling between the core mode and these asymmetric cladding modes. The cladding mode field profile is strongly dependent on the magnitude and the distribution profile of the RI modulation [35].
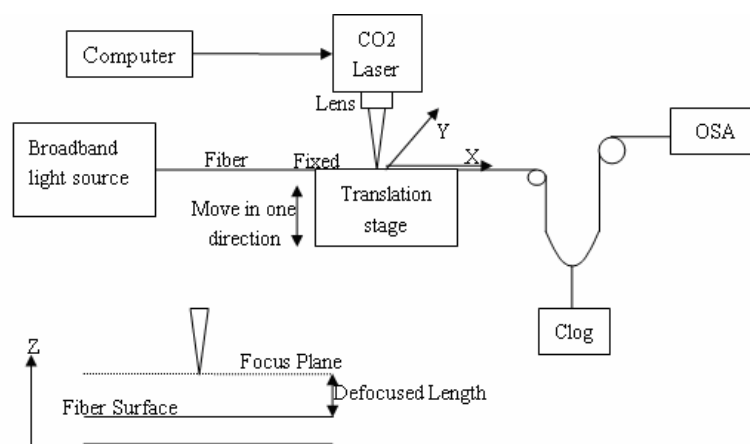
Fig. 4.1 Fabrication system of LPFG with defocused high-frequency CO_2 laser.

In order to investigate the RI modulation asymmetry property, several LPFG samples are written by CO_2 laser irradiation with different defocused length (defined as the distance between fiber cladding surface and focus plane). The fabrication setup is shown in Fig. 4.1. A high frequency CO_2 laser system with wavelength of 10.6 μm, repetition rate of 10 kHz, and average output power of ~0.5 W is used (Hans Laser). The SMF under irradiation is accurately positioned

using a translation stage that can adjust the defocused length. The fiber is pulled straight during the fabrication by a small weight clog (~5 g). The laser pulses first scan perpendicularly along the fiber (y-direction) and then shift a grating period along the fiber length (x-direction) before the next scan starts. The process continues until the whole grating length is reached, which forms a complete cycle. Usually several cycles are needed to write an LPFG with large resonant dip depth. The same laser output power is employed for different scanning cycles by keeping the control parameters unchanged.
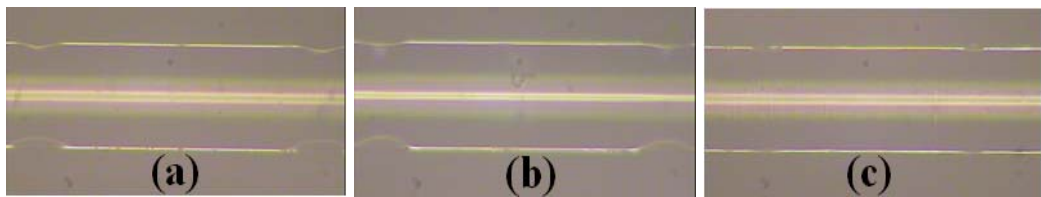
Fig. 4.2 Cladding surface of LPFG with different defocused lengths (a) 0 mm (b) 1 mm (c) 2 mm.

Three samples with different defocused length of 0, 1, and 2 mm, are made and their surface morphologies are shown in Fig. 4.2 (a)-(c), respectively. Each of the three samples has a grating pitch of 400 μm and a grating number of 40. The CO_2 laser has a focused beam spot diameter of ~35 μm [38], which means that the laser beam irradiation cannot reach the whole fiber surface when it is accurately focused. When the defocused length is small, the laser can carve minor periodical grooves on the cladding due to the high local temperatures created [38], as shown in Fig. 4.2 (a) and 4.2 (b).

The near-field mode profiles at the resonant wavelengths of the three samples have been examined by a system including a tunable laser (Agilent 8164B), a lens, an infrared camera (Electrophysics 7290A), and a data collecting computer. The output power of the tunable laser is kept constant during the whole experiment. The tested LPFG is perpendicularly cleaved at one end of the grating length in order to observe the near-field profile. The brightness of the mode field profile is proportional to the mode energy intensity, which is related to the

amplitude of RI change. The near-field mode profile of each sample at its corresponding resonant wavelength is shown in Fig. 4.3. It can be observed that, when the focus plane is accurately located on the cladding surface, the excited cladding mode field has a strong angle-dependent profile, as shown in Fig. 4.3 (a). The mode field profile intensity also implies that the RI change is mainly concentrated in the laser irradiation direction. The cladding mode field profile is mainly a circularly asymmetric LP_{16} mode superimposed with other cladding modes, which is determined by the mode field profile and the phase matching condition simulated. With the increase of defocused length, the cladding mode changes from a single-side hybrid mode like profile to a standard LP_{16} mode like profile. Meanwhile, the mode field intensity implies that more power is confined to the area near the core as the defocused length increases, as shown in Fig. 4.3 (b) and 4.3 (c).
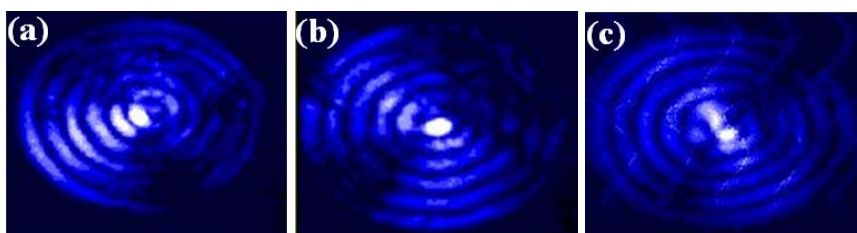
Fig. 4.3 Excited LP_{16} mode of LPFG with defocused lengths (a) 0 mm (b) 1 mm (c) 2 mm.

The periodic residual stress relaxation is considered the main mechanism to form the LPFG [39, 40]. When the focus plane is moved away from the cladding surface, both the laser transmission loss in the air and the enlargement of the affected area will lower the power intensity irradiated on the cladding surface. This in turn reduces the laser penetration depth into the fiber, thus decreases the heat depth of the silica glass [41]. This implies that the residual stress relaxation mainly occurs near the cladding surface region in the laser irradiation direction, while the fiber core is hardly affected. For the normal penetration depth, the RI decreases linearly from the cladding surface to the core. However, when the penetration depth is small, the RI change may follow an approximately quadratic or exponential profile [35]. Based on this assumption, the LP_{16} cladding mode

fields in a normal SMF with different side RI change profiles are simulated. The expression for each of the profiles is: (a) $n = n_0 - y\Delta n_1$; (b) $n = n_0 - y^2 \Delta n_2$ and (c) $n = n_0 - (e^{y/R} - 1)\Delta n_3$, where n_0 is the initial cladding RI; y is the axis parallel with laser irradiation direction, with the origin located at the core center; R is the cladding radius; and Δn_i represents the coefficient that ensures all three profiles have the same largest RI change magnitude of 3×10^{-4} at the cladding surface.
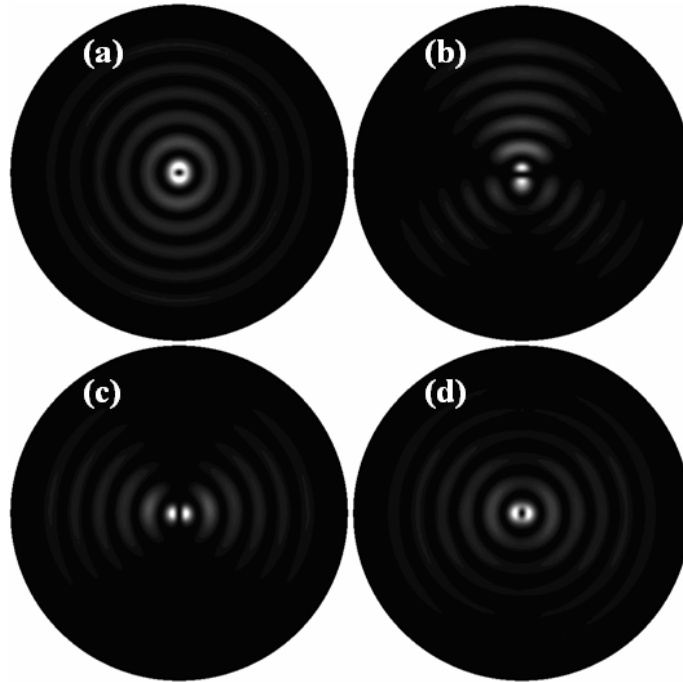
Fig. 4.4 Simulated LP_{16} mode profiles with (a) none (b) linear (c) quadratic and (d) exponential side cladding refractive-index change.

The FEM simulation results obtained are shown in Fig. 4.4, with the labels (a)–(d) denote none (unperturbed fiber), linear, quadratic, and exponential cladding RI change profiles of the fiber, respectively. The simulated results have a similar variation tendency with results shown in Fig. 4.3 and hence can qualitatively explain the relationship between the mode field distortion and the cladding RI change profile. This relationship can be understood by the fact that the mode field tends to shift toward the position where a larger RI exists. When compared with the linear profile, the latter two possess the cladding RI change mainly near the fiber surface, and therefore the cladding RI can be considered to be nearly

circularly symmetric at the cladding–core boundary. The mode fields of the latter two profiles tend to become standard LP_{16} modes, while the first profile is strongly angle-dependent.

4.1.3 Polarization Dependent Loss

In-fiber polarizer based on LPFG has received wide attentions. For example, such a device can be used as an in-line fiber polarizer [42] or a wavelength switching element in a fiber ring laser [43]. Different types of fibers, including polarization maintaining fiber, PCF, and hollow-core PBGF, have been used to make such devices [43-45]. The main reason for the polarization dependency is the asymmetric residual stress relaxation due to the single side laser irradiation.

The individual transmission spectrum and PDL of the three samples in section 4.1.2 with different defocused lengths are also investigated by an optical all-parameter analyzer (Agilent 81910A), as shown in Fig. 4.5. It should be noticed that since the air gap introduces a certain loss of laser energy, the larger the defocused length, the more scanning cycles are needed to write LPFG with similar resonant depth. The three samples here require scanning cycles of 7, 15, and 80, respectively. During the scanning process, no over-coupling appears.
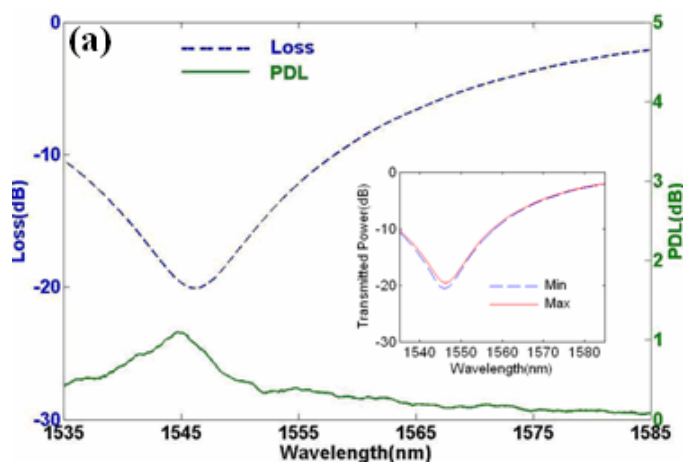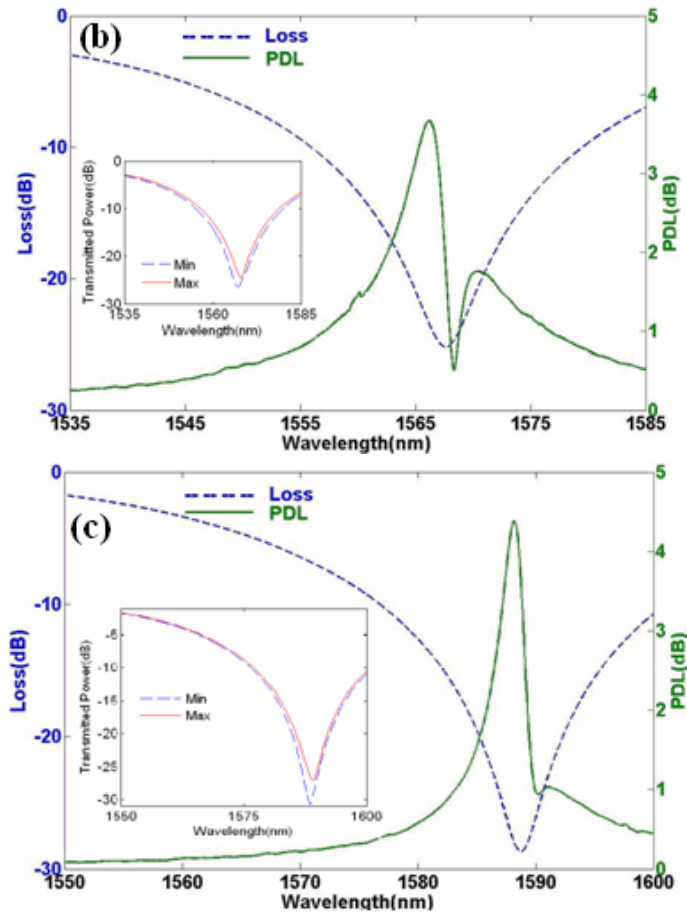
Fig. 4.5 PDL tests of LPFG with defocused lengths (a) 0 mm (b) 1 mm (c) 2 mm.

The PDL is calculated by means of the Mueller matrix method [46]. The LPFG written by the focused light beam possesses a maximum PDL of 1.10 dB, which is similar to that with large dimensional grooves (1.35 dB) [38] and edge-written (originally 1.22 dB) LPFG [47]. However, by applying the defocused laser beam for scanning and increasing the defocused length, the maximum PDL is greatly increased to 3.68 dB (for 1 mm) and 4.38 dB (for 2 mm), respectively. The polarization-induced dip changes of the three samples are 0.19, 0.95, and 0.6 nm, respectively. The three LPFG have similar values of a single-side 3 dB stop bandwidth of 32.46 nm, 32.53 nm, and 30.55 nm, respectively, which indicates that the PDL difference among them is mainly due to the different levels of photo-induced birefringence in the fiber.

Being different from that of the LPFG written with focused light beam [7, 39-41], the asymmetric residual stress relaxation distribution profile in the fiber cladding

cross section is the main reason for the enhancement of the polarization-dependent property [39]. In this situation, n_{eff}^{cl} decreases while n_{eff}^{co} changes little, as the RI change mainly occurs near the cladding surface. This also results in the different resonant wavelengths of the three samples in Fig. 4.5. Moreover, the simulation results in Fig. 4.4 demonstrate an increase in birefringence of the four-fold degenerated LP_{16} mode with 3×10^{-6}, 4×10^{-6}, and 7×10^{-6}, respectively. This increase in the cladding mode birefringence also contributes to the enhancement of the PDL in the LPFG written with single side laser irradiation [48]. LPFG fabricated with defocused CO_2 laser possesses a relatively large PDL compared with that obtained by conventional methods, which means that it can be effectively used as a polarization-sensitive element. The mode field profiles obtained at the corresponding resonant wavelength show that with the increase of the defocused length, the cladding area affected by the laser irradiation also increases, which results in the mode field distortion and thus an increase of PDL.

4.2 Micro-holes Based LPFG in All Solid Photonic Bandgap Fiber

LPFG can be inscribed in various types of optical fibers including PBGF [11, 23, and 49]. PBGF confines light through the bandgap effect instead of the conventional total internal reflection, exhibits different dispersion and nonlinear properties when compared with normal communication SMF and as a result, has received increased research attentions nowadays [50, 51]. PBGF can be divided into two types, hollow core and all solid PBGF. In all solid PBGF, the guidance is due to anti-resonant scattering from the high RI rods and the transmission spectrum consists of discrete frequency bands. The modal properties are thus very different from index guiding fibers, such as PCF and SMF. Compared with hollow core PBGF, all solid PBGF has the advantages of easy fabrication and small splicing loss with conventional SMF as no air hole collapse occurs [52].

The non-photosensitive all solid PBGF used in this section (made by Yangtze Optical Fiber and Cable, YOFC Ltd.) has 5 layers of high RI rods with a period of 9.6 μm. A buffering loop (with the diameter of 7.3 μm) lies around each rod. The buffering loop is fluorine-doped, which acts as an index-depressed layer around the high RI rods (germanium-doped) in the unit cell of photonic crystal cladding [53]. The RI (at 1550nm) of the high RI rod, the buffering loop and the cladding are 1.4807, 1.4356, and 1.444, respectively. These parameters will be used in the simulation later. The cross section of the fiber is shown in Fig. 4.6.
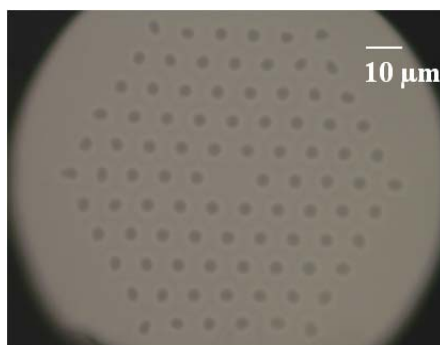
Fig. 4.6 Cross section of the all solid PBGF with a buffering loop lies around each high RI rod.

4.2.1 Micro-holes Based LPFG Fabrication

Compared with normal SMF, the high RI rods and the buffering loops of the all solid PBGF will induce different internal stress distribution and thus the fs laser fabrication parameters need to be adjusted. Through several trail processes, it is found that the full through micro-hole may make the all solid PBGF extremely brittle. For drilling half through micro-holes into the all solid PBGF, the MO is selected with its magnification of 20× and NA of 0.8. The on-target pulse energy is set as 6.3 μJ and kept constant during the experiments. The fs laser irradiation time is set as ~40 s for each micro-hole. The focus point is located at the cladding surface and aimed at the core central axis. By drilling micro-holes periodically, a structural modulated LPFG device is fabricated. The micro-hole

scale is about 62 μm in depth (close to the cladding radius) with a cone angle of 5 degree (corresponds to 11 μm in width at the cladding surface). The micro-hole morphology in all solid PBGF is shown in Fig. 4.7.
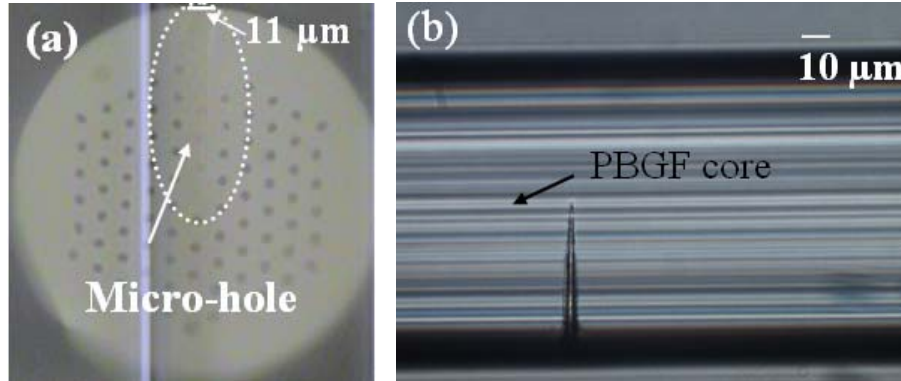
Fig. 4.7 Morphology of the half through micro-hole in all solid PBGF (a) cross section view (the lines is resulted from CCD synchronized noise) (b) side view.

4.2.2 Properties of Micro-holes Based LPFG

The transmission spectrum of the LPFG is measured by the OSA with a resolution of 0.5 nm. The evolution of the transmission spectrum of one LPFG sample with a period of 610 μm is shown in Fig. 4.8 (a). The resonant wavelength of the device is located at 1390.9 nm. The insertion loss is 14.40 dB and the resonant depth is 25.96 dB (which is estimated as the difference between the transmission loss at the resonant wavelength and the insertion loss). The high insertion loss may be due to the following reasons: 1) the fabrication will remove part of the fiber core; 2) the surface roughness of the microhole may result in light scattering; and 3) the small difference in the focus position and the size for each micro-hole, which affects the uniformity of the grating structure and leads to the increase of the light scattering. In order to improve the grating behavior, a more precise focus position should be achieved. Besides, the pulse energy and the irradiation time should also be carefully adjusted as smaller pulse energy together with longer irradiation time result in a smoother inner micro-hole surface. Figure 4.8 (b) demonstrates the transmission spectra for the LPFG with

different periods under the same laser exposure condition. The grating periods are 585, 500, 400 and 380 μm, with the corresponding resonant wavelengths of 1474.2, 1510.9, 1596.2 and 1621.4 nm, respectively. These LPFG have the period number of 10, 11, 8 and 11, respectively. The spectra in Fig. 4.8 are not so clean, which is due to the noise of the broadband light source used in the experiments. The resonant wavelength of each sample is determined by measuring the dip value of the transmission spectrum. For example, in Fig. 4.8 (b), the spectra are smooth at their dips and the resonant wavelengths can be determined unambiguously except for that with the period of 585 μm.
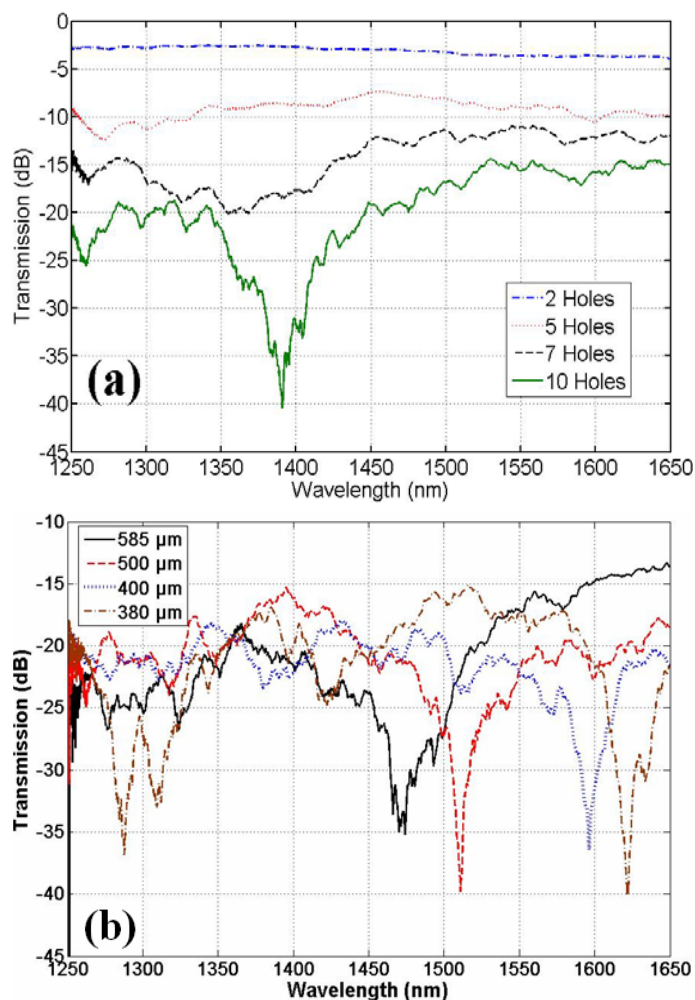
Fig. 4.8 Transmission spectra of (a) selected evolution spectra of one LPFG with the number of the micro-hole (b) LPFG samples with different periods.

The total grating length of the LPFG fabricated by fs laser micromachining is much smaller than that written in normal SMF, which is due to the extremely

strong structural RI modulation. The polarization dependent property of the device proposed is studied in another sample with a period of 400 μm. A fiber polarizer is used to change the broadband light into a certain state of polarization (SOP) and a polarization controller is used to change the SOP. The maximum resonant wavelength change is 1 nm (from 1598 to 1597 nm) and the maximum PDL obtained is 7.6dB, as shown in Fig. 4.9. The high PDL may be induced by the one side structure modulation, which results in a strong asymmetry in fiber waveguide and affects the birefringence of both core mode and cladding mode.
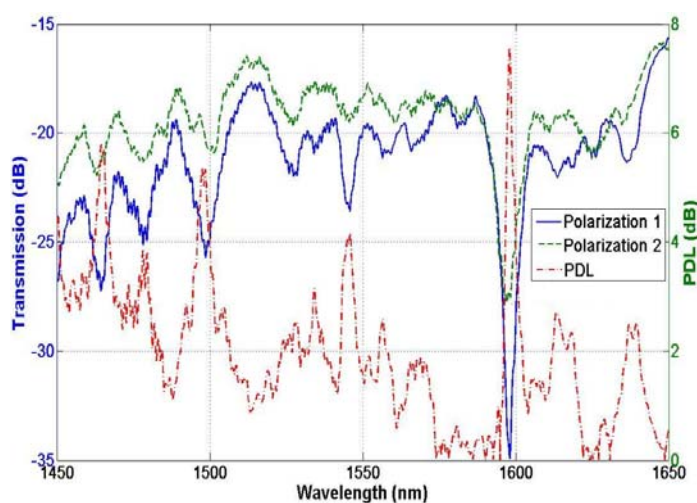
Fig. 4.9 Polarization dependent property of a sample with the period of 400 μm.

4.2.3 Mode Coupling

For LPFG fabricated in all solid PBGF, the mode coupling may occur between the fundamental core mode and either cladding modes or guided supermodes [49]. In order to identify the modes involved, the sample shown in Fig. 4.8 (a) is cut off at the grating end and its near-field mode is measured by an infrared CCD (Electrophysics 7290A) and a tunable laser (Agilent 8164B). The sample is immersed in liquid with RI of 1.32, which changes the resonant wavelength to 1500.3 nm so as to fit in the minimum wavelength of the tunable laser at 1494 nm. Fig. 4.10 (a) shows the fundamental mode of the sample away from the resonant wavelength, where most of the light energy is confined in the fiber core

except one high RI rod (this may due to the surface roughness of the cross section induced by cleaving). Fig. 4.10 (b) shows the mode profile at the resonant wavelength and when compared with that in Fig. 4.10 (a), it is clearly seen that the fundamental mode has split into three parts. This mode field profile is considered to be the LP_{11} high order mode: the upper half (along the laser irradiating direction) of the LP_{11} mode is split into two parts by the micro-hole structure; while the lower half remains without obvious deformation.
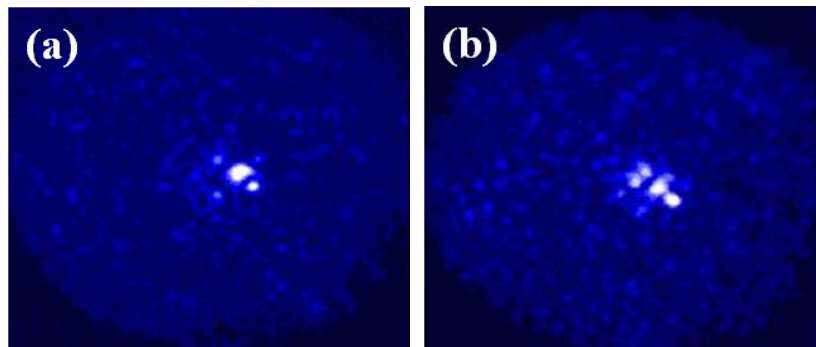
Fig. 4.10 Near-field mode profile of the sample in Fig. 4.8 (a) when the external RI is 1.32 (a) LP_{01} core mode (b) LP_{11} cladding mode.

The mode field properties of the micro-hole based LPFG in all solid PBGF can also be simulated by use of FEM. The simulation model is shown in Fig. 4.11, with the parameters set according to the all solid PBGF and the micro-hole dimensions stated before and the external RI is set as 1.32. The results obtained are shown in Fig. 4.12 (a)~(d), which agrees with the observed results in Fig. 4.10. For simplicity, only the mode fields near the fiber core is displayed.
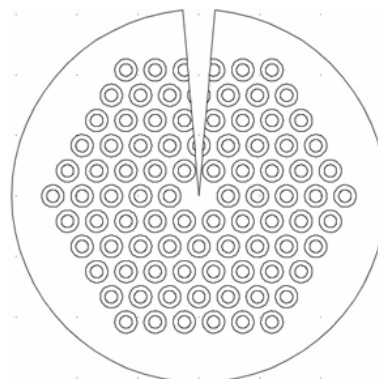
Fig. 4.11 FEM simulation model of the micro-hole in all solid PBGF.
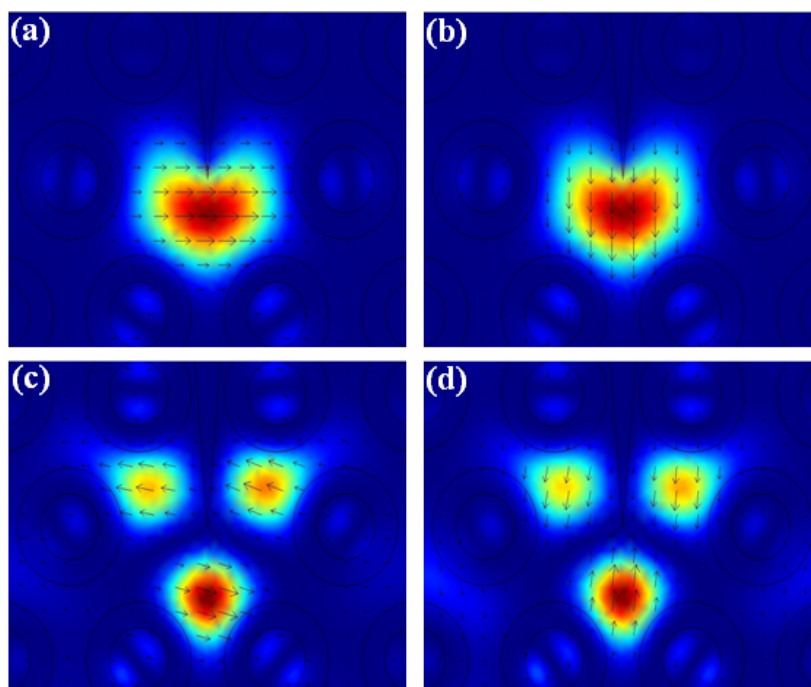
Fig. 4.12 FEM simulation results of (a, b) the two-fold symmetry LP_{01} core mode; (c, d) the two-fold symmetry LP_{11} cladding mode.

In the simulation results, the black arrows represent both the direction and the magnitude of the modes electric field. The simulation demonstrates that both the core mode and the cladding mode have two-fold symmetry: one with electric field direction parallel to the micro-hole and the other perpendicular to the micro-hole. Both the LP_{01} mode and LP_{11} mode are mainly restricted in the fiber core. The phase matching curve (when external RI is 1.0) for the coupling between the LP_{01} core mode and the LP_{11} cladding mode is also simulated by FEM, as shown in Fig. 4.13. For the purpose of comparison, the experimental phase matching curve, as data from Fig. 4.8(b), is also plotted in Fig. 4.13. Both the curves show the decrease in resonant wavelength when the grating period increases. The difference between the simulation and the experiment results may be mainly caused by discrepancy between the simulation model and the actual micro-hole dimension. Besides, the material dispersion, which is neglected during the simulation and the dimension unconformity among the individual micro-holes will also result in the difference, as a slight deviation of the laser

focus spot at the cladding surface leads to a large shift of the microhole tip in the fiber core, which strongly affects the structural modulated RI change.
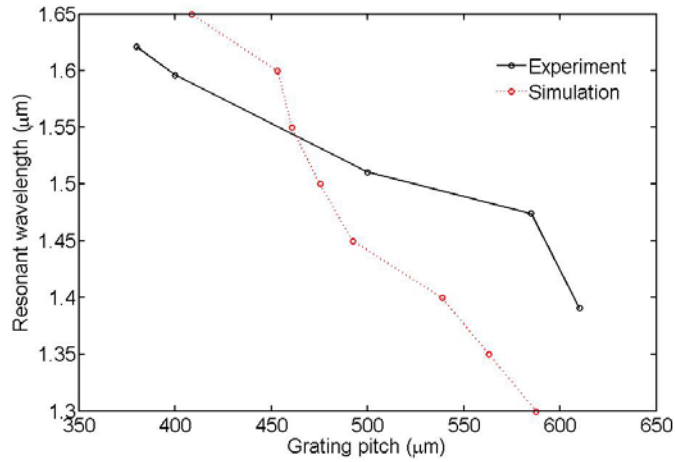
Fig. 4.13 Phase matching curve for coupling between the fundamental mode and LP_{11} like cladding mode (solid line: experimental result; broken line: simulation result).

4.2.4 Application for RI sensing

The sample in Fig. 4.8 (a) is also immersed in different RI liquids to measure the resonant wavelength change before being cut off. When the external RI changes from 1.30 to 1.35, the resonant wavelength shift is 23.7nm (from 1485.6 to 1509.3 nm). The average external RI sensitivity in the range 1.30-1.35 is estimated of 537 nm/RIU, as shown in Fig. 4.14.
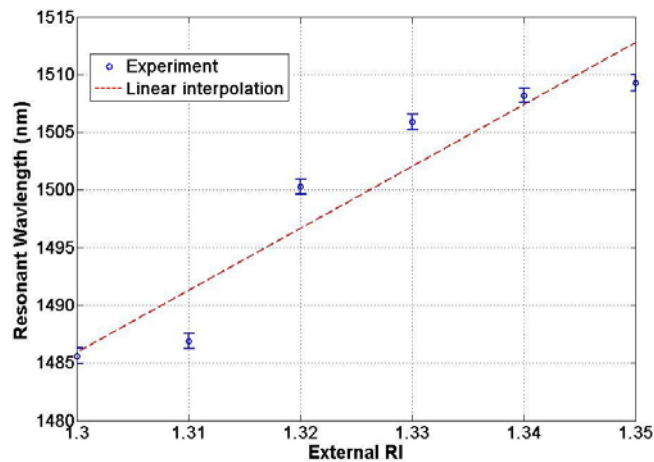
Fig. 4.14 Resonant wavelength shift of the sample in Fig. 4.8 (a) when the external RI changes from 1.30 to 1.35 (circles: experiment data with error bar; broken line: linear interpolation).

The DL of RI sensing is defined as DL=R/S, where R is the sensor resolution and S is the sensitivity. R can be estimated as follows [54]: 1) the amplitude noise (with an assuming *SNR* of 60 dB) $\sigma_{amp} = \Delta\lambda/(4.5SNR^{0.25})$; 2) the temperature stabilization, which is neglected here; 3) the 0.5 nm wavelength resolution has a uniform error distribution of $\sigma_{spe} = 0.5/\sqrt{12} \approx 0.14$ nm. And the estimated error of the resonant wavelength can be obtained as $3\sigma = 3\sqrt{\sigma_{amp}^2 + \sigma_{spe}^2}$. The DL is estimated to be 4×10^{-3} RIU. The RI sensing results obtained are shown in Fig. 4.14. The error performance poor since the 3-dB bandwidth $\Delta\lambda$ is quite large (~90 nm). Besides, the resonant wavelength response to the RI may not be linear.

Compared with LPFG written in SMF of similar periods (~50 nm/RIU) [55, 56], the relatively high external RI sensitivity of the resonant wavelength change obtained has potential applications in RI sensing in the range around water. The external RI change will lead to the effective RI change of the core mode and the cladding mode simultaneously. Thus, the dispersion of both the core mode and the cladding mode needs to be taken into account, while for LPFG in SMF [56], only the cladding mode stands for the RI sensitivity. The present RI sensitivity is not as high as that reported (~1500 nm/RIU) in PCF based refractometer [57]. However, the proposed structure is more convenient for external RI sensing as no infiltrating liquid into the PCF is required, the process of which is difficult and time-consuming. Another advantage of the device proposed is that the liquid sample can be flexibly changed after each measurement.

4.3 Asymmetrically Located Micro-holes Based LPFG in SMF

Due to the fiber price, it is favourable to develop micro-hole based LPFG in SMF as those fabricated in all solid PBGF. However, substantial fabrication difficulty has been found when implementing symmetrically located micro-hole

based LPFG in SMF, since the core mode area of SMF is smaller than that of the all solid PBGF, which implies a much smaller tolerance in geometrical non-uniformity. The depth and location of the micro-holes will critically affect the mode properties in SMF, and the inevitable processing errors in the geometrical parameters of the micro-holes may virtually restrain the mode resonance in SMF. Moreover, for symmetric located micro-holes, the FPI effect discussed in section 3.2.1 is much stronger in SMF than that in all solid PBGF, because of the different light guiding mechanism between the two fibers.

In this section, the fabrication of asymmetric micro-hole based LPFG by use of fs laser is presented. Such an LPFG exhibits a relatively large tolerance to geometry errors of the micro-holes and thus can be readily fabricated in the low cost SMF. Moreover, a clearly decreased insertion loss and an almost linear resonant wavelength shift to the external RI around water can be obtained.

4.3.1 LPFG Fabrication

In the experiment, the MO is selected with its magnification of 10× and an NA value of 0.25. The focus point is located at cladding surface but positioned 6 μm away from the core center in the y-direction (in Fig. 2.5). The pulse energy is 15 μJ and the irradiation time for each micro-hole is ~30 s. Multiple micro-holes are drilled with the same conditions and each time after one micro-hole is created, the fiber is shifted with one grating period along the length. This process continues until the LPFG with apparent resonance dip can be observed. Fig. 4.15 shows the geometry schematic, cross section view and side view of the asymmetric located micro-holes.
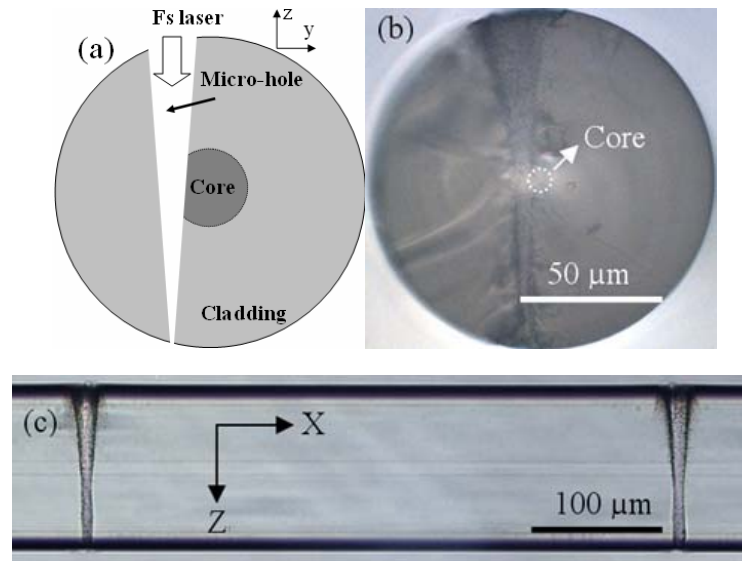
Fig. 4.15 Morphology of the asymmetrically located micro-hole (a) geometry schematic (b) cross section view (c) side view (of a sample with period of 450 μm).

4.3.2 LPFG Performance and Mode Coupling

The transmission spectra evolution of a sample with the grating period of 450 μm is shown in Fig, 4.16 (a). The transmission loss increases before obvious resonant dip shows up for the first seven micro-holes. After 15 grating periods are fabricated, the depth of the resonance peak around 1517 nm becomes the deepest (over 20 dB). The insertion loss of the final device is ~5 dB, which is much smaller compared with that in all solid PBGF (~14.40 dB as shown in Fig. 4.8). The resonant depth would dramatically decay if more number of micro-holes were drilled due to overcoupling. The resonant peak near 1404 nm is created due to the coupling of the fundamental core mode to cladding mode. The near-field mode profiles of the core mode (at 1600 nm) and cladding mode at the resonant wavelength (at 1517.4 nm) are observed, as shown in Fig. 4.16 (b) and (c). For the core mode shown in Fig. 4.16 (b), the fringes distributed in the cladding region may be caused by the scattering of the micro-holes. The mode field profile in Fig. 4.16 (c) presents a dispersive intensity distribution of the LP_{16} cladding mode, but slightly affected by the background noise.
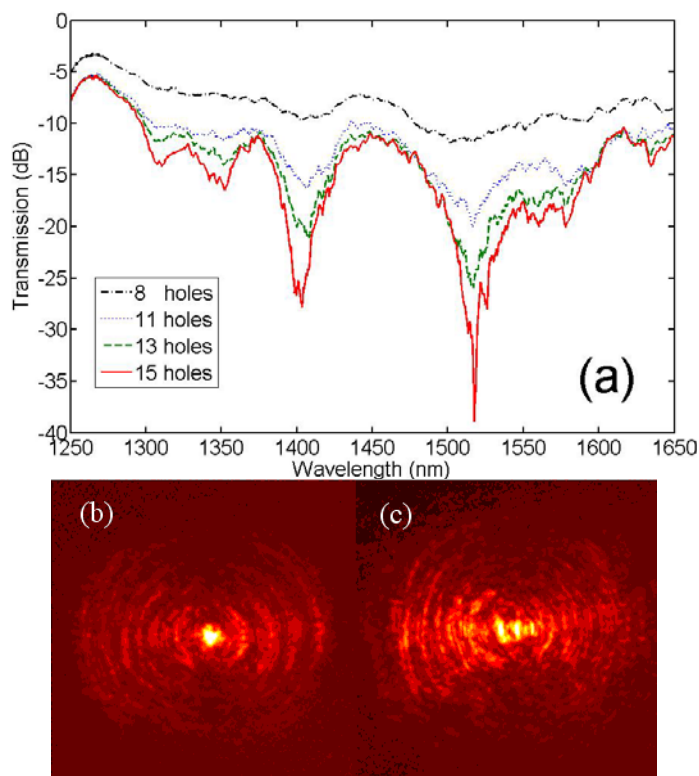
Fig. 4.16 (a) Transmission spectra evolution with the number of micro-hole and near-field mode of (b) core mode at 1600 nm (c) LP_{16} cladding mode at 1517.4 nm. The grating period is 450 μm.

The experimental and calculated phase matching curves of such kind of LPFG are presented in Fig. 4.17. The simulation is performed with an FEM model established according to Fig. 4.15 (a) with the following parameters: fiber core diameter D_{co}=8.2 μm, fiber cladding diameter D_{cl}=125 μm, fiber core RI n_{co}=1.4689, cladding RI n_{cl}=1.4636, cone angle of the micro-hole θ=7.4°, removed fiber core width d=1.4 μm, micro-hole diameter at the fiber core-cladding interface D=6.5 μm. The material dispersion is neglected in the simulations. The calculated phase matching curve for the coupling between the LP_{01} core mode and the LP_{16} cladding mode is shown as the blue curve in Fig. 4.17 (a). Several samples with grating periods from 400 to 460 μm are fabricated and found that the resonant wavelengths were in good agreement with the simulation results. Fig. 4.17 (b) illustrates the transmission spectra of the samples with grating period of 410, 430 and 460 μm, respectively. The visibilities of the resonance peaks are all over 20 dB.
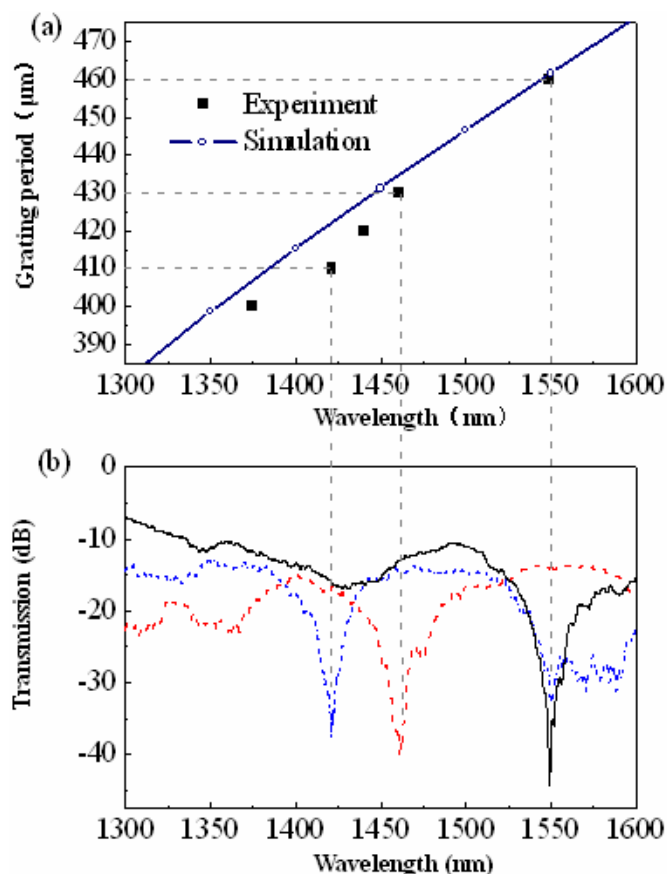
Fig. 4.17 (a) Experimental and simulated relation between the resonant wavelength and the grating period (b) transmission spectra of samples with grating period of 410, 430 and 460 μm.

4.3.3 Application for RI sensing

In order to investigate the RI response of the asymmetrically located micro-hole based LPFG in SMF, a sample with period of 430 μm is immersed into a series of RI liquids. The RI of the liquids used are in the range of 1.31-1.38 (@589.3 nm). The resonance wavelength change is plotted in Fig. 4.18, with an average RI sensitivity obtained ~190 nm/RIU in the investigated RI range. With the increase of the surrounding RI, the resonant wavelength experiences a "red shift", which is different from the "blue shift" characteristic of the conventional LPFG fabricated by UV or CO_2 laser [53, 54]. Besides, the resonant wavelength shift has a linear response to the change of the external RI in this region.
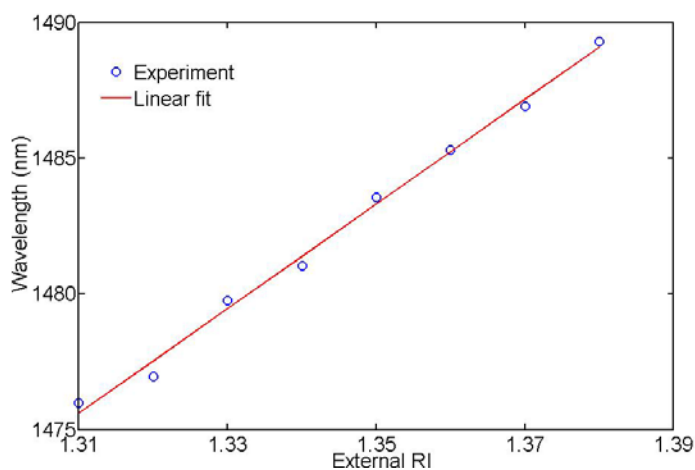
Fig. 4.18 RI response of the sample with a grating period of 430 μm.

4.4 Discussion

According to the CLM theory discussed in section 4.1.1, for LPFG with strong waveguide variation, such as the structural modulated LPFG based on periodical drilling of micro-holes, the mode energy coupling would mainly occur at each waveguide variation region, which means only the core mode and the cladding mode field profiles at that region need to be taken into account. These modes will keep constant with each mode field profile and effective RI while propagating along the remaining unperturbed fiber, until they reach the next waveguide perturbation. Therefore in section 4.2 and 4.3, only the mode field profiles at the waveguide geometry variation are simulated.

The transmission spectra of the micro-hole based LPFG, fabricated either in all solid PBGF or SMF, are not as clean as those conventional LPFG fabricated by CO_2 or UV laser. The most important reason stands for this phenomenon is the geometry non-uniformity among individual micro-hole, which may result from either the pulse energy fluctuation or focus point location difference. The slight difference exists in the waveguide perturbation may result in a significant mode field distribution variation, which makes the phase matching condition much more complex than that expressed in Eq. (4.8) and thus a broader bandwidth of

the transmission dip will be obtained. Since each micro-hole induces such a strong structural modulation, the number of grating period required is then much smaller than conventional LPFG and thus enables a compact device dimension.
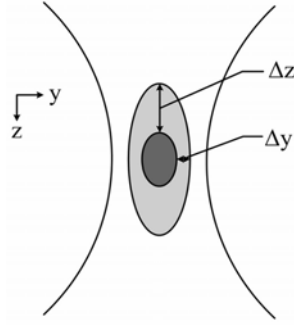
Fig. 4.19 Illustration of geometry errors induced by irradiation dosage fluctuation. The dark grey elliptical area represents the ablation zone of a lower energy pulse, and the light grey elliptical area represents that of a higher energy pulse, Δy and Δz represent the error in y- and z-direction.

Compared with symmetrically located micro-holes, the asymmetrically located ones can effectively lower the insertion loss since they remove a smaller part of fiber core. And the less geometric errors would be induced by the irradiation dosage fluctuation in the vicinity of the focus point, as shown in Fig. 4.19. Since the Rayleigh length (in the z-direction) is much larger than the focused beam diameter (in the y-direction), the irradiation dosage fluctuation induced geometric error in the z-direction, Δz, is also much larger than that in the y-direction, Δy. Thus, asymmetrically located micro-holes that fully penetrate through the fiber with side-wall contact of fiber core will result in less geometry error, and thus smaller non-uniformity of each micro-hole perturbation compared with the half through symmetric micro-holes that penetrate into fiber core. However, more number of micro-holes is required.

4.5 Summary

In this chapter, the general theory of CLM for LPFG with strong waveguide modulation is introduced, which divides the fiber into two parts: the waveguide perturbation region and imperturbation region. The CLM implies that mode

coupling can only occur between the fiber core mode and cladding mode in the waveguide perturbation region, which is different from that of conventional CMT that usually applied in most previous literatures. A numerical simulation method by separating the waveguide perturbation region into small thin pieces is introduced for calculating the transmission spectrum of such kind of strong modulated LPFG.

The LPFG performances, including its transmission spectrum, mode filed profile, PDL, and phase matching condition, strongly depend on its RI modulation symmetry. A simple investigation of the effects of the RI modulation symmetry is carried out on several LPFG written in SMF by CO_2 laser, with different defocused lengths, which leads to different asymmetric RI modulation profile. It is found that with a larger asymmetry RI modulation (or the local RI change mainly occurs near the fiber cladding surface), the cladding mode at the resonant wavelength suffers a stronger distortion and thus results in a larger PDL.

By fs laser periodically drilling micro-holes into the fiber, a novel kind of structural modulated LPFG can be effectively created. Each micro-hole induces a relative strong structural modulation (or waveguide perturbation) into the fiber, which can effectively couples light energy from the core mode to certain cladding mode according to the CLM theory. Two different types of micro-hole based LPFG are developed, the symmetrically located micro-holes for all solid PBGF and asymmetrically located micro-holes for SMF. Both the devices can be applied as RI sensors. The individual cladding mode profiles are investigated for each type. The asymmetrically located micro-holes can effectively reduce the waveguide geometry error induced by the irradiation dosage fluctuation and thus can enhance the uniformity and lower the scattering loss.

References for Chapter 4

1. A. M. Vengsarkar, P. J. Lemaire, J. B. Judkins, et al, "Long-period fiber gratings as band rejection filters," J. Lightwave Technol. **14**, 58–65 (1996).

2. A. M. Vengsarkar, J. R. Pedrazzani, J. B. Judkins, et al, "Long-period fiber-grating-based gain equalizers," Opt. Lett. **21**, 336-338 (1996).

3. V. Bhatia, A. M. Vengsarkar, "Optical fiber long-period grating sensors," Opt. Lett. **21**, 692-694 (1996).

4. B. J. Eggleton, P. S. Westbrook, R. S. Windeler, et al, "Grating resonances in air-silica microstructured optical fibers," Opt. Lett. **24**, 1460-1462 (1999).

5. B. J. Eggleton, P. S. Westbrook, C. A. White, et al, "Cladding-Mode-Resonances in Air-Silica Microstructure Optical Fibers," J. Lightwave Technol. **18**, 1084-1100 (2000).

6. V. Bhatia, "Applications of long-period gratings to single and multi-parameter sensing," Opt. Express. **4**, 457-466 (1999).

7. D. D. Davis, T. K. Gaylord, E. N. Glytsis, et al, "Long-period fibre grating fabrication with focused CO_2 laser pulses," Electron. Lett. **34**, 302-303 (1998).

8. G. Kakarantzas, T. E. Dimmick, T. A. Birks, et al, "Miniature all-fiber devices based on CO_2 laser microstructuring of tapered fibers," Opt. Lett. **26**, 1137-1139 (2001).

9. Y. J. Rao, Y. P. Wang, Z. L. Ran, et al, "Novel fiber-optic sensors based on long-period fiber gratings written by nigh-frequency CO_2 laser pulses," J. Lightwave. Technol. **21**, 1320-1327 (2003).

10. Y. P. Wang, L. M. Xiao, D. N. Wang, et al, "Highly sensitive long-period fiber-grating strain sensor with low temperature sensitivity," Opt. Lett. **31**, 3414-3416 (2006).

11. Y. Wang, W. Jin, J. Ju, et al, "Long period gratings in air-core photonic bandgap fibers," Opt. Express **16**, 2784-2790 (2008).

12. G. Rego, O. Okhotnikov, E. Dianov, et al, "High-temperature stability of

long-period fiber gratings produced using an electric arc," J. Lightwave. Technol. **19**, 1574-1579 (2001).

13. H. Dobb, K. Kalli, D.J. Webb, "Temperature-insensitive long period grating sensors in photonic crystal fibre," Electron. Lett. **40**, 657-658 (2004).

14. G. Humbert, A. Malki, S. Février, et al, "Characterizations at high temperatures of long-period gratings written in germanium-free air silica microstructure fiber," Opt. Lett. **29**, 38-40 (2004).

15. G, Rego, R. Falate, J. L Santos, "Arc-induced long-period gratings in aluminosilicate glass fibers," Opt. Lett. **30**, 2065-2067 (2005).

16. Y. Kondo, K. Nouchi, T. Mitsuyu, et al, "Fabrication of long-period fiber gratings by focused irradiation of infrared femtosecond laser pulses," Opt. Lett. **24**, 646-648 (1990).

17. E. Fertein, C. Przygodzki, H. Delbarre, "Refractive-index changes of standard telecommunication fiber through exposure to femtosecond laser pulses at 810 cm," Appl. Opt. **40**, 3506-3508 (2001).

18. A. I. Kalachev, D. N. Nikogosyan, G. Brambilla, "Long-period fiber grating fabrication by high-intensity femtosecond pulses at 211 nm," J. Lightwave. Technol. **23**, 2568-2578 (2005).

19. T. Allsop, M. Dubov, A. Martinez, et al, "Bending characteristics of fiber long-period gratings with cladding index modified by femtosecond laser," J. Lightwave. Technol. **24**, 3147-3154 (2006).

20. C. R. Liao, Y. Wang, D. N. Wang, et al, "Femtosecond laser inscribed long-period gratings in all-solid photonic bandgap fibers," IEEE Photon. Technol. Lett. **22**, 425-427 (2010).

21. I. K. Hwang, S. H. Yun, B. Y. Kim, "Long-period fiber gratings based on periodic microbends," Opt. Lett. **24**, 1263-1265 (1999).

22. S. Savin, M. J. F. Digonnet, G. S. Kino, et al, "Tunable mechanically induced long-period fiber gratings," Opt. Lett. **25**, 710-712 (2000).

23. P. Steinvurzel, E. D. Moore1, E. C. Mägi, et al, "Long period grating resonances in photonic bandgap fiber," Opt. Express. **14**, 3007-3014 (2006).

24. C. Y. Lin, L. A. Wang, G. W. Chern, "Corrugated long-period fiber gratings as strain, torsion, and bending sensors," J. Lightwave. Technol. **19**, 1159-1168 (2001).

25. Y. Jiang, Q. Li, C. H. Lin, et al, "A novel strain-induced thermally tuned long-period fiber grating fabricated on a periodic corrugated silicon fixture," IEEE Photon. Technol. Lett. **14**, 941-943 (2002).

26. M. Fujimaki, Y. Ohki, J. L. Brebner, et al, "Fabrication of long-period optical fiber gratings by use of ion implantation," Opt. Lett. **25**, 88-89 (2000).

27. M. L. V. Bibra, A. Roberts, J. Canning, "Fabrication of long-period fiber gratings by use of focused ion-beam irradiation," Opt. Lett. **26**, 765-767 (2001).

28. S. W. James, R. P. Tatam, "Optical fibre long-period grating sensors: characteristics and application," Meas. Sci. Technol. **14**, R49-R61 (2003).

29. Y. J. Rao, T. Zhu, Z. L. Ran, et al, "Novel long-period fiber gratings written by high-frequency CO_2 laser pulses and applications in optical fiber communication," Opt. Commun. **229**, 209-221 (2004).

30. Y. Wang, "Review of long period fiber gratings written by CO_2 laser," J. Appl. Phys. **108**, 081101 (2010).

31. T. Erdogan, "Fiber grating spectra," J. Lightwave. Technol. **15**, 1277-1294 (1997).

32. A. W. Snyder, J. D. Love, *Optical Waveguide Theory*, Chapman & Hall: London, U.K. (1983).

33. L. Jin, W. Jin, J. Ju, et al, "Coupled local-mode theory for strongly modulated long period gratings," J. Lightwave. Technol. **28**, 1745-1751 (2010).

34. C. Zhang, K. S. Chiang, "CO_2 laser-written long-period fiber gratings in a germanium–boron codoped fiber: effects of applying tension during the writing process," IEEE Photon. Technol. Lett. **21**, 1456-1458 (2009).

35. R. Slavik, "Coupling to circularly asymmetric modes via long-period

gratings made in a standard straight fiber," Opt. Commun. **275**, 90–93 (2007).

36. D. D. Davis, T. K. Gaylord, E. N. Glytsis, et al, "CO_2 laser-induced long-period fiber gratings: spectral characteristics, cladding modes and polarization independence," Electron. Lett. **34**, 1416–1417 (1998).

37. O. V. Ivanov, G. Rego, "Origin of coupling to antisymmetric modes in arc-induced long-period fiber gratings," Opt. Express **15**, 13936-13941 (2007).

38. Y. P. Wang, D. N. Wang, W. Jin, et al, "Asymmetric long-period fiber gratings fabricated by use of CO_2 laser to carve periodic grooves on the optical fiber," Appl. Phys. Lett. **89**, 151105 (2006).

39. H. S. Ryu, Y. Park, S. T. Oh, et al, "Effect of asymmetric stress relaxation on the polarization-dependent transmission characteristics of a CO_2 laser-written long-period fiber grating," Opt. Lett. **28**, 155–157 (2003).

40. B. H. Kim, Y. Park, T.-J. Ahn, et al, "Residual stress relaxation in the core of optical fiber by CO_2 laser irradiation," Opt. Lett. **26**, 1657–1659 (2001).

41. T. Hirose, K. Saito, S. Kojima, B. Yao, et al, "Fabrication of long-period fiber grating by CO_2 laser-annealing in fiber-drawing process," Electron. Lett. **43**, 443–445 (2007).

42. A. S. Kurkov, M. Douay, O. Duhem, et al, "Long-period fiber grating as a wavelength selective polarization element," Electron. Lett. **33**, 616–617 (1997).

43. Y. W. Lee, B. Lee, "Wavelength-switchable erbium-doped fiber ring laser using spectral polarization-dependent loss element," IEEE Photon. Technol. Lett. **15**, 795–797 (2003).

44. H. F. Xuan, W. Jin, J. Ju, et al, "Hollow-core photonic bandgap fiber polarizer," Opt. Lett. **33**, 845–847 (2008).

45. Y. P. Wang, L. M. Xiao, D. N. Wang, et al, "In-fiber polarizer based on a long-period fiber grating written on photonic crystal fiber," Opt. Lett. **32**, 1035–1037 (2007).

46. Y. P. Wang, D. N. Wang, W. Jin, et al, "Mode field profile and polarization

dependence of long-period fiber gratings written by CO2 laser," Opt. Commun. **281**, 2522–2525 (2008).

47. T. Zhu, Y. J. Rao, J. L. Wang, et al, "A highly sensitive fiber-optic refractive index sensor based on an edge-written long-period fiber grating," IEEE Photon. Technol. Lett. **19**, 1946–1948 (2007).

48. B. L. Bachim, T. K. Gaylord, "Polarization-dependent loss and birefringence in long-period fiber gratings," Appl. Opt. **42**, 6818–6823 (2003).

49. L. Jin, Z. Wang, Y. Liu, et al, "Ultraviolet-inscribed long period gratings in all-solid photonic bandgap fibers," Opt. Express **16**, 21119–21131 (2008).

50. F. Luan, A. K. George, T. D. Hedley, et al, "All-solid photonic bandgap fiber," Opt. Lett. **29**, 2369–2371 (2004).

51. A. Bétourné, G. Bouwmans, Y. Quiquempois, et al, "Improvements of solid-core photonic bandgap fibers by means of interstitial air holes," Opt. Lett. **32**, 1719–1721 (2007).

52. Y. Li, D. N. Wang, L. Jin, "Single-mode grating reflection in all-solid photonic bandgap fibers inscribed by use of femtosecond laser pulse irradiation through a phase mask," Opt. Lett. **34**, 1264–1266 (2009).

53. G. Ren, P. Shum, L. Zhang, et al, "Low-loss all-solid photonic bandgap fiber," Opt. Lett. **32**, 1023-1025 (2007).

54. I. M. White, X. Fan, "On the performance quantification of resonant refractive index sensors," Opt. Express **16**, 1020–1028 (2008).

55. J. H. Chong, P. Shum, H. Haryono, et al, "Measurements of refractive index sensitivity using long-period grating refractometer," Opt. Commun. **229**, 65–69 (2004).

56. X. Shu, L. Zhang, I. Bennion, "Sensitivity characteristics of long-period fiber gratings," J. Lightwave Technol. **20**, 255–266 (2002).

57. L. Rindorf, O. Bang, "Highly sensitive refractometer with a photonic-crystal-fiber long-period grating," Opt. Lett. **33**, 563–565 (2008).

Chapter 5 Fiber Bragg Grating Sensor Integrated with Micro-holes

Fiber in-line RI sensors are attractive for chemical, biological and environmental sensing because of their compactness, convenient operation, low cost and many other advantages provided by optical fibers. However, most of the liquids to be measured are temperature sensitive, which makes it difficult to determine their RI values accurately because of the temperature induced cross sensitivity [1]. It is therefore necessary to implement the simultaneous measurement of RI and temperature. Various types of OFS have been developed for this purpose, including sampled FBG, hybrid structure of FBG and LPFG, cascaded LPFG, tilted FBG, D-type fiber, FBG embedded in polished fiber or etched fiber, double cladding fiber and fiber interferometers, etc. [1-13]. In general, most of these sensors determine the two parameters by simultaneously monitoring two characteristic wavelengths, and the corresponding demodulating systems are therefore complex. The usually involved nonlinear RI response due to evanescent-field coupling [14] also leads to a rather complicated sensitivity matrix (e.g., different matrix coefficients exist in different RI ranges, or the matrix is expressed as the sum of polynomials in different orders [2]), and significant difficulties in performing automatic and real-time measurement.

By use of fs laser micro-machining, the micro-hole based RI sensor developed in Chapter 3 has been demonstrated with the advantages of easy for fabrication and capable of performing temperature independent RI measurement. The RI sensitivity of the device would be further increased if more micro-holes could be drilled along the fiber length. Recently, several kinds of FBG embedded micro-structures, including micro-channel, micro-slot based hybrid waveguide, and MZI developed in Chapter 3, are developed, which can be applied for

simultaneous temperature and RI measurement [15-17].

In this chapter, a simple micro-structure OFS for simultaneous and independent RI and temperature measurement is proposed and demonstrated. The sensor is based on a number of asymmetrically located micro-holes mainly positioned in the FBG region, which enables the fiber core interact with the surrounding medium. Since the asymmetrically located micro-holes hardly destroy the periodic structure of the FBG, the temperature change can still be determined by observing the resonant wavelength shift of the FBG. Thus the temperature and RI sensing can be carried out independently by detecting the FBG resonant wavelength shift and its intensity variation, respectively. The system is convenient in operation and supports simple demodulation method by monitoring only one characteristic wavelength. This kind of device is a good example for integration of micro-structure in fiber with other sensing element inscribed in advance.

5.1 Device Fabrication

In the experiment, a second order type-II FBG with 3 mm grating length is fabricated in SMF (without hydrogen loaded) by use of fs laser irradiation through a phase mask in advance [19] and mounted on the 3D stage. For type-II FBG, the induced index change is likely to be a result of plasma formation caused by multi-photon and avalanche ionization process, which requires a higher power threshold than that of type-I FBG. The high laser power may affect the fiber glass structure and create a damage region inside the fiber, and the periodical damage along the fiber forms the grating structure [20]. Fs laser pulses are then focused onto the SMF cladding surface through a 20× MO with the NA value of 0.50. The pulse energy is set as 10 μJ, with an irradiation time of ~60 s. These parameters are kept constant during the fabrication to ensure a good micro-hole drilling repeatability. The focus point is ~4 μm away from the

fiber core center, along the y-direction and on the cladding surface. The first micro-hole is located at the grating edge. Altogether 8 micro-holes are drilled, with the hole-spacing of 500 μm. The device here is not just a combination of micro-holes and FBG as: 1) most of the micro-holes are fabricated within the grating region, which supports a compact device dimension; 2) the micro-holes are asymmetrical positioned a few μm away from the core center (being different from that in [8]), which make one side of the fiber core partially exposed to the external medium without seriously damaging the periodical structure of FBG. A broadband light source and an OSA with the resolution of 0.01 nm are used to observe the transmission spectrum during the fabrication.
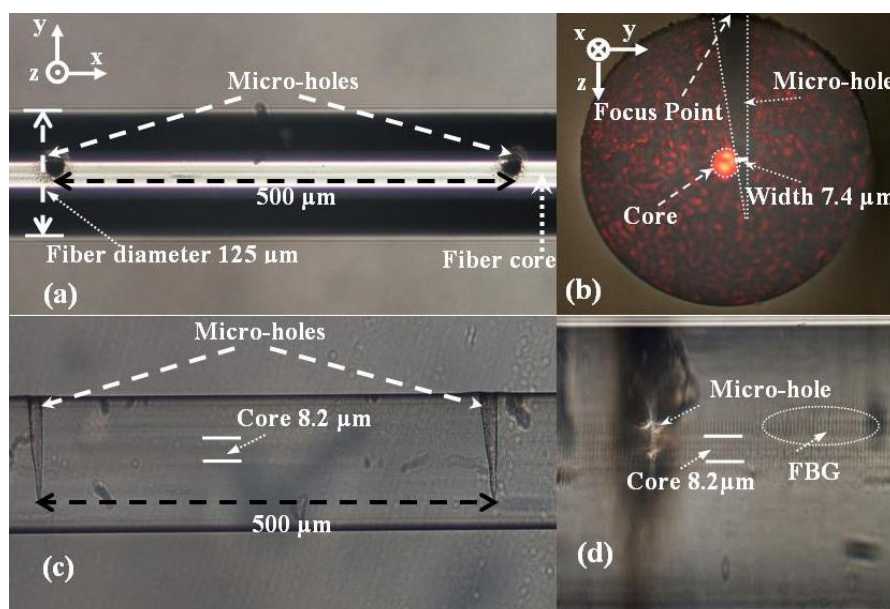
Fig. 5.1 Morphology of the micro-holes embedded FBG in (a) top view (focused at the cladding surface) (b) cross section view (c) side view (d) top view (focused at the fiber core).

Fig. 5.1 shows the morphology of the micro-holes embedded FBG in different views. It can be seen from Fig. 5.1 (d) that the periodical structure of FBG almost remains unaffected. According to Fig. 5.1 (b), the diameter of the micro-hole near the fiber core is estimated to be ~7.4 μm and the depth of the micro-hole is estimated to be ~80 μm.

5.2 Individual RI and Temperature Sensing

Two samples (noted as S1 and S2) with 8 micro-holes are fabricated to reveal that different FBG with similar micro-hole structure and micro-hole number exhibit similar transmission loss and hence similar RI sensitivity. Fig. 5.2 (a) and Fig. 5.2 (b) show the transmission spectra of the initial FBG and the FBG with micro-holes for S1 and S2. The initial transmission spectra (when no micro-hole is drilled) of S1 and S2 have a pristine insertion loss of about 1 and 2.5 dB out of the resonant band, which are the insertion loss of the FBG themselves. After fabrication, the corresponding insertion losses induced by the micro-holes are 6.94 dB and 7.30 dB, respectively, which are close to each other.
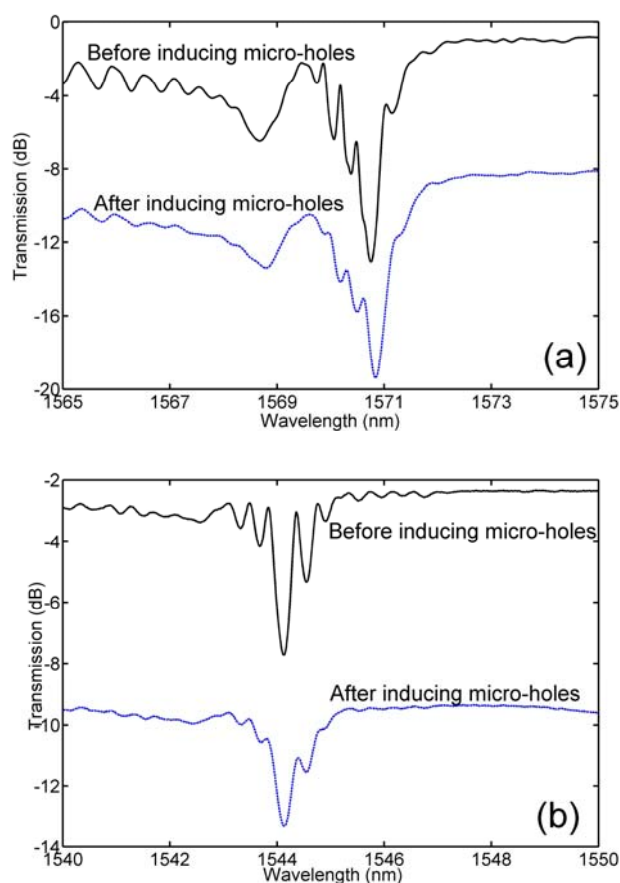
Fig. 5.2 Transmission spectra of initial FBG and FBG with micro-holes: (a) S1 (b) S2.

In the initial transmission spectra of both S1 and S2, sidelobes exist around the main Bragg peak. These peaks may result from the coactions of the following

reasons: (1) During the FBG fabrication, the fiber may have a slight vibration, which generates small non-uniformity in the grating structure; (2) The forward core mode may couple to the backward higher order cladding mode, which results in the resonant dips with small depth in the shorter wavelength region close to the main Bragg peak; (3) The FBG may have apodization at the two ends and small internal defects, which results in multiple reflection of light.

In-situ RI measurement is carried out by immersing the FBG with micro-holes into different RI liquids in the range of 1.30-1.45. Fig. 5.3 (a) shows the responses of the two samples to the external RI change, where the intensity is measured at the FBG resonant dip, λ_B. For S1, the linear fitted RI sensitivity was 29.5 dB/RIU in the range between 1.300 and 1.450, with a linear regression value of R=0.9981. For S2, the linear fitted RI sensitivity is 33.7 dB/RIU in the range between 1.300 and 1.395, with R=0.9986. Both the samples exhibit a similar RI sensitivity and the linear regression value, which ensure a good linearity that can be used in practical applications. Both resonant dips do not shift with the increase of external RI (S1 remains at 1570.85 nm and S2 at 1544.14 nm), owing to the fact that only a small portion of fiber core is actually exposed to the external environment. This means that light energy is mainly bounded inside the fiber core and thus the effective RI of core mode changes little with variation of external RI. Fig. 5.3 (b) shows the transmission spectra of S1 in different RI liquids, and no shift of dip wavelength λ_B is observed.
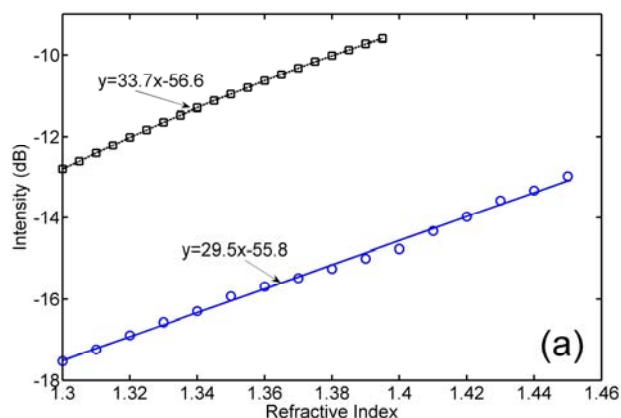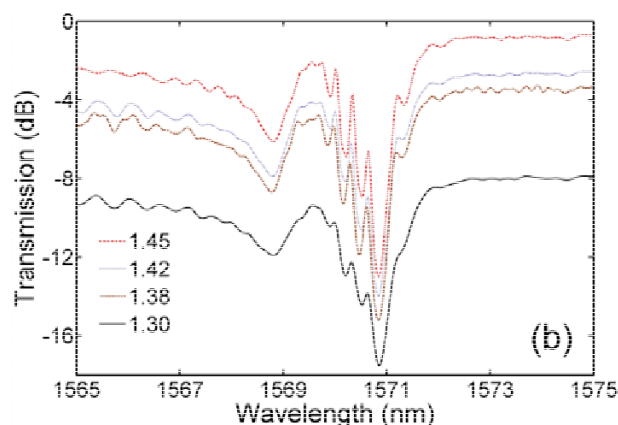
Fig. 5.3 Individual RI measurement (a) FBG resonant dip intensity versus RI (circles: S1; squares: S2) (b) selected transmission spectra of S1 in different RI liquids.

Individual temperature measurement is performed by placing S1 in an column oven (type LCO102), exposed to air, and detecting the shift of λ_B when temperature is gradually increased from 20 to 90 ℃. The result obtained is shown in Fig. 5.4, with the sensitivity of 10.7 pm/℃.
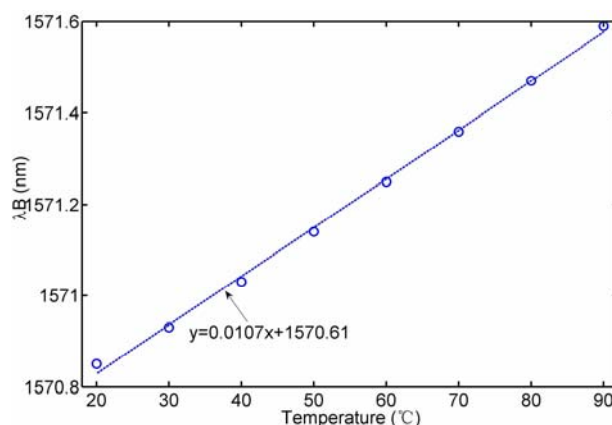
Fig. 5.4 Individual temperature measurement: FBG resonant wavelength of S1 versus temperature (circles: experiment results; line: linear fitted).

5.3   Simultaneous RI and Temperature Sensing

The simultaneous RI and temperature measurement is carried out, by immersing S1 in a RI liquid with value of 1.340 (at 25 ℃, with a temperature coefficient of -0.000338 /℃), which is close to the RI of water. The temperature variation range was chosen as 20-80 ℃, in which the RI liquid could stand without obvious evaporation. When the sensor was immersed into the RI liquid, the rise

of temperature led to the reduction of the RI of the liquid and thus the resonant dip intensity would also decrease. Fig. 5.5 (a) shows the resonant dip intensity I_0 versus external RI change induced by the temperature. The measured RI is determined by I_0 value and the linear fitted results in Fig. 5.3 (a). The temperature induced measurement error and the temperature-RI cross sensitivity are calculated as follows. The RI of liquid is firstly determined at different temperatures according to its temperature coefficient, noted as the calculated RI in Fig. 5.5 (a). Then we can find the corresponding intensity I_1 (according to the calculated RI) by the linear fitted results obtained in Fig. 5.3 (a), noted as the calculated intensity in the inset of Fig. 5.5 (a). The measurement error is then the difference between I_1 and I_0 in the inset of Fig. 5.5 (a). The maximum error obtained is 0.06 dB at 70 ℃, which results in the maximum RI measuring error of 0.002. The error may come from the intensity fluctuation of the light source and the fact that the RI liquid may not keep the same temperature coefficient over the entire temperature range. The temperature induced wavelength shift of λ_B is shown in Fig. 5.5 (b), where the sensitivity obtained is 10.6 pm/℃, almost the same as that in Fig. 5.4, close to the typical value of type-II FBG [21], showing a stable thermal property of the device, not affected by external RI.
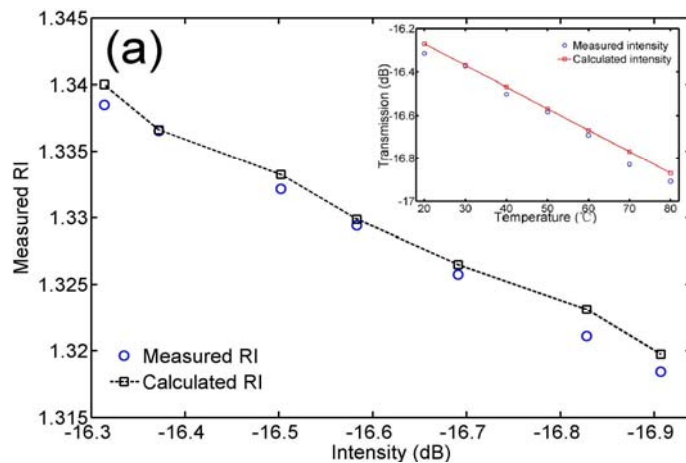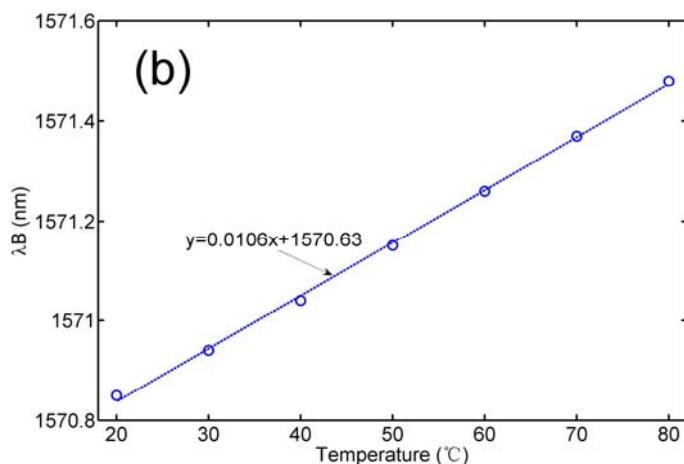
Fig. 5.5 Simultaneous RI and temperature measurement of S1 (a) FBG resonant wavelength intensity versus RI (circles: measured RI, squares with line: calculated RI of liquid at different temperatures), inset: FBG resonant wavelength intensity variation with temperature in the RI liquid (circles: measured intensity I_0; line: calculated intensity I_1) (b) FBG resonant wavelength shift versus temperature (circles: experiment; line: linear fitted).

5.4 Discussion

In order to check the mechanical strength of the FBG with micro-holes, a sample with 8 micro-holes (with total fiber length of 24 cm) is measured with the failure strain of 0.2%. Suppose glass fiber has a Young's modulus of 70 GPa, this failure strain corresponds to a failure stress of 0.14 GPa (or failure tension of 1.72 N if the fiber radius is 62.5 μm), which can be considered as a high loading [22]. Another sample could be bent to a curvature radius of ~1.5 cm before being broken. In RI and temperature experiments, the samples used are not too fragile to be easily broken. Of course, proper care still needs to be taken.

Normally, the more micro-hole number, the larger micro-hole size and the smaller deviation position from the core center, the larger the insertion loss and hence the greater the RI sensitivity. Compared with the two samples, S1 has a smaller micro-hole induced insertion loss and thus a smaller RI sensitivity. This difference may result from the geometry error during the fabrication process.

An irregular wavelength dependent transmission loss exists in Fig. 5.3 (b),

which means that the RI responses of transmission loss are not the same at different wavelengths. This may result from: (1) the periodical asymmetrically located micro-holes can induce the LPFG effect as discussed in section 4.3, which results in small irregular transmission dips when phase matching condition is met; (2) each micro-hole can be seen as an MZI with small fringe visibility and extreme large FSR, as discussed in section 3.3, and the a number of cascaded holes can enhance the interference effect [23].

5.5 Summary

In this chapter, FBG with asymmetrically located micro-holes embedded sensor is fabricated by use of fs irradiation. By direct detection of the FBG resonant wavelength shift and its intensity variation, a simultaneous and independent temperature and RI sensing can be achieved. The two parameters can be determined by tracing only one characteristic wavelength, which is convenient for practical system operation. The RI sensitivity obtained is ~29.5 dB/RIU in the RI region 1.300-1.450, with a good linearity, which can be further increased by increasing the number of micro-holes.

References for Chapter 5

1. X. Shu, B. A. L. Gwandu, Y. Liu, et al, "Sampled fiber Bragg grating for simultaneous refractive-index and temperature measurement," Opt. Lett. **26**, 774-776 (2001).

2. X. Chen, K. Zhou, L. Zhang, et al, "Simultaneous measurement of temperature and external refractive index by use of a hybrid grating in D fiber with enhanced sensitivity by HF etching," Appl. Opt. **44**, 178-182 (2005).

3. T. Allsop, R. Neal, D. Giannone, et al, "Sensing characteristics of a novel two-section long-period grating," Appl. Opt. **42**, 3766-3771 (2003).

4. A. P. Zhang, L. Y. Shao, J. F. Ding, et al, "Sandwiched Long-Period Gratings

for Simultaneous Measurement of Refractive Index and Temperature," IEEE Photon. Technol. Lett. **17**, 2397–2399 (2005).

5. C. L. Zhao, X. Yang, M. S. Demokan, et al, "Simultaneous Temperature and Refractive Index Measurements Using a 3∘ Slanted Multimode Fiber Bragg Grating," J. Lightwave Technol. **24**, 879-883 (2006).

6. K. Zhou, L. Zhang, X. Chen, et al, "Optic sensors of high refractive-index responsivity and low thermal cross sensitivity that use fiber Bragg gratings of >80° tilted structures," Opt. Lett. **31**, 1193-1195 (2006).

7. D. W. Kim, F. Shen, X. Chen, et al, "Simultaneous measurement of refractive index and temperature based on a reflection-mode long-period grating and an intrinsic Fabry–Perot interferometer sensor," Opt. Lett. **30**, 3000-3002 (2005).

8. K. Zhou, X. Chen, L. Zhang, et al, "Implementation of optical chemsensors based on HF-etched fibre Bragg grating structures," Meas. Sci. Technol. **17**, 1140-1145 (2006).

9. O. Frazão, B.V. Marques, P. Jorge, "High birefringence D-type fibre loop mirror used as refractometer," Sensors and Actuators B: Chemical **135**, 108-111 (2008).

10. L. Y. Shao, A. P. Zhang, W. S. Liu, et al, "Optical refractive index sensor based on dual fiber-Bragg gratings interposed with a multimode-fiber taper," IEEE Photon. Technol. Lett. **19**, 30–32 (2007).

11. L. Q. Men, P. Lu, Q. Y. Chen, "A multiplexed fiber Bragg grating sensor for simultaneous salinity and temperature measurement," J. Appl. Phys. **103**, 053107, (2008).

12. P. Lu, L. Men, K. Sooley, and Q. Chen, "Tapered fiber Mach–Zehnder interferometer for simultaneous measurement of refractive index and temperature," Appl. Phys. Lett. **94**, 131110 (2009).

13. H. Liu, F. Pang, H. Guo, et al, "In-series double cladding fibers for simultaneous refractive index and temperature measurement," Opt. Express **18**, 13072-13082 (2010).

14. T. Wei, Y. Han, Y. Li, et al, "Temperature-insensitive miniaturized fiber inline Fabry-Perot interferometer for highly sensitive refractive index measurement," Opt. Express **16**, 5764-5769 (2008).

15. K. Zhou, Y. Lai, X. Chen, et al, "A refractometer based on a micro-slot in a fiber Bragg grating formed by chemically assisted femtosecond laser processing," Opt. Express **15**, 15848-15853 (2007).

16. H. Fu, K. Zhou, P. Saffari, et al, "Microchanneled chirped fiber Bragg grating formed by femtosecond laser-aided chemical etching for refractive index and temperature measurements," IEEE Photon. Technol. Lett. **20**, 1609-1611 (2008).

17. C. Mou, K. Zhou, E. Davies, et al, "Fiber laser incorporating an intracavity microchannel for refractive index and temperature sensing," IEEE Photon. Technol. Lett. **21**, 1559-1561 (2009).

18. C. R. Liao, Y. Wang, D. N. Wang, et al, "Fiber In-Line Mach–Zehnder Interferometer Embedded in FBG for Simultaneous Refractive Index and Temperature Measurement," IEEE Photon. Technol. Lett. **22**, 1686-1688 (2010).

19. Y. Li, C. R. Liao, D. N. Wang, et al, "Study of spectral and annealing properties of fiber Bragg gratings written in H_2-free and H_2-loaded fibers by use of femtosecond laser pulses," Opt. Express **16**, 21239-21247 (2008).

20. C. W. Smelser, S. J. Mihailov, D. Grobnic, "Formation of Type I-IR and Type II-IR gratings with an ultrafast IR laser and a phase mask," Opt. Express **13**, 5377-5386 (2005).

21. C. Liao, D. N. Wang, Y. Li, et al, "Temporal thermal response of Type II–IR fiber Bragg gratings," Appl. Opt. **48**, 3001-3007 (2009).

22. B. H. Kim, Y. Park, T.-J. Ahn, et al, "Residual stress relaxation in the core of optical fiber by CO_2 laser irradiation," Opt. Lett. **26**, 1657-1659 (2001).

23. Y. Wang, H. Zhu, B. Li, "Cascaded Mach–Zehnder interferometers assembled by submicrometer PTT wires," IEEE Photon. Technol. Lett. **21**, 1115-1117 (2009).

Chapter 6 Fs Laser Assisted Selective Infiltration Technique

The work of this thesis by now is achieved by only one fundamental application of fs micro-machining: either local irradiation or line scanning. And the micro-structures remain in the fabricated devices. In this chapter, by use of fs laser assisted micro-machining, a selective infiltration of any air hole(s) of the PCF is achieved in a convenient and flexible way. This technique applies both the two basic ways, with several key problems taken into consideration, such as the focusing beam geometry, the energy control and the focus point location, which is an example for complicate fs laser micro-machining. Two devices based on this technique, including a directional coupler and a two mode interferometer are developed, which can be used for RI or temperature sensor with relatively high sensitivity. The theoretical analysis on mode properties of the two devices is presented by use of FEM simulation, and their sensitivities are also simulated, which agree well with the experiment results obtained. No micro-structure is left in the two devices, which broadens the application of fs laser micro-machining in fabricating novel OFS.

6.1   Fs Laser Assisted Selective Infiltration

PCF is a type of micro-structured optical fiber (MOF) that contains a solid fiber core, which is surrounded by periodical arrays of air holes in the fiber cladding. Compared with normal SMF, PCF possesses many interesting modal and dispersion properties and in addition, the air holes around the solid core make it a potential platform for RI sensing. An elegant way is to infiltrate liquid analyte with higher RI value than that of the background silica into certain air hole(s) of the PCF [1], which strongly changes the guidance property depending on the RI of the analyte. A commonly used way is to block the air holes not to be

infiltrated while leave the other air holes open for infiltration [2]. The presented techniques include air holes collapsing [3, 4], injection-cure-cleaving [5], splicing MOF with a single-hole hollow-core fiber [6, 7], lateral access to the air holes [8, 9] and direct manual gluing [1, 2, 10]. Overall, these methods have the difficulties in flexibly and efficiently filling of any groups of air hole(s) with similar air hole size in the cladding region. Besides, the steps are usually complicated and inconvenient.

Compared with the previously reported ones, the fs laser assisted selective infiltration technique developed here has certain advantages of excellent flexibility and reliability, which is easily achieved. This technique includes the following steps [11]: (1) a section of PCF is fusion spliced with normal SMF to block all the air holes, (2) the SMF is then cut off at the position close to the splice point by use of fs laser scanning and (3) the desired air holes are then drilled full through from the cutting end of the SMF to the splice point by fs laser so as to selectively infiltrate liquid into the PCF. In this chapter, the PCF used is a commercialized LMA-10 type solid core PCF from NKT Photonics, with 60 holes periodically locates in the fiber cross section. The air hole diameter is 3.04 μm and the hole-to–hole pitch is 6.26 μm, as shown in Fig. 6.1.
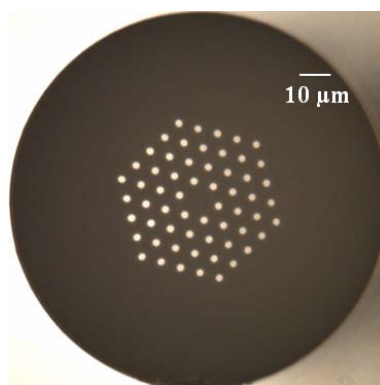

Fig. 6.1 Cross section of LMA-10 PCF from NKT Photonics.

6.1.1 Fs Laser Cleaving

The sample of PCF spliced with SMF is mounted on the 3D translation stage. The cleaving position is chosen to be ~10 μm away from the splicing point. This parameter is optimized due to the following principles:

(1) For a more accurate location of the laser focus point when drilling micro-hole afterwards, one would wish to use the MO with a larger magnification. According to the discussion in Chapter 2, the larger the magnification of the MO, the larger the NA (and the smaller the focused beam waist), and thus the smaller the Rayleigh length (or the micro-hole depth that can be drilled). Therefore, if the cleaving position is too far away from the splicing point, the remaining SMF may not be easily drilled fully through. Besides, the SMF layer that is too thick may result in difficulty of locating the desired air hole for selective infiltration.

(2) On the other hand, the cleaving position cannot be chosen to be too close to the splicing point so as to protect the splicing point stay unaffected from the fs laser beam waist width during the scanning process. Since the micro-hole drilled by fs laser is a cone structure as mentioned in Chapter 3, a certain thickness of the SMF layer may help to prevent infiltration of unwanted air hole in PCF when the cone angle of the micro-hole drilled afterwards is large.

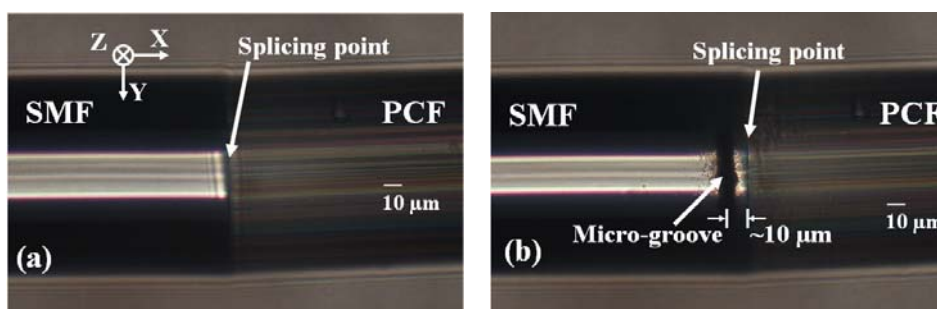Fig. 6.2 Fs laser cleaving (a) scanning direction (b) micro-groove made by scanning.

After the laser focus point is located at the desired position, the fs laser is then scanning along the transverse y-direction along the SMF at the cladding surface, as shown in Fig. 6.2 (a). The magnification of the MO is 20×, with its NA of 0.50. The fs laser scans across the SMF for 2~3 times, with a single pulse

energy of 5 μJ and a scanning speed of 50 μm/s. These parameters are chosen so as to make the cleaving surface as smooth as possible while leaves a thin SMF layer to still block the air holes and protect the splicing point without damaging. The fs laser scanning process will leave a micro-groove across the SMF, which generates a local stress concentration to break the redundant SMF away easily. The micro-groove is shown in Fig. 6.2 (b).

6.1.2 Selective Opening of Air Hole(s)

After the fs laser cleaving process, selective opening of air hole(s) is performed by fs drilling of micro-hole(s) directly on the cleaving surface. The sample is put perpendicularly. To ensure an accurate locating of focus point, the MO with its magnification of 60× and NA value of 0.85 is chosen. The laser focus point is first located at the plane of splicing point, which makes the air holes of PCF clearly seen, as shown in Fig. 6.3 (a). Then, the desired air hole for selective opening is targeted. Finally, the focus point is moved to the cleaving surface, which makes the remaining SMF layer clearly seen while the air holes blur as shown in Fig. 6.3 (b).
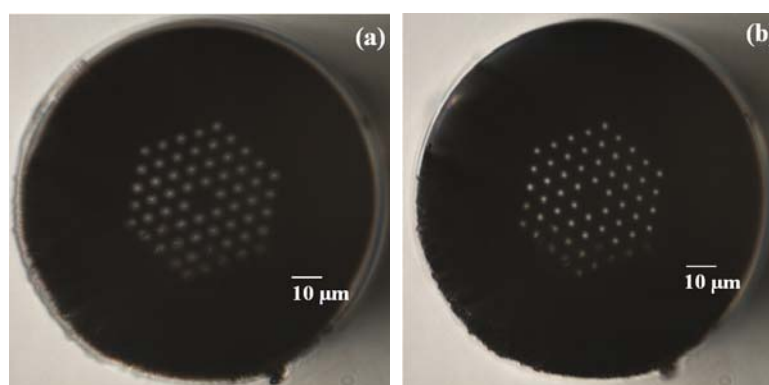
Fig. 6.3 Focus point locating at (a) plane of splicing point (b) cleaving surface.

The drilling parameters are selected to be 3 μJ for the single pulse energy and ~40 s for the irradiation time of one micro-hole, so as to ensure (1) a through micro-hole from the cleaving surface to the desired air hole of PCF for infiltration, and (2) no connection between the drilled micro-hole and any other

undesired air hole(s) of PCF. The drilled micro-hole is shown in Fig. 6.4.
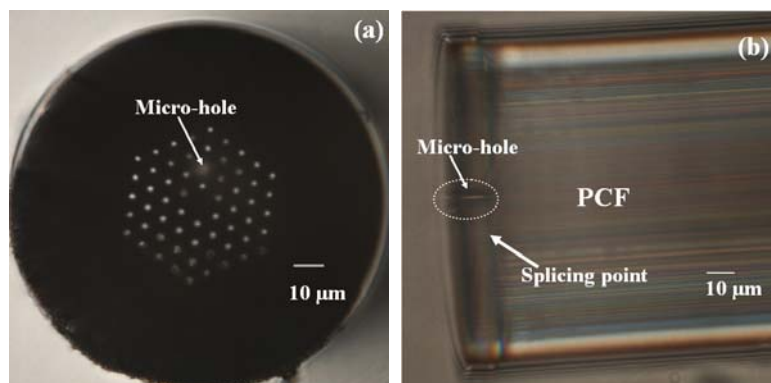
Fig. 6.4 Micro-hole drilled in (a) top view at the plane of cleaving surface (b) side view.

6.1.3 Infiltration of Liquid

After the desired air holes are opened, the sample is then immersed in liquid analyte to be infiltrated according to the well-known capillary effect. The infiltration speed depends on the air hole size of the PCF, the viscosity and the surface tension of the infiltrating liquid [2]. In order to obtain a PCF with liquid infiltrated length as long as possible, the non-immersed PCF end should be left open without fusion splicing and the infiltration time needs to be as long as possible. After infiltration, the SMF section is cleaved to observe the infiltration results of the remaining PCF. One example is shown in Fig. 6.5, with the infiltrated air-holes easily distinguished from the others.
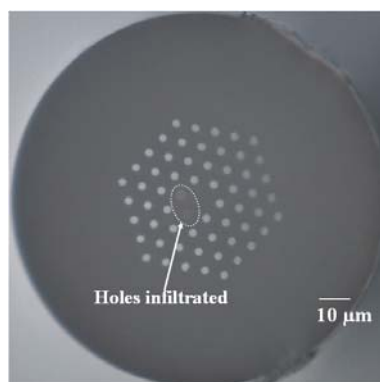
Fig. 6.5 Example of infiltration result.

6.2   Modes Coupling Resonant Sensor

By infiltrating high RI analyte into one air hole located at the second innermost layer of the PCF, a directional coupler device can be fabricated. The high RI analyte rod is a waveguide itself, which can support waveguide rod modes beyond cutoff. Mode coupling can occur between the PCF fundamental core mode and the fundamental or certain higher order mode of the high RI rod according to the phase matching condition between the two modes. The phase matching point is close to the cutoff point of the rod mode in wavelength, which results in a sharp deep transmission dip in the spectrum. The phase matching point is highly sensitive to the RI of the high analyte in the air hole.

6.2.1 Modes of High RI Rod

PCF is known to confine light in the solid core by total internal reflection (or called RI guiding) [12]. The effective RI of the PCF fundamental core mode (core LP_{01} mode) $n_{eff, core}$ is slightly smaller than that of the background silica n_{bg}. When high RI analyte is infiltrated into one air hole of the PCF, it forms a waveguide (high RI rod) and can support different order waveguide rod mode with effective RI $n_{eff, wg}$ higher than n_{bg}. Normally, the fundamental rod mode (rod LP_{01} mode) has its $n_{eff, wg} > n_{eff, core}$, which means phase matching between the core LP_{01} mode and the rod LP_{01} mode is impossible and no modes coupling occurs. When $n_{eff, wg} > n_{bg}$, the mode field of rod LP_{01} mode is confined in the high RI rod and is therefore called a bound mode. However, the rod mode may reach cutoff due to the waveguide dispersion or decrease in the rod RI, whereas $n_{eff, wg} < n_{bg}$. Its mode field is then no longer confined by the high RI rod but distributed in the silica region between air holes and is therefore called a leaky mode. The critical wavelength when rod mode reaches cutoff is noted as the modal cutoff wavelength λ_c [1, 2]. Fig. 6.6 shows mode field profile of the core LP_{01} mode, the rod LP_{01} mode before and after cutoff, by use of FEM simulation

(the black circles indicate the air holes of PCF and only the region near the mode field is shown for simplicity).
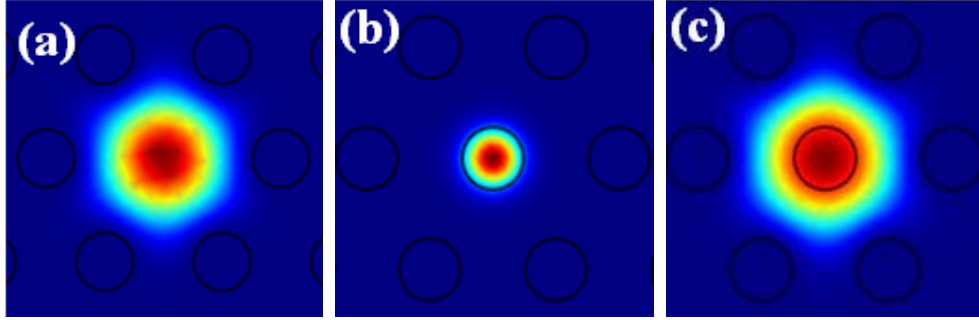
Fig. 6.6 Mode field simulation of (a) core LP_{01} mode (b) rod LP_{01} mode before cutoff (c) rod LP_{01} mode after cutoff.

6.2.2 RI Sensitivity

During the transition region around the cutoff point of the rod mode, there is a wavelength point when $n_{eff, wg}=n_{eff, core}$, which satisfies the phase matching condition and mode coupling occurs from the core mode to the rod mode. This wavelength point is very close to λ_c, and is extremely sensitive to the RI of the high RI rod. The RI sensitivity S can be calculated according to the following equations [1, 2]:

$$\lambda_c = \frac{2\pi\rho}{V_c}\sqrt{n_{high}^2 - n_{bg}^2} \tag{6.1}$$

$$S = \frac{\partial \lambda_c}{\partial n_{high}} = \frac{\lambda_c n_{high}}{n_{high}^2 - n_{bg}^2} \tag{6.2}$$

where ρ is the radius of the high RI rod, n_{high} is the RI of the high RI analyte, $V_c \in \{2.405, 3.832, \ldots\}$ is the normalized cutoff frequency corresponding to different order of rod mode (the values in the set equal to the first root of Bessel function with different order, which correspond to rod modes of different order). It can be seen that the RI sensitivity reaches maximum when $n_{high} = n_{bg}$.

6.2.3 Temperature Sensor Based on Mode Coupling

In order to get a strong coupling and thus a deep transmission dip at cutoff wavelength, liquid with RI slightly higher than the background silica is infiltrated into the second innermost layer of LMA-10 PCF. There are 12 air-holes in this layer, which can be divided into 2 groups, according to the distance between the air hole center to the fiber core center, noted as type-A and type-B [11], as shown in Fig. 6.7.
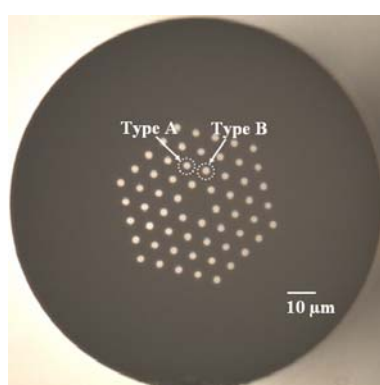
Fig. 6.7 Two types of air holes in the second innermost layer of LMA-10 PCF.

For a prototype, one of the type-A holes is infiltrated of liquid with RI=1.46 (@ 589.3nm, 25 ℃, the temperature coefficient is -3.89×10^{-4} RIU/℃). Fig. 6.8 demonstrates the fiber geometry after the selective infiltration process. In the experiment, the liquid filled PCF sample used is 2.4 cm in length.
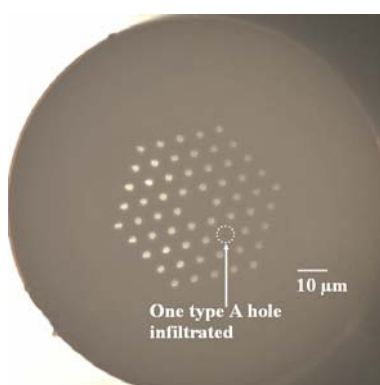
Fig. 6.8 Selective infiltration of one type-A hole of LMA-10 PCF.

In the room temperature, there are no apparent transmission dips in the wavelength range between 1500-1600 nm, which may due to the fact that the

effective RI of rod LP_{01} mode is always larger than that of the core LP_{01} mode. However, when the sample is heated to 34 ℃ (the type LCO102 column oven has a display temperature accuracy of 0.1 ℃ and is enclosed to diminish the air quenching induced temperature variance), apparent transmission dip appears. The transmission spectra corresponding to the temperature range between 34.0 and 35.4 ℃ are recorded in Fig. 6.9 (a). At each temperature, the sample stayed for 30 minutes before measuring the transmission spectrum so as to make the temperature as stable as possible. And the dip wavelength variation with the temperature is plotted in Fig. 6.9 (b), which appears to be a linear temperature response, with an averaged temperature sensitivity of 54.3 nm/℃ obtained in the region between 1500-1600 nm. The dip wavelength is red-shifted with the increase of temperature.
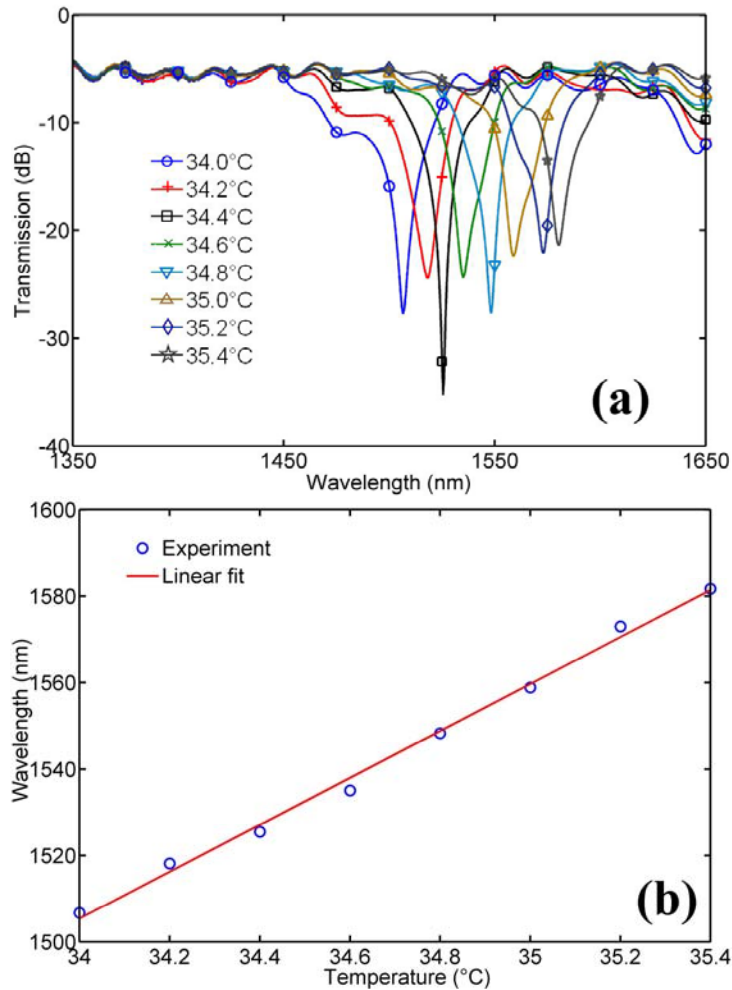
Fig. 6.9 Temperature response of the sample (a) transmission spectra (b) shift of transmission dip.

The modes involved in the coupling are the core LP_{01} mode and the rod LP_{01} mode because of the close value of silica and the liquid analyte when heating to 34 ℃ and thus the similar dispersion properties of the two modes. To confirm the coupling mechanism and the temperature sensitivity theoretically, the liquid sample is modeled with the geometrical parameters aforementioned. The modal dispersion properties are calculated numerically by use of FEM simulation. The material dispersions of both silica [13] and RI liquid (with a Cauchy approximation formula of $n(\lambda) = a + \dfrac{b}{\lambda^2} + \dfrac{c}{\lambda^4}$ [14]) are taken into account, as listed in Table 6.1.

Table 6.1 Calculated material dispersion of 1.46 RI liquid and silica.

Wavelength (nm)	RI of 1.46 liquid	RI of Silica
800	1.45466	1.45356
900	1.45337	1.45200
1000	1.45247	1.45066
1100	1.45180	1.44945
1200	1.45130	1.44830
1300	1.45091	1.44717
1400	1.45061	1.44603
1500	1.45036	1.44487
1600	1.45016	1.44367

The simulated mode field profiles of the core LP_{01} mode and the rod LP_{01} mode are shown in Fig. 6.10 (a) and 10(b), respectively. There are no interactions between the two modes in the wavelength region between 800-1600 nm, when liquid is in room temperature. The rod LP_{01} mode is more temperature sensitive than that of the core LP_{01} mode, due to a much larger temperature coefficient of the liquid than that of silica. Therefore, the effective RI of rod LP_{01} mode decreases more significantly than that of the core LP_{01} mode and results in interaction of the two dispersion curves. Fig. 6.10 (c) presents the mode profile at the resonant wavelength, which means that light coupling occurs between the fiber core and the high RI rod. The dispersion curves of the core LP_{01} and rod LP_{01} modes at different temperatures (30 and 35 ℃) are shown in Fig. 6.10 (d). The effective RI change of the core LP_{01} mode introduced by the 5 ℃

temperature increment is too small to be observed in the figure.
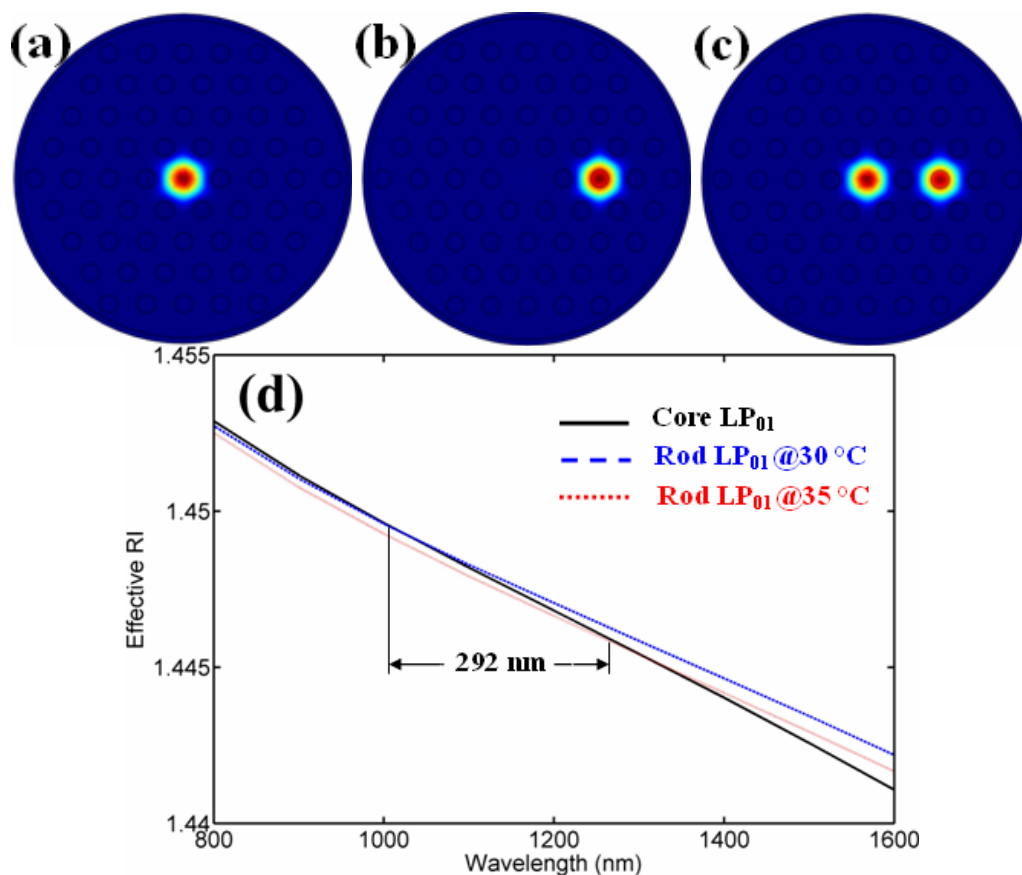
Fig. 6.10 FEM simulation of (a) mode field of core LP_{01} mode (b) mode field of rod LP_{01} mode (c) mode field of the two modes at resonant wavelength (d) dispersion curves of the two modes.

The region between the two crossing points of the core LP_{01} and the rod LP_{01} dispersion curves determines the coupling wavelength region in the transmission spectra of Fig. 6.9 (a). With the increase of temperature of the sample, the effective RI of the rod LP_{01} mode decreases and hence results in a dramatic red shift of the resonant wavelength, due to the very close dispersion properties of the two modes. The simulated resonant wavelength shifts for ~292 nm from 1012 nm at 30 ℃ to 1304 nm at 35 ℃, representing an averaged temperature sensitivity of ~58.4 nm/℃. The exact discrepancy between the numerical results and the experiment data of the exact resonant wavelength is possibly caused by the geometry deviation of the simulation model from the virtual PCF sample.

6.3   MZI Based Temperature Sensor

Being different from the directional mode coupling device developed in section 6.2, in this section, a novel kind of fiber-inline MZI is developed by selective infiltration of two adjacent air holes in the innermost layer of the LMA-10 PCF. The interaction between the higher order modes of the two high analyte rod can support a hybrid mode, which can interfere with the core LP_{01} mode and leave interference fringe in the transmission spectrum. When properly chosen the RI of analyte, the FSR can be clearly identified. This device can also be applied as a temperature sensor with a high temperature sensitivity. The modes involved in interference and temperature sensitivity of the MZI device is also simulated by FEM and compared with the experiment.

6.3.1 Device Performance

In this section, liquid with RI=1.47 (@589.3 nm, 25 ℃, the temperature coefficient is -3.92×10^{-4} RIU/℃) is infiltrated into two adjacent air holes in the innermost layer of the LMA-10 PCF. The motivation for infiltrating two air holes here is to generate a stable guide mode with smaller attenuation than the leaky mode generated by infiltrating only one air hole. On the other hand, if more than two holes are infiltrated, more rod modes and hybrid modes may be generated, which may make the interference fringe pattern complicate and not convenient for sensing application. The infiltration result is shown in Fig. 6.11.
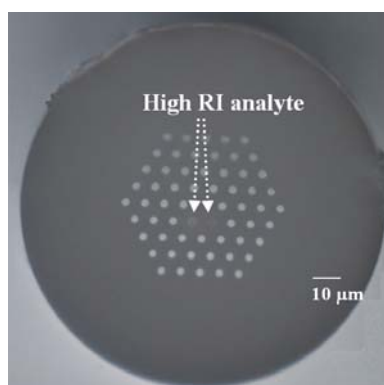

Fig. 6.11 Selective infiltration of two adjacent air holes.

After the infiltration is completed, the sample is cut back from the non-immersed fiber end and observed the result with the help of a microscope, until all the remaining PCF to be used is fully filled of liquid. The initial infiltrated PCF length is approximately 8.2 cm. Such a sample is then spliced with SMF on both ends and its transmission spectrum is measured. After each measurement, the sample is cut back again to allow measuring the transmission spectrum of the device with a different PCF length, as shown in Fig. 6.12. It can be clearly seen that interference fringe pattern exists in each transmission spectrum and the FSR of the fringe pattern increases with the decrease of PCF length. The FSR around 1550 nm is 8.7, 16.7, 24.2, and 40.2 nm for the PCF length of 8.2, 5.2, 3.4, and 1.8 cm, respectively. The relatively large insertion loss corresponding to the device length of 8.2 cm may be created in the splicing process.
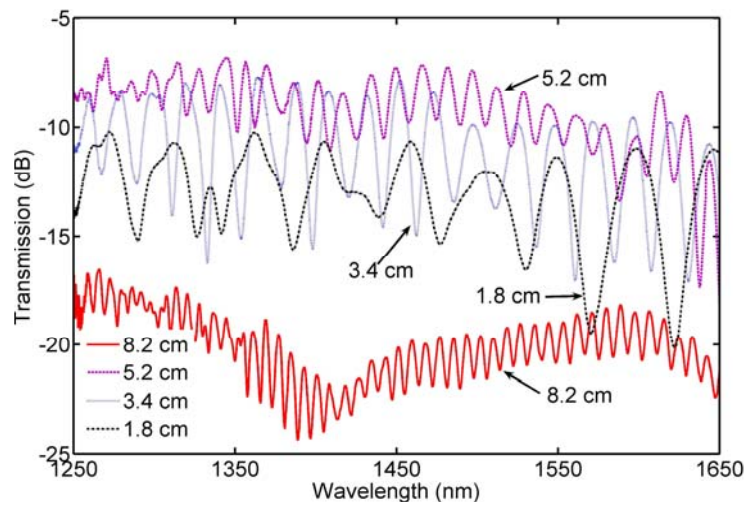
Fig. 6.12 Transmission spectra of the sample with different PCF lengths.

According to Eq. (3.3), the effective RI difference Δn_{eff} of the two modes involved in interference can be calculated as 3.4×10^{-3}, 2.8×10^{-3}, 3.0×10^{-3} and 3.4×10^{-3}, for the different PCF length respectively. The difference in the calculated Δn_{eff} values may result from the measurement error of the device length. In Fig. 6.12, apart from the main fringe structure, a slowly varying envelope can also be found. This may due to the interference between the polarization modes, which has a much smaller Δn_{eff} and hence a larger FSR than

that of the main fringe. However, when the device length is reduced, the visibility of the main fringe pattern increases and the slowly varying envelope has little effect on the transmission spectrum.

6.3.2 Simulation of Modes Involved in Interference

In order to identify the modes involved in the main interference fringe pattern, the first four modes (each is two-folder degenerated) with the largest effective RI values are simulated by FEM, as shown in Fig. 6.13. For the sake of simplicity, only one polarization state is plotted. The arrows in Fig. 6.13 stand for both the amplitude and the direction of the mode electric field. The modes in Figs. 6.13 (a) and 3(b) are the bound modes of the high RI rods, but with different electric field directions of the two rod LP_{01} modes: the modes in Fig. 6.13 (a) have the same electric field direction, while in Fig. 6.13 (b), the directions of the two rod LP_{01} modes are opposite. Such a difference in electric field direction results in a difference in effective RI, as well as in intermodal coupling. Mode in Fig. 6.13 (c) is the PCF core LP_{01} mode and mode in Fig. 6.13 (d) is denoted as the hybrid mode confined by the two high RI analyte rods.
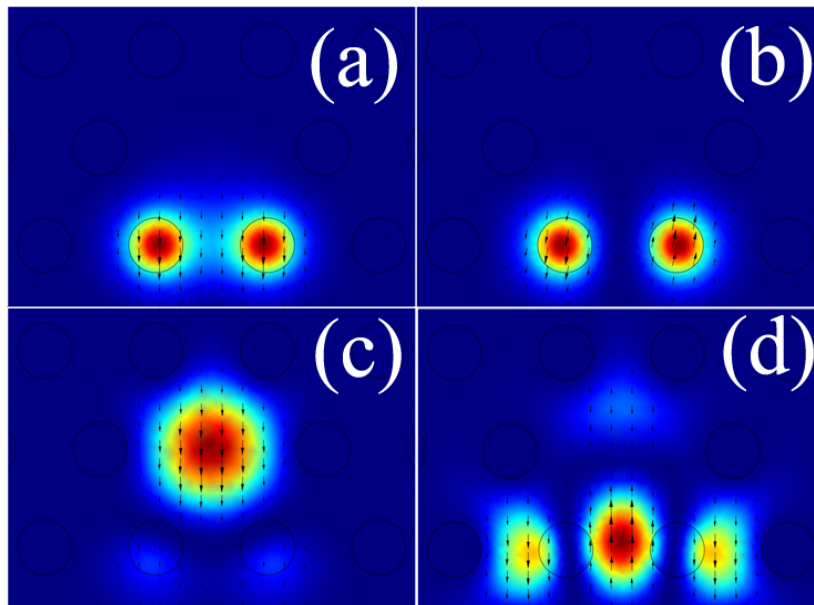
Fig. 6.13 Simulation of the first four mode fields, only the y-polarization state is plotted.

Being different from the real core mode supported by the second fiber core [16-21], the hybrid mode here is actually the overlap of the two LP_{11} higher order rod modes (which is the first higher order mode of the infiltrated holes) of the two high RI rods when they have the same electric field direction. This overlap makes the mode field intensity in the region between the two high rods stronger.

Table 6.2 Calculated material dispersion of 1.47 RI liquid and silica.

Wavelength (nm)	RI of 1.47 liquid	RI of silica
1250	1.45985	1.44773
1300	1.45964	1.44717
1350	1.45945	1.44660
1400	1.45929	1.44603
1450	1.45914	1.44546
1500	1.45900	1.44487
1550	1.45888	1.44428
1600	1.45877	1.44367
1650	1.45867	1.44306
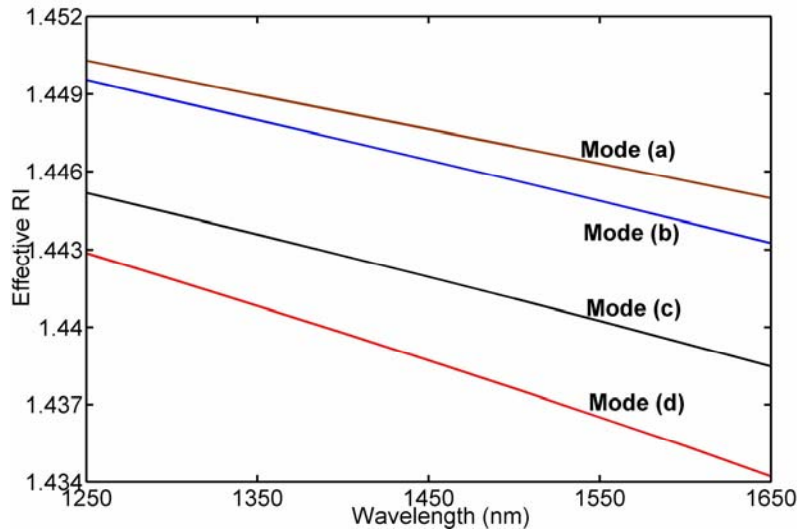
Fig. 6.14 Simulation of the dispersion curves of the four modes in Fig. 6.13 (a)-(d).

The dispersion curves of the modes appear in Fig. 6.13 are also simulated by use of FEM, with material dispersion (shown in Table 6.2) being taken into account, as shown in Fig. 6.14. According to the simulated effective RI values of each mode and the previously calculated Δn_{eff}, the two modes involved in the main interference pattern should be the core LP_{01} mode and the hybrid mode. It is worth noting that the hybrid mode always has a smaller effective RI than that of

the background silica, and thus is confined by the hole–silica structure. This is due to the fact that in the wavelength range between 1250 and 1650 nm, the dispersion curves of the core LP_{01} mode and the hybrid mode do not intersect, and therefore no mode coupling will occur since the phase matching condition cannot be satisfied.

Meanwhile, the birefringence of each mode (which is the difference in effective RI between the x-polarization and the y-polarization state of each mode) is simulated as 1.1×10^{-5}, 5.0×10^{-6}, 7.0×10^{-6}, and 7.7×10^{-5} for the modes of Fig. 6.13 (a)–(d), respectively. The hybrid mode has the largest birefringence, which corresponds to a polarization mode interference with FSR of around 380nm when the device length is 8.2 cm, similar to that obtained by measuring the slowly varying envelope as shown in Fig. 6.12.

6.3.3 Temperature Sensitivity

The selected spectra and the wavelength shifts of the fringe dip corresponding to different PCF lengths in different temperatures are shown in Fig. 6.15, where the temperature sensitivity obtained for the PCF lengths of 1.8 and 3.4 cm is 6.0 and 7.3 nm/℃, respectively. The heating oven is the same as that used in section 6.2. The sensitivity variation may come from the temperature fluctuation during the measurement: because of the high temperature sensitivity, a slight temperature fluctuation results in a large measurement error. Although any wavelength dip (peak) can be traced in the measurement, the fringe dip around 1550nm (the initial fringe dips are 1555.6 and 1534.5nm for the PCF lengths of 3.4 and 1.8 cm, respectively) is chosen, which simplifies the subsequent simulations.
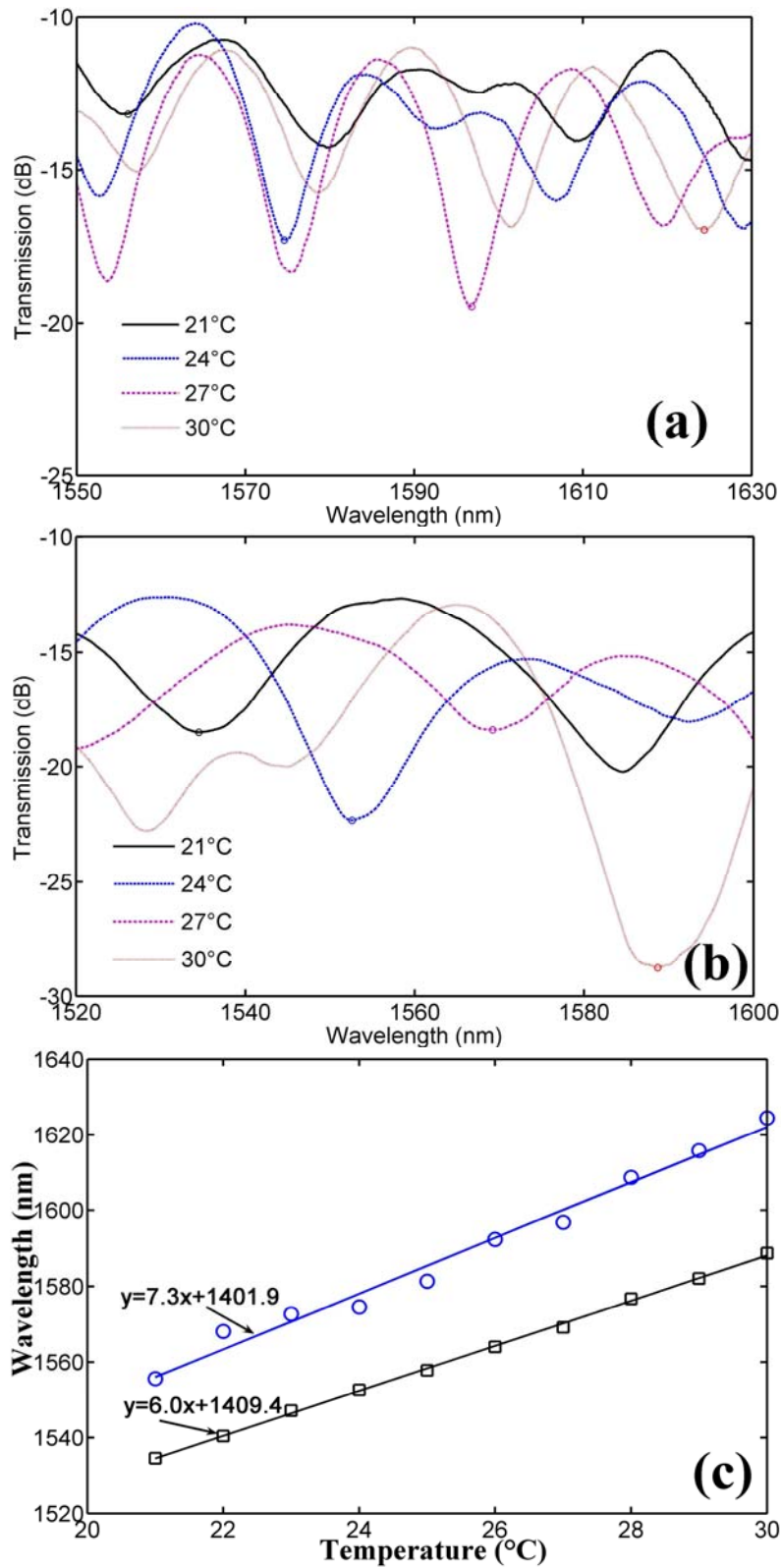
Fig. 6.15 Temperature sensitivity of the interferometer with different PCF lengths (a) selected transmission spectra when PCF length is 3.4 cm, circles: traced fringe dip (b) selected transmission spectra when PCF length is 1.8 cm, circles: traced fringe dip (c) traced fringe dip wavelength shift for different PCF length: circles, 3.4 cm; squares: 1.8 cm; lines: linear fitted.

The temperature sensitivity for a certain fringe dip λ of the MZI is expressed as

Eq. (3.4). Since the liquid high RI analyte usually has a much larger thermo coefficient than that of silica [22], the temperature sensitivity of the device is much larger than that of the conventional temperature sensor device based on changing the RI of silica only. The thermo coefficient of the core LP_{01} mode and the hybrid mode can be simulated through FEM and the results obtained are $-2.0 \times 10^{-6} /℃$ and $-2.1 \times 10^{-5} /℃$, respectively, as shown in Fig. 6.16.
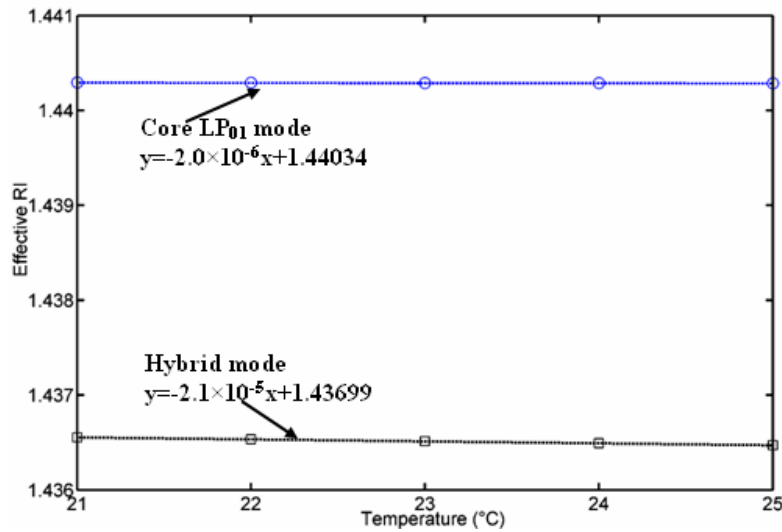
Fig. 6.16 Simulation of the thermo coefficients of the core LP_{01} mode (circles) and the hybrid mode (squares); lines: linear fit of the simulation results.

According to Eq. (3.4), the temperature sensitivity is approximately 7.7 nm/℃, which is reasonably close to the experimental results obtained in Fig. 6.15. The temperature sensitivity obtained from the experiment is much larger than that of the air-cavity-based MZI [15] or a dual-core structured PCF [21]. Moreover, the close values obtained in the experiment and in the simulations also imply that the main interference pattern is most likely produced by the core LP_{01} mode and the hybrid mode generated from the coupling of the two rod LP_{11} modes.

6.4 Summary

In this chapter, the fs laser assisted selective infiltration of air hole(s) in PCF has been developed and applied for fabricating RI or temperature sensors, which includes a series basic operations of fs laser micro-machining. This technique

has shown its advantages of highly flexibility, reliability and accuracy for infiltrating any groups of air hole(s). Two kinds of devices based on this technique are also developed for temperature sensing with high sensitivities. The FEM simulations are performed for the temperature sensitivities and compared with the experiment results. For mode coupling device based on filling of one type-A air hole, the liquid is desired to have a similar RI value to that of silica, and the mode coupling occurs between the core LP_{01} mode and the rod LP_{01} mode, when the dispersion curves of the two modes have interactions. This results in a transmission dip at the resonant wavelength. The temperature sensitivity can be as high as 54.8 nm/℃, with a resonant wavelength region of 292 nm. Another device developed is based on infiltrating of two adjacent air holes with the same RI value, which generates a hybrid mode from the mode coupling of the two rod LP_{11} higher-order modes. This hybrid mode interferes with the core LP_{01} mode, and the sample in this chapter has a temperature sensitivity of ~7 nm/℃. The two devices developed have shown the possibility for other devices developed by infiltrating versatile groups of air holes, and thus enable the fs assisted selective infiltration technique a wide application.

References for Chapter 6

1. D. K. C. Wu, B. T. Kuhlmey, B. J. Eggleton, "Ultrasensitive photonic crystal fiber refractive index sensor," Opt. Lett. **34**, 322-324 (2009).

2. B. T. Kuhlmey, B. J. Eggleton, D. K. C. Wu, "Fluid-filled solid-core photonic bandgap fibers," J. Lightwave Technol. **27**, 1617-1630 (2009).

3. K. Nielsen, D. Noordegraaf, T. Sørensen, et al, "Selective filling of photonic crystal fibres," J. Opt. A, Pure Appl. Opt. **7**, L13–L20 (2005).

4. L. Xiao, W. Jin, M. S. Demokan, et al, "Fabrication of selective injection microstructured optical fibers with a conventional fusion splicer," Opt. Express **13**, 9014–9022 (2005).

5. Y. Huang, Y. Xu, A. Yariv, "Fabrication of functional microstructured

optical fibers through a selectivefilling technique," Appl. Phys. Lett. **85**, 5182–5184 (2004).

6. J. Canning, M. Stevenson, T. K. Yip, et al, "White light sources based on multiple precision selective micro-filling of structured optical waveguides," Opt. Express **16**, 15700–15708 (2008),

7. C. Martelli, J. Canning, K. Lyytikainen, et al, "Water-core Fresnel fiber," Opt. Express **13**, 3890–3895 (2005).

8. C. M. B. Cordeiro, E. M. Dos Santos, C. H. Brito Cruz, et al, "Lateral access to the holes of photonic crystal fibers - selective filling and sensing applications," Opt. Express **14**, 8403–8412 (2006).

9. C. M. B. Cordeiro, C. J. S. de Matos, E. M. dos Santos, et al, "Towards practical liquid and gas sensing with photonic crystal fibres: side access to the fibre microstructure and sing-mode liquid core fibre," Meas. Sci. Technol. **18**, 3075–3081 (2007).

10. X. Zhang, R. Wang, F. M. Cox, et al, "Selective coating of holes in microstructured optical fiber and its application to in-fiber absorptive polarizers," Opt. Express **15**, 16270–16278 (2007).

11. Y. Wang, C. R. Liao, D. N. Wang, "Femtosecond laser-assisted selective infiltration of microstructured optical fibers," Opt. Express. **18**, 18056-18060 (2010).

12. P. St. J. Russell, "Photonic-crystal fibers," J. Lightwave Technol. **24**, 4729-4749 (2006).

13. J.-l. Kou, Z.-d. Huang, G. Zhu, et al, "Wave guiding properties and sensitivity of D-shaped optical fiber microwire devices," Appl. Phys. B, DOI: 10.1007/s00340-010-4244-y (2010).

14. F.A. Jenkins, H.E. White, *Fundamentals of Optics*, McGraw-Hill Inc: New York (1976).

15. Y. Wang, Y. Li, C. Liao, et al, "High-temperature sensing using miniaturized fiber in-line Mach–Zehnder interferometer," IEEE Photon. Technol. Lett. **22**, 39-41 (2010).

16. G. E. Town, W. Yuan, R. McCosker, et al, "Microstructured optical fiber refractive index sensor," Opt. Lett. **35**, 856-858 (2010).

17. W. Yuan, G. E. Town, O. Bang, "Refractive index sensing in an all-solid twin-core photonic bandgap fiber," IEEE Sens. J. **10**, 1192-1199 (2010).

18. B. J. Mangan, J. C. Knight, T. A. Birks, et al, "Experimental study of dual-core photonic crystal fibre," Electron. Lett. **36**, 1358-1359 (2000).

19. Z. Wang, T. Taru, T. A. Birks, et al, "Coupling in dual-core photonic bandgap fibers: theory and experiment," Opt. Express **15**, 4795-4803 (2007).

20. W. E. P. Paddena, M. A. van Eijkelenborg, A. Argyros, et al, "Coupling in a twin-core microstructured polymer optical fiber," Appl. Phys. Lett. **84**, 1689-1691 (2004).

21. J. Du, Y. Liu, Z. Wang, et al, "Thermally tunable dual-core photonic bandgap fiber based on the infusion of a temperature responsive liquid," Opt. Express **16**, 4263-4269 (2008).

22. T. Toyoda, M. Yabe, "The temperature dependence of the refractive indices of fused silica and crystal quartz," J. Phys. D, Appl. Phys. **16**, L97-L100 (1983).

Chapter 7 Conclusion and Further Work

7.1 Conclusion

In this thesis, with the help of fs laser micro-machining, several kinds of novel micro-structures are fabricated on optical fibers. Compared with normal OFS, these micro-structures embedded devices possesses the advantage of compact device dimensions and relative high sensitivities, which may help to achieve small dimensional sensing such as the idea of point sensing.

The fs laser micro-machining system is built up for fabricating micro-structures on the fiber. The laser pulse parameters, including the spatial beam diameter and the single pulse energy can be adjusted by the external optical path. A microscope system including a 3D translation stage and a CCD camera is used for real time observation of the fs laser micro-machining process. The MO can focus fs laser directly onto the fiber under fabrication. Normally, MO with larger magnification has a larger NA value and thus a smaller focused beam diameter at the beam waist, and therefore, the focus point will have larger spatial laser intensity. Besides, MO with larger magnification can enable more accurate positioning of the focus point on the fiber. However, the Rayleigh length is also smaller, which limits the depth of the fabricated micro-structure. Proper selection of MO depends on the micro-structure to be fabricated.

By local fs laser irradiation, a micro-hole can be effectively drilled into the fiber core center without chemical etching. This micro-structure can be applied for RI sensing by detecting the transmission loss at certain wavelength. The RI sensing property depends on the diameter of the micro-hole at the core, which can be changed by adjusting proper pulse energy and irradiation time. The transmission loss responses to the external RI are linear for both the half through micro-hole

and the full through micro-hole with diameter (near the fiber core) larger than that of the fiber core. The temperature-RI cross sensitivity of the half through micro-hole is less than 4.0×10^{-4}, obtained by immersing it into water and measuring its transmission loss while heating the water. This enables a temperature insensitive RI measurement achieved by the micro-hole structure.

A micro-cavity can be fabricated in SMF by line scanning the fs laser focus point along the fiber length. The micro-cavity is positioned asymmetrically on one side of the fiber core and acts as one arm, while the remaining fiber core acts as the other arm, to form a fiber-inline MZI. The extreme large RI difference between the two arms enables a much more compact device length for certain OPD requirement. Different micro-cavity lengths in the order of tens of μm are fabricated and the corresponding FSR are observed. The visibility of the fabricated MZI can be optimized to be larger than 15 dB by removing the core width properly and using a slow and repeated fs laser scanning process. The micro-cavity is a permanent structure as long as the cavity length does not change with temperature, which enables a high temperature sensor up to 1100 ℃ with a good precision and repeatability. Besides, the device has a considerably high RI sensitivity of ~9300 nm/RIU for RI change around water.

When periodical micro-holes are drilled along the fiber length, a novel kind of structural modulated LPFG can be fabricated by fs laser micro-machining. In this thesis, symmetrically or asymmetrically located micro-holes based LPFG are fabricated in all solid PBGF and SMF, respectively. Such a structural modulated LPFG belongs to the type of strongly waveguide variation LPFG; whose coupling mechanism can be explained by a CLM theory. The cladding modes involved in mode coupling are checked by both simulation and experiment observation to be LP_{11} and LP_{16} modes for the two kinds of fiber, respectively. The experimental phase matching curves of the corresponding cladding modes are also compared with simulation results. The RI responses of

the two types of LPFG have been checked in the RI range around water (1.33). Compared with normal RI modulated LPFG, the higher RI sensitivities around the RI of water enables structural LPFG as RI sensor for water solution. This kind of device demonstrates the possibility of integration of multiple micro-structures into one fiber and together develop functional OFD.

The micro-hole embedded FBG device is developed through asymmetrically positioning several micro-holes in the FBG region with the FBG sensor inscribed in advance. The micro-holes can make the fiber core partially exposed to the external environment without significantly damaging the periodical FBG structure. This device can be applied as simultaneous and independent temperature and RI sensor, by tracing only the FBG resonant dip with both of its wavelength and transmission. It also has a compact dimension and is convenient in operation. The micro-hole embedded FBG sensor shows the possibility of embedding micro-structures in optical fiber without destroying other sensing element inscribed according to the fine property of fs laser micro-machining.

Fs laser assisted selective infiltration of air hole(s) in the commercial LMA-10 PCF is developed. The main steps of this technique include: (1) fusion splice with SMF to block all air holes; (2) laser cleaving near the splicing point and (3) open certain air hole and infiltrate liquid analyte with RI higher than the background silica into the opened air hole. By infiltrating a type-A air hole of the LMA-10 PCF, a directional coupler is achieved by coupling the PCF core mode to the LP_{01} mode of the high RI rod. Another kind of MZI can be achieved by infiltrating two adjacent air holes of the innermost layer: a hybrid mode can be supported by the coupling of LP_{11} modes between the two high RI rods, which interferes with the PCF core mode. Both the two types of devices can be applied as temperature sensors with very high temperature sensitivity. The temperature sensitivities are simulated to be close to the experiment results.

Compared with the micro-structure based OFS reported in previous literatures, this thesis has proceeded with the work of fs laser micro-machining on optical fiber in the following aspects: (1) Several novel kinds of micro-structures are developed in optical fiber, some of which can be applied as other functional OFD besides their sensing application, such as the micro-cavity MZI and the micro-holes based LPFG; (2) This thesis also demonstrates the possibility of integration of multiple micro-structures into one fiber, such as the periodical micro-holes based LPFG and the micro-holes embedded FBG sensor. The latter case also makes progress for integrating micro-structures into fiber with other sensing element inscribed in advance; (3) The fs laser assisted selective infiltration technique broadens the applications of fs laser micro-machining in fabricating novel fiber devices without micro-structures left in the final device.

7.2　Further Work

The micro-structures developed in this thesis are directly fabricated into fiber, with relatively large pulse energy and thus part of the fiber is removed. This may result in a coarse morphology of the ablation surface due to the thermal effect, which induces unwanted scattering loss and geometry error. One promising solution is to take advantage of the internal fabrication ability of fs laser. With the fs pulse energy smaller than the threshold energy for material damage, RI modulation region (or imprint) can be induced inside the optical fiber. This imprint can be removed by diluted HF with a much larger etching rate than the other part of fiber without imprinting so that the desired micro-structure can be obtained, with its surface much more smooth than that of direct ablation. However, the imprinting pulse energy, the concentration of HF, and the etching time need to be optimized, which may be a time consuming work. One of the applications of the chemical etching assisted fs micro-machining is to fabricate micro-structure inside the optical fiber, such as micro-ring and micro-waveguide.

Another important issue to be addressed before the micro-structure OFS can be practically used is the proper protection of the devices. Since part of the fiber is removed, the mechanical strength will be significantly lowered, although the devices in experiments are not easily broken. A straight ceramic or stainless steel tube with proper adhesive glue may help to achieve this purpose.

The ultra-high pulse intensity of fs laser and its ablation mechanism may help to achieve micro-machining on special Sapphire fiber, which has a relative high melting point over 2000 ℃ (and therefore can hardly be processed by normal lasers such as CO_2 or UV laser). The single crystal property makes the Sapphire fiber only has a core rod structure without cladding, being different with normal SMF, which may lower the transmission loss when micro-structures are fabricated into it.

The fs laser assisted selective infiltration technique opens a way for highly flexible infiltration of any air hole(s) of PCF. The devices developed in this thesis are just prototypes for application. Further works, including optimization of the device length for efficient coupling, selection of suitable RI as the infiltrated analyte, and solidification of the liquid analyte need to be carried out. Moreover, other functional devices can be developed by this technique. For example, if a series of in-line air holes are infiltrated with RI smaller than background silica, the resultant fiber may turn into a Hi-Bi PCF, with its birefringence tuneable. Besides, this technique can produce internal metal rods in PCF if melting gold can be successfully infiltrated, which has potential applications for integrated metal switch or surface plasma resonant sensors.